The Graduate University for Advanced Studies, SOKENDAI

School of Physical Sciences
National Institute for Fusion Science

Applicability of High-Temperature Superconducting Stacked-Tape Large-Current Conductors to Fusion Magnets

PhD Thesis

Garfias Dávalos Diego Armando

Supervisors:
Nagato Yanagi
Yoshiro Narushima

Toki, Japan. March 2024

Contents

List of Figures

List of Tables

Glossary

A

AC Alternating Current. vi, 18, 19, 23, 24, 29, 30, 33–36, 40, 41, 70, 107
ARC Affordable, Robust, Compact. 8
ASTRA Aligned Stacks Transposed in Roebel Arrangement. 24

B

BRAST BRAided STack. 24
BSCCO Bismuth Strontium Calcium Copper Oxide. 12, 17, 57, 64, 65

C

CFS Commonwealth Fusion Systems. 22
CICC Cable-in-Conduit Conductor. 24, 25, 28, 33, 36, 38, 97, 102
CoE Cost of Electricity. 8
CroCo CrossConductor. 25
CS Central Solenoid. 38
CSMC Central Solenoid Model Coil. 37

D

DC Direct Current or Continuous Current. 7–10, 19, 25, 33, 40, 41, 95, 100, 106–108
DP Double Pancake. 95, 96, 98

E

ENEA Agenzia nazionale per le nuove tecnologie, l'energia e lo sviluppo economico sostenibile (Italian National Agency for New Technologies, Energy and Sustainable Economic Development). 24
EPFL École Polytechnique Fédérale de Lausanne. 24
EXSIV Experiments on a Single Inner Vertical coil. 34

F

FAIR Friction stir welding, Aluminum alloy jacket, Indirect cooling, and REBCO tapes. 21, 40
FEM Finite Element Method. 104

G

GFRP Glass Fiber Reinforced Plastic. 49

H

HTS High Temperature Superconductor. iii, iv, 5–26, 28–33, 40–43, 49, 50, 52–54, 57–59, 61, 62, 64, 66, 67, 70–75, 77, 78, 80, 81, 83, 85, 87, 90, 92–95, 97, 98, 100–104, 106–110, 113

I

IAEA International Atomic Energy Agency. 1
ITER From latin: "the way". 39, 95–98, 107

J

JT-60SA Japan Torus 60 Super Advanced. 38

K

KCL Kirchhoff's Current Law. 113
KIT Karlsruhe Institute of Technology. 24, 25
KVL Kirchhoff's Voltage Law. 113

L

LHD Large Helical Device. 2, 34
L-RAISER Inductance (L) RAISing ExpeRiment. 43, 72, 83, 103, 109
LTS Low Temperature Superconductor. 5–10, 12–15, 17, 18, 28–30, 32, 33, 40, 41, 70, 92, 95, 97, 100, 107–109

M

Maglev Magnetic levitation. 14
MCF Magnetic Confinement Fusion. 2–4
MIT Massachusetts Institute of Technology. 21, 22
MRI Magnetic Resonance Imaging. 12, 14
MTS Medium Temperature Superconductor. 12–14

N

NIFS National Institute for Fusion Science. 2, 19, 20, 108
NINT No-Insulation No-Twist. 20
NMR Nuclear Magnetic Resonance. 14
NSTX National Spherical Torus Experiment. 8
NUCD Non-Uniform Current Distribution. vii, x, 10, 32–34, 36, 37, 41, 42, 47, 49, 57, 61, 76, 80, 85, 108, 109

P

PFCI Poloidal Field Conductor Insert. 37

R

REBCO Rare Earth Barium Copper Oxide. vii, 7, 9, 12, 16–18, 20, 41, 42, 53, 57, 64, 70–72, 81, 103, 109
RRL Ramp Rate Limitation. 29, 108, 109

S

SC Superconducting, superconductor. 28, 29, 33
ScGA Superconductivity Global Alliance. 13
SDG Sustainable Development Goals. 1, 13

SECAS SECtor ASsembled. 24
SPARC Soonest/Smallest Private-Funded Affordable Robust Compact. 20
SST-1 Steady State Tokamak - 1. 36
STARS Stacked Tapes Assembled in Rigid Structure. 40, 53, 64, 68, 72, 77, 80, 83, 87, 92, 94, 97, 102–104, 106, 109

T

TFC Toroidal Field Coil. 8, 20, 39, 77, 95–98, 107
TFMC Toroidal Field Model Coil. 20
TJ-II Tokamak de la Junta II. 8
TSTC Twisted Stacked-tape Conductor. 21, 25

U

UNDP United Nations Development Program. 1, 13
UNFC United Nations Framework Classification for Resources. 1
UNRMS United Nations Resource Management Systems. 1

W

WISE Wound and Impregnated Stacked Elastic tapes. 40

Y

YBCO Yttrium Barium Copper Oxide. 70

Abstract

Non-Uniform Current Distribution (NUCD) reduces the stability of Low-Temperature Superconducting (LTS) cables, causing premature quenches and reduction in the operation current, especially with fast ramp rate (Ramp Rate Limitation; RRL), and the reason for which twisting and transposition of superconducting strands is necessary for stable operation. A non-twisted simple-stacking approach for high-current High-Temperature Superconducting cables based on tapes has been investigated, taking advantage of the higher cryogenic stability of HTS compared to LTS, where twisting and transposition may not be necessary for stable operation, especially for DC current.

Simple-stacking is mechanically robust and low-cost to manufacture, yet since a non-uniform current distribution gets formed among HTS tapes following parallel paths, further clarification is required to confirm stable operation under a coil shape with inductance variation between strands. In this project three experiments confirmed stable operation of the simple-stacking configuration under NUCD: for a short-straight cable (1.3 m long, 5 stacked REBCO tapes), the 20-kA-class "STARS" cable coiled sample (6 m, 15 stacked REBCO tapes), and the "L-RAISER" HTS solenoid experiment (10 m, 5 stacked REBCO tapes).

Circulation currents normally occur in superconducting cables, as they have been observed in large LTS magnets (especially wound with cable-in-conduit conductors). They are related with NUCD, in the sense of the different current share among superconducting strands, which can lead to unstable operation. Similarly, circulation currents were confirmed in the 20-kA-class STARS cable, by means of a measured residual magnetic field, dependent on the ramp rate applied to the coiled sample. The L-RAISER solenoid investigated further by intentionally enhancing circulation currents, confirming stable operation in a higher self-inductance of the strands, under a fast ramp-rate and the presence of NUCD.

Two constant-temperature numerical calculations for the current distribution in stacked HTS cables have been developed, for straight (R circuit) and coiled (RL circuit) cable configurations. The R circuit calculation takes into account the resistance of the superconducting layers according to the Power Law for HTS, while including the experimental contact resistance between REBCO tapes. It reproduces the experimental data obtained in the voltage taps of the 1.3 m HTS cable experiment. The RL circuit calculation considers both resistance of the superconducting strands, and the inductance resulting from such strands following parallel paths in a coiled configuration. The residual magnetic field decay observed in the 20-kA-class STARS conductor was reproduced, and better insight of how the current distribution may look in stacked HTS cables. By extending these results, an extrapolation for a double pancake inside the ITER TFC magnet was done. Results suggest that stable operation may be available for such large HTS magnets based on simple-stacking, where inductance variation is present, up to a few kA/s ramp-up rate.

While a zero-dimensional thermal calculation indicates negligible temperature rise for the 20-kA-class STARS experiment by ohmic losses with a NUCD, an extended thermal calculation remains as future work, in order to clarify the reduction of critical current while accounting heat propagation.

1 Introduction

1.1 Superconductivity and Nuclear Fusion

Nuclear fusion can provide a new energy source to complement the electricity generating options available, including fossil fuels, hydroelectric, wind, solar, geothermal, biomass and nuclear fission. What kind of energy source is used varies within regions and countries, due to differences in available land for deployment, natural resources, energy requirements for dense urban regions and political stances. An objective comparison of what energy source to use considers land area used per unit of energy produced, and fuel volume or weight consumed per unit of energy output [1]; so an energy mix based on the local conditions and resources works best for the electricity production needs of a region [2].

For the sustainable development of the energy sector, nuclear fusion and fission are considered viable players that can contribute to the effort. In terms of the United Nations Development Program (UNDP) and the Sustainable Development Goals (SDG) [3], they are considered an important support pillar towards the 2030's. It may be worth to note that public perception may influence the preference of some energy sources over others and influence political agendas, that may be inadvertedly hurtful by not reducing greeenhouse emissions in the energy sector. To attain sustainability goals it is convenient to account scientific and economic factors, as well as the industrial capability to attain the goals of the energy sector decarbonisation as fast as possible, adjusted to the geography, resources and financial capabilities of each country [4, 5].

Nuclear energy is considered able to make make contributions to all the 17 SDG's by multiple international scientific entities. These include the International Atomic Energy Agency (IAEA) with its program "Atoms for Peace and Development", the World Nuclear Association; while being backed up within the United Nations Framework Classification for Resources (UNFC) and the United Nations Resource Management Systems (UNRMS) to guide policies and development of nuclear projects to contribute the energy mix of countries towards reducing greenhouse gas emissions [6]

Directly in terms of SDG's the 7th goal (Affordable and Clean Energy) and 13th goal (Climate Action) are addressed. As nuclear energy (both fission and fusion) has high energy density, significant electricity can be produced in a low area footprint, with a baseload capability to cover the demands of large cities or industrial sites, as it is available 24 h without being dependent on weather. Being also a low CO_2 energy source, it can complement other renewable energy sources to gradually replace in a joint effort fossil fuel energy sources, to decarbonise the energy sector [7–9].

Currently no single low CO_2 energy source (wind, solar, geothermal, hydro, or nuclear) has the industrial deployment capability to single-handedly replace fossil fuel energy source fast enough to attain the United Nations 2030 decarbonisation goals (furthermore solar and wind also require large amounts of energy storage to account fluctuation with no energy production at night or low speed wind periods). So a joint effort of all the available low CO_2 energy source options may be the safest bet towards attaining the 1.5 degrees limit from the Paris Agreement in 2015 [10].

Nuclear fission for electricity generation has been available since the late 1950's. It can provide a continuous energy supply with reduced CO_2 emissions, as the reaction can be tuned to supply a needed energy output. High initial construction costs and nuclear waste production and handling are concerns that difficult a widespread acceptance and use of the technology [11]. Nonetheless, reprocessing technology of nuclear waste keeps developing, to recover fissile resources and reduce the lifetime of nuclear waste [12, 13].

Nuclear reactions are energy dense compared to chemical reactions (e.g. burning fossil fuels for generating thermal energy that can be converted to electricity). Nuclear fission is based on splitting heavy atoms, such as uranium or thorium [14], which releases energy and uses solid or liquid fuel. In the case of nuclear fusion the approach is the opposite, fusing light atoms such as hydrogen isotopes also releases energy, but the fuel needs to be at a high temperature, up to the plasma state of matter.

A star such as the sun, can sustain a plasma by gravitational confinement, producing fusion of the atoms in it, and continuously produce heat energy. To confine a plasma and extract energy from it on Earth, gravitational force is not available, so strong magnetic fields are used, produced by coils in nuclear fusion reactors, in the MCF (Magnetic Confinement Fusion) approach.

For MCF, toroidal-shaped fusion reactors there are two main designs: the tokamak and the stellarator. They achieve the best results for confinement time, plasma density and temperature; key parameters that lead to a fusion plasma that can be used as an energy source [15].

The tokamak is the most widespread MCF design, consisting of a set of planar coils in different orientations, able to create the helical and toroidal magnetic field required for plasma confinement, via a plasma current and the magnetic field created by the coils. For the stellarator family of devices, they create the helical toroidal magnetic field by coils with more complicated geometries, without need of a plasma current. The heliotron concept is a stellarator-like device, that uses two sets of helical coils to create the required magnetic field, being LHD at NIFS the biggest of its kind.

While perhaps simpler to operate and with potentially less plasma instabilities by having no plasma current, the complex manufacturing of stellarator/heliotron devices gave a time edge to tokamaks to be developed first. Figure 1 shows a general comparison between a tokamak and heliotron fusion devices.

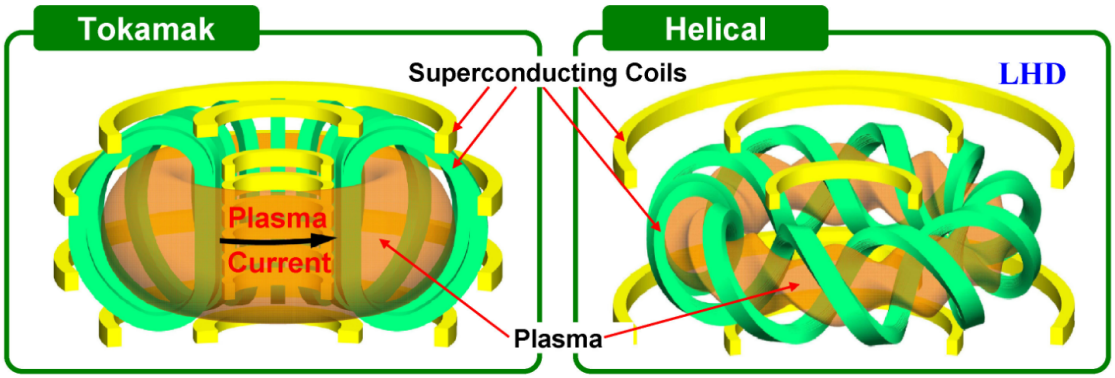

Figure 1: Schematic for toroidal MCF devices. Left: The tokamak is the most widespread design, consisting of planar set of coils to confine the plasma. Right: The heliotron features continuous helical coils that go around the torus shape, achieving the same plasma confinement effect.

Increasing the magnitude of the magnetic field results in a better confinement of the plasma, holding in closer proximity the atoms that can interact and ultimately fuse to generate energy. As such, a high magnetic field is desirable to be increased, which may be more clearly explained by looking into the related equations.

In toroidal MCF devices, the toroidal beta is a parameter to describe the plasma (β_T), defined as the ratio of the kinetic plasma pressure to the magnetic pressure:

$$\beta_T = \frac{\bar{p}}{B_0^2/2\mu_0}$$

with $\bar{p}$ the volume averaged plasma pressure and B_0 the toroidal magnetic field on the plasma axis, defined by the torus' major radius R_0. The fusion power density per volume unit ($\frac{P_f}{V_p}$) scales with the square of the kinetic pressure, then replacing the previous equation for the definition of toroidal beta results in:

$$\frac{P_f}{V_p} \propto \bar{p}^2$$

$$P_f \propto \beta_T^2 B_0^4 V_p$$

Then we can clearly see the advantage of increasing the magnetic field strength in a fusion device, because of this fourth power dependence (considering a constant β_T). While increasing the volume of the machine helps to get more fusion power output, comparatively, increasing the magnetic field has a stronger effect for the energy produced in a fusion reactor, which can then be converted to usable electricity. In other words, it also means that the size of fusion reactor can be reduced for the same power output, reducing the total cost of the device [16, 17], or the power production increased for a given reactor size with a stronger magnetic field.

While increasing the reactor size may be a straightforward solution, total cost rises and manufacturability becomes more difficult, with larger and heavier pieces that conform the

reactor, with tolerances and possible assembly accidents becoming a more serious issue. Still, it is necessary to keep a minimum size in the reactor, to shield neutrons produced in the fusion reactors, while extracting their thermal energy into a wide volume.

In short, a fusion reactor as of mid-term may provide a low CO_2 emissions controlled source of thermal energy, that can then converted into electricity via a steam cycle [18]. The steam cycle process is the same approach that is done in nuclear fission reactors or fossil fuel power plants, shown in Figure 2. The availability of nuclear fusion as another energy option may be incorporated with future long-term sustainable energy planning scenarios [19–21], and linked to other efforts to reduce CO_2 emissions, such as the transition towards a green hydrogen society [22–28].

While there are alternative fusion reactor concepts that may skip the steam cycle into directly generating electricity, the focus of this text is for MCF reactors that produce thermal energy that is then converted to electricity, and specifically about the superconducting cables used in the magnet system.

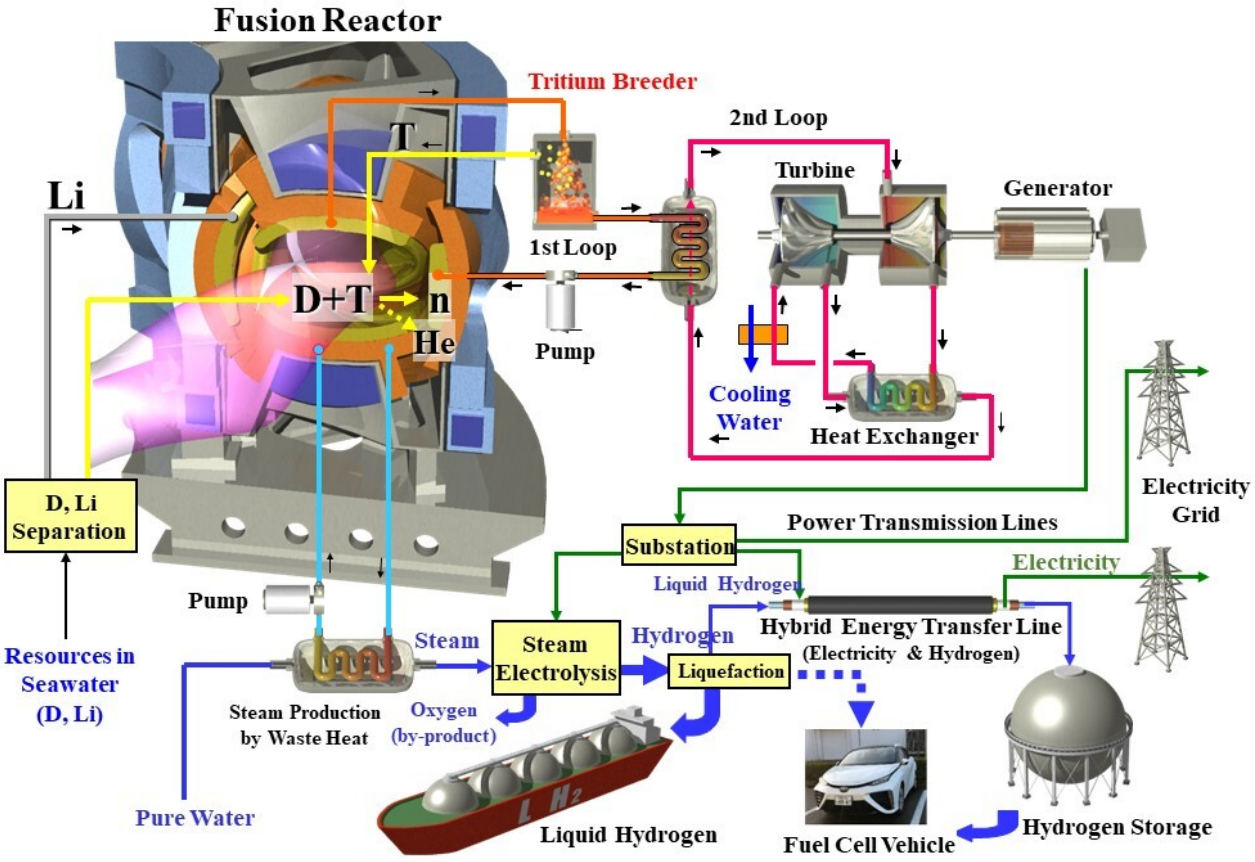

Figure 2: Concept of a Nuclear Fusion Power Plant connected to the electric grid, and in line with sustainable development towards low CO_2 emissions. While the electricity is produced via a steam cycle extracting the heat energy from the fusion reactions, waste heat can be recirculated towards other purposes, such as green hydrogen generation and housing heating.

The magnet system of most fusion reactors up to now is made with Low-Temperature Super-

conductors (LTS), which have been commercially available in kilometer-length quantities for more time than High-Temperature Superconductors (HTS), making LTS relatively cheaper than HTS. However, HTS can achieve higher current density, which leads to stronger magnetic field and better performance for the plasma confinement, and as such it would be the preferred magnet technology for a fusion reactor.

There is a push in the fusion community to transition towards HTS magnet systems, as overall the better plasma confinement performance with a higher magnetic field, can increase the fusion energy produced in the reactor. The fusion energy gain factor Q is a parameter ratio that accounts the various power sources and sinks occurring in a fusion reactor [17], which can be seen as:

$$Q = \frac{\text{net thermal power out}}{\text{heating power in}} = \frac{\text{total thermal power out} - \text{heating power in}}{\text{heating power in}} = \frac{P_{out} - P_{in}}{P_{in}} \tag{1}$$

The gain factor has to be larger than one ($Q > 1$), which implies that more energy is produced in the fusion reaction, than the energy required to initiate the fusion reactor in the first place. In reality the gain factor is further reduced by the energy conversion from thermal energy to electricity.

The engineering gain factor Q_E shows the real energy gain value in terms of total electric power used to produced the fusion reactions ($P_{in}^{(E)}$), and electric power obtained from the fusion reactions after conversion by the thermal steam cycle ($P_{out}^{(E)}$), both gain factors shown in Figure 3. Q_E may be roughly estimated as 30% of Q, for the average energy conversion efficiency of a steam cycle:

$$Q_E = \frac{P_{out}^{(E)} - P_{in}^{(E)}}{P_{in}^{(E)}} \tag{2}$$

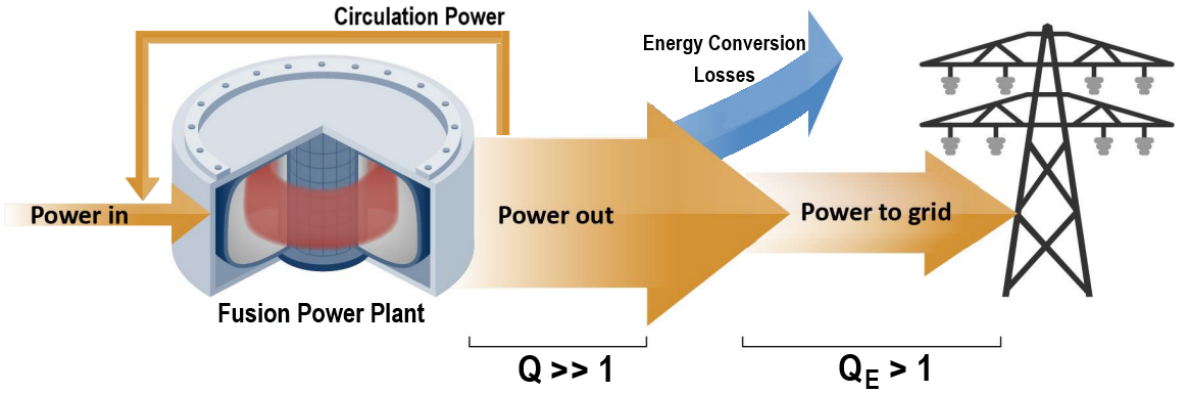

Figure 3: Power balance schematic for a nuclear fusion power plant, in terms of the gain factors Q and Q_E . Q is significantly larger than 1, which means that more energy is obtained from the nuclear fusion reactions than the energy needed to start them., After the energy conversion losses, Q_E should be at least larger than 10, for a commercially viable energy source. Adapted from [29].

As such, for a fusion reactor for electricity generating purposes, a gain factor of ($Q = 10$) is deemed as a minimum value to aim for a power plant, with at least ($Q \geq 20$) considered a more economically viable electricity generating source. Figure 4 shows for different fusion reactor designs, a comparison for size, magnetic field in the plasma region and gain factor; including the magnetic field strength regions attainable with LTS and HTS.

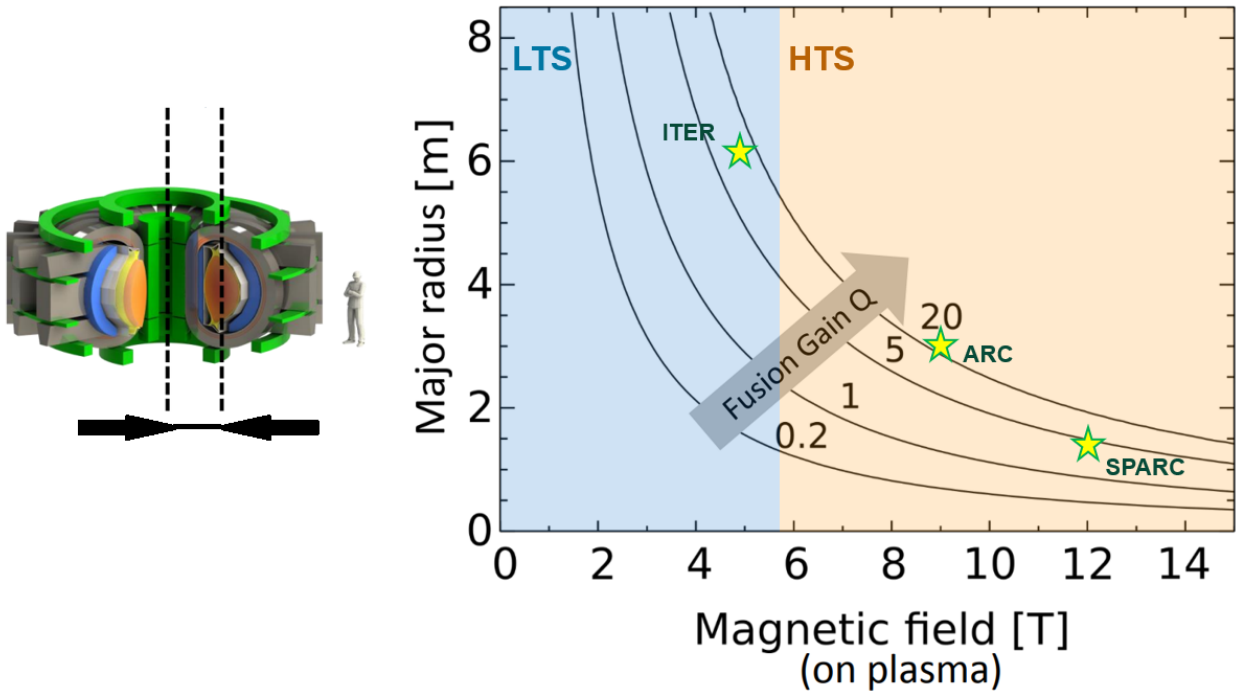

Figure 4: Fusion energy gain factor lines for tokamak devices, depending on the major radius and magnetic field on the plasma axis. As LTS magnets are limited to a maximum magnetic field of around 6 T at plasma center, incorporating HTS makes available smaller fusion devices with higher gain factor Q. This gain factor scaling applies to stellarator devices as well. Adapted from [30] .

1.2 Fusion Reactor Concepts with HTS

An advantage by using HTS is the higher temperature that they can be operated, which allows a larger heat capacity of the materials, so they can be more resilient to heat disturbances with a lesser temperature rise.

The higher critical temperature also allows using other coolants, besides helium which is compulsory for the operation of LTS. As coolants such as liquid hydrogen or liquid nitrogen become available, the cryogenic cooling system can be significantly cheaper. This may allow the development of smaller fusion reactor concepts to be explored with HTS magnets and more limited budgets [31–33], as e.g. liquid nitrogen can enable a significantly higher current density in an HTS cable compared to a copper cable.

In the case of nuclear fusion magnets for power plant scale, as previously mentioned, the fusion power output scales with the magnetic field strength and size of the machine. Considering that the magnetic field strength is fixed for a given material performance, increasing the

size can give a further performance boost, yet precision manufacturing of large scale pieces weighing tonnes becomes the limitation factor.

A solution, to manufacturing large scale magnets, is to section them in pieces, assemble them together, and electrically connect their joints via solder or mechanical pressure. In LTS this process is usually not available, as the materials have a lower heat capacity by operating at temperatures around 4 K, and joints may produce too much joule heating and the superconducting state lost. On the other hand, HTS can operate at higher temperatures, e.g. at 20 K, where materials have higher heat capacity and cryogenic stability, so they may be able to withstand slightly more joule heat generation by joints, while extracting this heat and remain at the operating temperature in the superconducting state [34].

Figure 5 shows schematics for large superconducting DC magnets where demountability could be used: toroidal field coils for the case of a tokamak, and helical coil in the case of a heliotron fusion reactor configuration.

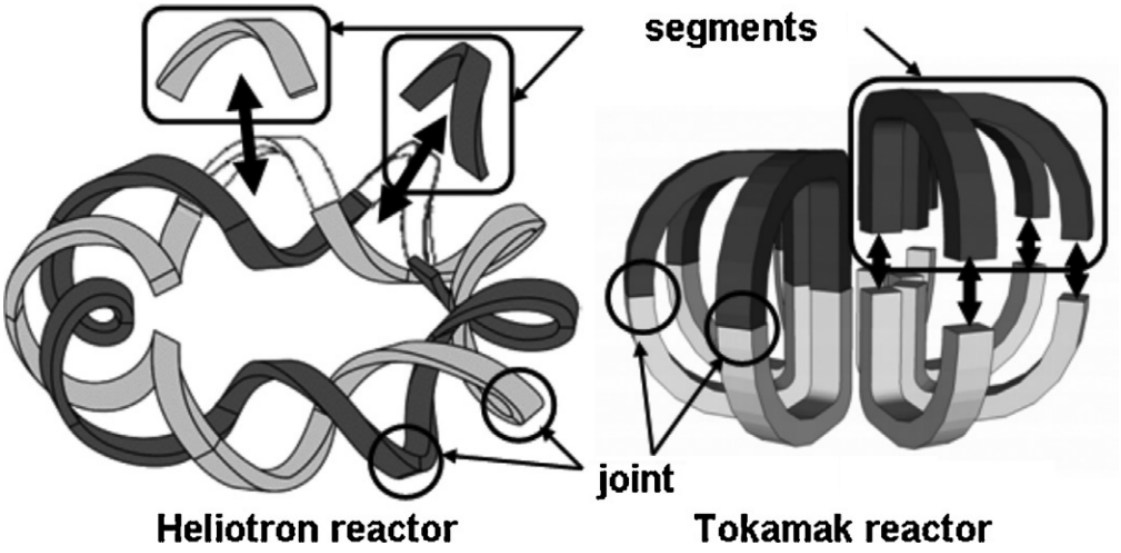

Figure 5: Remountable magnet concepts for tokamak and heliotron devices, to fabricate large-scale power-plant size coils. The higher cryogenic stability of HTS may allow to fabricate such magnets sections and assemble them via joints. Apart from assembly itself, being the magnets remountable allows for faster maintenance campaigns and fix scenarios in case of damage [35] .

The resistance of a joint for a large reactor size magnet is at the $n\Omega$ level, despite this being a low value, the total joule heating can add up depending on the number of joints, whose generated joule heating has to be extracted by a cooling system. Nevertheless, some estimations indicate that for a large tokamak with HTS toroidal field coils made with REBCO tapes and soldered joints would add a few percent of heat load to the cryogenic cooling system, considered to be feasible to implement and still operate stably [35].

Thanks to the increase in availability and consistent high-quality of HTS conductors, as

well as the decrease in cost, makes a case to explore the possibilities of even estimating operation prices of a power plant. An EURATOM/CCFE study made a comparison of the Cost of Electricity (CoE), estimating a slight decrease in price when using HTS instead of LTS for a demountable TFC system, while reducing the machine size and increasing the operating temperature [34].

By making magnets with demountable joints, faster modular construction as well as periodic maintenance may become available [36]. It allows to more easily disassemble the reactor, enabling access to internal regions for maintenance and replacement of damaged pieces, if or when there is the need to do so. Or if there is some damage in one section of a magnet for any reason, only the corresponding section can be replaced, instead of the whole magnet. Then if shut-down time for maintenance periods can be reduced, the total availability of a fusion reactor operation time can be increased. Such concept while optimal is a big challenge, which would need developing consistent techniques for low-resistance joints in multiple assembling/disassembling campaigns.

The idea of demountable magnets has been applied formerly for copper coils and earlier fusion devices, often in the Toroidal Field Coil (TFC) system. Examples of demountable coils include NSTX tokamak and TJ-II heliac device; as well as Alcator C-Mod tokamak [37]. With the availability of HTS the concept has been revised again to explore its applicability in large DC magnets based on HTS; such as the TFC for *ARIES-I* and ARC conceptual reactors [38, 39], and FFHR-d1 helical reactor [40].

The high-field ARC tokamak has been planned with modularity in mind, featuring a vertical assembly approach, where pieces may be replaced as units in case maintenance or replacing is required. By using HTS in the TFC system, it was estimated that the total power needed to cool the joints in the TFC was small and affordable compared to the total power balance of the reactor [39]. Figure 6 shows a schematic of the vertical assembly approach.

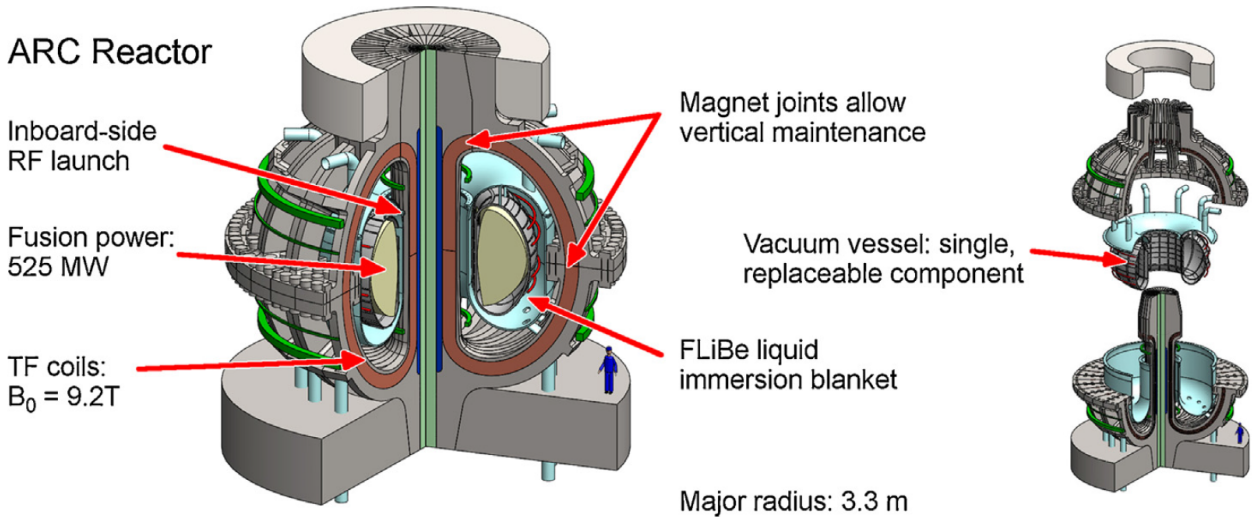

Figure 6: ARC reactor, featuring modular HTS coils, a liquid blanket, and vertical assembly for facilitating access and maintenance, with a major radius of 3.3 [m]. From [39].

The FFHR-d1 studies explore the feasibility of building a large scale magnet system, com-

posed of two helical coils made of HTS with a major radius of 15.6 m. Due to the large size of the coil, a "joint-winding" approach was explored, by considering one helical-pitch segments as a basic unit, joined by a total of 3900 bridge-type mechanical joints. Experiments and estimations for the total joule heating by all joints, suggest that said heat is low enough to be permissible, being a a small fraction of the available cooling power [41–44].

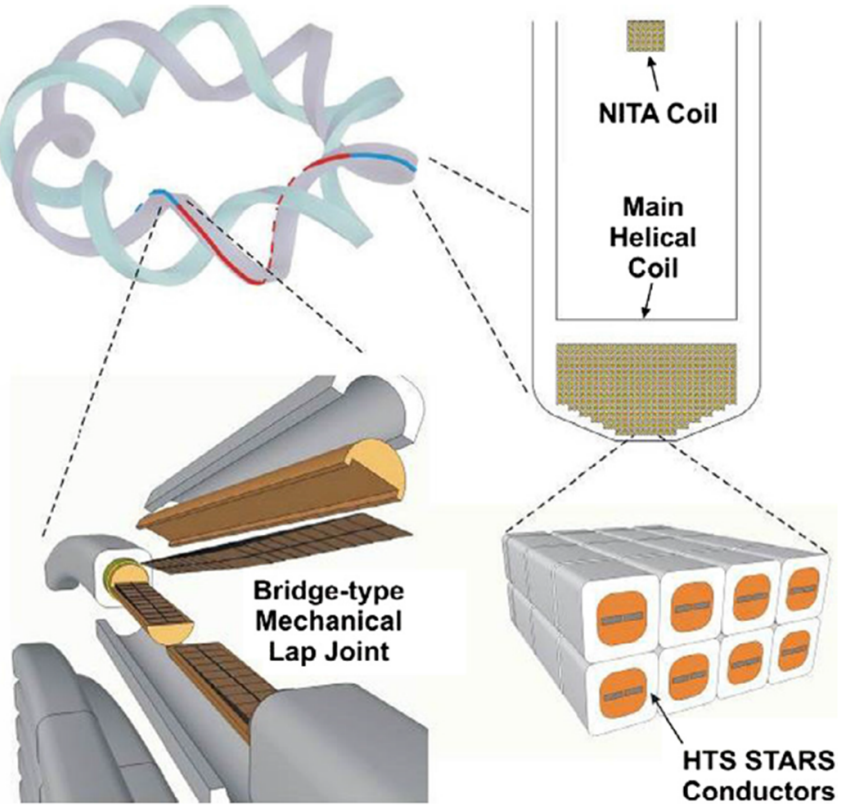

Figure 7: FFHR-d1 heliotron reactor concept, with HTS STARS conductors as the main element of the magnet system. Due to the large size of the helical magnets (major radius of 15.6 m), a once-through joint concept is foreseen joining one helical pitch segments, connected via joints such as the bridge-type mechanical one [45].

1.3 Research Question: Simple-stacking for large DC magnets

As described so far, there are a number of advantages of developing magnet systems in fusion reactors by using HTS. There are multitude of options to develop a high-current HTS cable, due to the geometries that different research groups around the world have proposed, with the availability of HTS conductors in the last 15 years or so.

The focus of this project is to explore if one of these cable concepts, called simple-stacking, can operate stably to be reliably used as the cable that conforms a HTS fusion magnet, operating in DC current. While LTS conductors come in the form of circular filaments, HTS conductors (especially the REBCO) have a planar tape form, as shown in Figure 8.

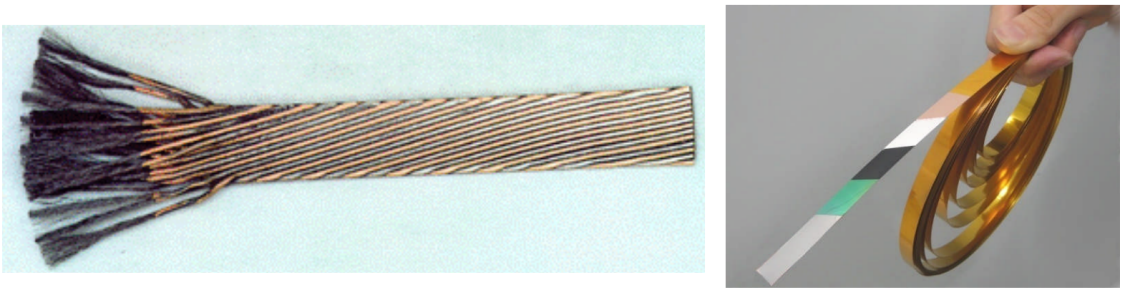

Figure 8: Comparison of LTS filaments (left) and HTS tapes (right). The circular cross section and relative ductility of LTS allows easy bending and transposition for a high-current cable with uniform current distribution. While transposition can also be applied to HTS tapes, the planar form partially limits the bending options and may cause degradation of the current handling capacity [30, 46].

By twisting and transposing filaments a uniform current distribution can be obtained in a cable. While for LTS the process is easily done due to the filament geometry, for HTS the process is slightly more complicated due to the limited bending of a planar tape. Simple-stacking avoids any twisting or transposition, with easier manufacturing and better mechanical properties against electromagnetic forces, at the cost of having a slight impedance variation among the HTS tapes.

A Non-Uniform Current Distribution NUCD is formed when impedance variation is present in the filaments of any cable, and is a source of diminished performance that has been historically observed in LTS cables. Simple-stacking is a concept mainly aimed to be applied for DC magnets made of HTS, aided by the better cryogenic stability of these materials compared to LTS. Further details are presented for the simple-stacking current distribution among HTS tapes in a high-current HTS cable.

So, this leads to the following research question, for application of simple-stacking in large HTS DC magnets:

Can a simple-stacking large-current HTS cable, operate stably in a coil shape for DC current, when inductance variation among the tapes is present?

In the next section, superconductivity concepts are introduced, and a number of high-current HTS cables are shown, to have a better grasp of the different approaches that are on research around the world, to contrast with the simple-stacking design. Later, a historical review is presented for LTS cable and unstable operation under NUCD, contrasted with stable operation in HTS while the NUCD was still present.

Later, experimental results from 3 HTS cables are shown, that confirm stable operation is possible so far in the conditions tested, while numerical simulations give additional insights into how the current may distribute along the cable in this geometry. Finally, a discussion for future work is presented, and key aspects to keep clarifying the applicability of simple-stacking for large HTS DC fusion magnets.

2 Superconductivity and HTS Technology

We start by introducing concepts that allow reaching a superconducting state in materials, in order to develop high-current cables to develop magnets for fusion applications, with a focus on High-Temperature Superconductors (HTS).

2.1 Superconductivity Concepts

2.1.1 Type I and Type II Superconductors

Shortly after the achievement of liquefying helium in 1908 by Heike Kamerlingh Onnes' research team, exploring material properties at temperatures close to 4 K became available. Three years later, the phenomenon of superconductivity in mercury was discovered, and later found in a number of materials at near zero Kelvin temperatures [47]. As such, expectation within the scientific community started for developing high-current cables for high-field magnets, surpassing the limitations of copper magnets and joule heating.

Eventually, by listing the superconducting material experimental observations, they were classified in Type I and Type II superconductors. When the materials are cooled below their critical temperature, magnetic field lines may partially penetrate into the material, or they are shielded and its propagation is impeded through it.

In superconducting materials this phenomenon is known as the Meissner effect. At low external magnetic field, the magnetic field lines are completely blocked from the material's interior, until reaching a critical magnetic field B_c, point after the superconducting state disappears [48] (sharply for Type I superconductors and gradually for Type II superconductors). The transitions regions of Type I and Type II superconductors are described in Figure 9:

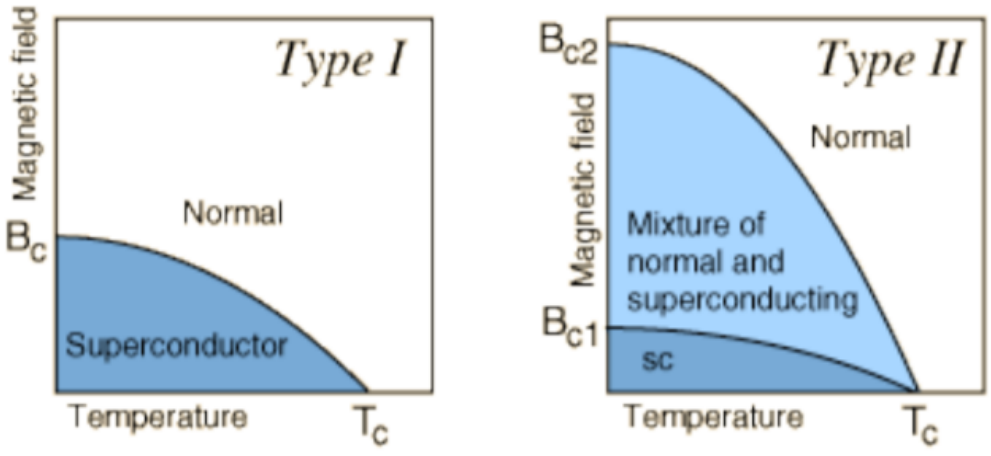

Figure 9: Schematic of magnetic field vs temperature dependence for Type I and Type II superconductors. The critical magnetic field B_c and critical temperature T_c define transition zones between superconducting and normal conducting states. There is a sharp transition for Type I superconductors, and a gradual transition (mixed state) region for Type II superconductors[49].

For Type I superconductors, the superconducting state disappears suddenly after the critical magnetic field is surpassed, point at which the magnetic field lines completely penetrate through the material. The maximum magnetic field tends to be relatively low, on the order of 0.1 T, and at the surface for a few micrometers depth, a current can flow as the critical temperature is not surpassed neither. As such, the low critical magnetic field, and small area where a current can flow, make Type I superconductors not practical for making wires and cables. Most of superconductors consisting of a single element are Type I.

For Type II superconductors, the behavior is different, as there is a transition zone from superconducting to normal conducting state, when the material is exposed between lower critical magnetic field B_{c1} and a higher critical magnetic field B_{c2}. Below B_{c1} the material is fully superconducting. Between B_{c1} and B_{c2} the magnetic field can partially penetrate the material at localized points as discrete flux lines, having then both superconducting and normal conducting regions. After surpassing B_{c2}, the superconducting states disappears completely and the material behaves as a normal conductor. Some elements such as Nb, V and Mo are Type II superconductors; yet materials practical for fabrication of high-current wires and cables are alloys and compound materials such as NbTi and Nb_3Sn. [50, 51].

2.1.2 LTS, MTS and HTS

Superconductors have been historically classified in function of its critical temperature T_c, threshold at which the superconducting state disappears, as described before. The focus of the superconducting materials mentioned here, is for those ones practical for the fabrication of high-current wires and cables.

Low-Temperature Superconductors (LTS) are now the materials which have more industrial maturity (such as NbTi and Nb_3Sn), and widely used for the manufacturing of high-field applications such as MRI, particle accelerator magnets or fusion magnets. The mechanical properties of the wires and circular cross section, allow winding and bending in different directions.

High-Temperature Superconductors (HTS) were discovered in 1986 [52, 53], which have the advantage of significantly higher critical temperature and critical magnetic field compared to LTS. Practical materials currently available for high-current applications include REBCO and BSCCO. They gradually have been decreasing in price, and become practical for applications were LTS haven't been widely used, including transformers, generators, motors for electric aircraft and outer space applications [54–62]. They usually come in the form of planar tapes due to their manufacturing process, which restricts bending in some directions as it may reduce their performance, yet manufacturing of high-current cables is available.

Mid Temperature Superconductors (MTS) are a class in-between the critical temperature of LTS and HTS, being MgB_2 one of the materials with higher prominence in this category. While their development and industrial availability is relatively recent compared to LTS or HTS, they have an interest to fill gaps in technology, on the meantime that prices in HTS keep decreasing to catch up and become widely adopted. They have better mechanical properties than HTS, and can serve as a stepping stone to reach better performance compared to LTS in applications such as MRI applications, while the price of HTS decreases to be more

widely adopted [63, 64].

We can see in Table 1 a compilation of superconducting materials for high-current cable applications, including their critical temperature and critical magnetic field [52, 64–69].

Table 1: Commercially available superconducting materials, along their critical parameters of temperature and magnetic field, as well as usual applications [70].

material	$T_c(0)$ / K	$B_{c2}(0)$ / T	application area
NbTi	9.3	12 - 15	medium field: magnets up to 9 T
Nb_3Sn	18.3	25 - 29	high field: magnets up to 15 - 20 T
BSCCO 2212	95	175 - 225	highest field: inserts for magnets above 20 T
BSCCO 2223	107	107	medium field: e.g. power cables and current leads
*Re*BCO	92 - 95	120 - 250	highest field: inserts for magnets above 20 T
MgB_2	35 - 39	14 - 40	low to medium field: e.g. wiring in satellites

With the continuous increase in the availability of HTS and MTS, as well as technological progress in the last decades, new applications are envisioned, that may have not been available with LTS materials alone. While superconducting versions of an electrical (copper) machine can be made, with increases in performance and efficiency, other kind of applications are possible.

Superconductivity can then improve multitude of areas, to contribute with solutions on the lines of the Sustainable Development Goals (SDG) from the United Nations Development Program (UNDP) agenda [3]. Identified areas where superconductivity can make a direct contribution, in terms of the outlined SDG's [71], include:

- 6) Clean Water and Sanitation
- 7) Affordable and Clean Energy
- 9) Industry, Innovation and Infrastructure
- 11) Sustainable Cities and Communities
- 12) Responsible Consumption and Production
- 13) Climate Action

The Superconductivity Global Alliance (ScGA) is a recently founded consortium, aiming to partner of universities, research institutes and industry [72]. The aim is to expand the scope of superconductivity to areas where there is potential to enable new technologies towards

a sustainable society development. Additional examples for potential technology development include transportation (Maglev transport, zero-emission vehicles), quantum computing, power electronics, improved healthcare magnets (MRI, NMR, Proton Beam Therapy), and power transmission cables.

2.1.3 Resistivity and Critical Temperature

From this point on, the focus of the text is for Type II superconductors, and there may be some overlap in the concepts applicable to LTS, MTS or HTS, yet the focus will be done for HTS materials and cable concepts.

The critical temperature is a parameter that depends on the material composition. Similarly to the magnetic field vs temperature transition zones, also a transition zone exists within a narrow temperature window around the critical temperature (T_c) threshold, as shown in Figure 10:

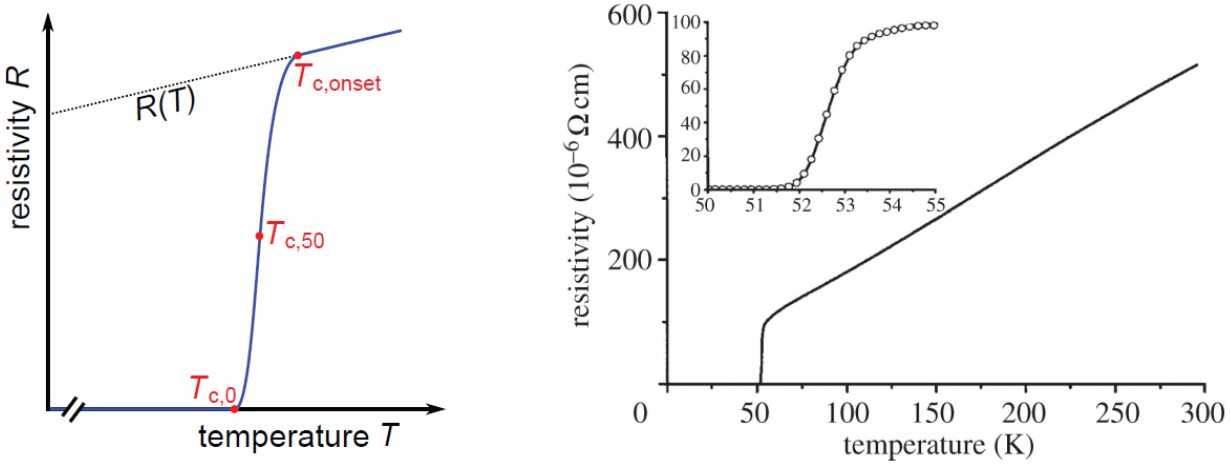

Figure 10: Type II Superconductor schematic, for the resistivity transition from superconducting to normal conducting states. Left: Virtually no resistance below the $T_{c,0}$ threshold, a mixed state between $T_{c,0}$ and $T_{c,onset}$, and normal conducting state after $T_{c,onset}$ [70]. Right: Resistivity vs Temperature for a LaSrCuO material, the transition temperature window between superconducting and normal conducting states occurs in a temperature window of about 2 K [73].

As previously mentioned, additional to the temperature, a magnetic field (self-produced or external) can further reduce the superconducting state. A high pressure is yet another parameter that can enable the existence of a superconducting phase, whose description is omitted in the present work, as such superconducting materials are not practical for high-current cable applications.

2.1.4 Operating in superconducting conditions

In this section it is explained how the parameters of temperature, magnetic field and internal current density inter-depend on each other, and define the region where superconductivity occurs, from now on for Type II superconductors. These three parameters, if plotted in a

three-axis plot define the so called critical surface, which is the threshold of values (temperature, magnetic field, current density) that should not be surpassed in order to operate into the superconducting state [53], as shown in Figure 11, including a comparison for the critical surface of LTS and HTS:

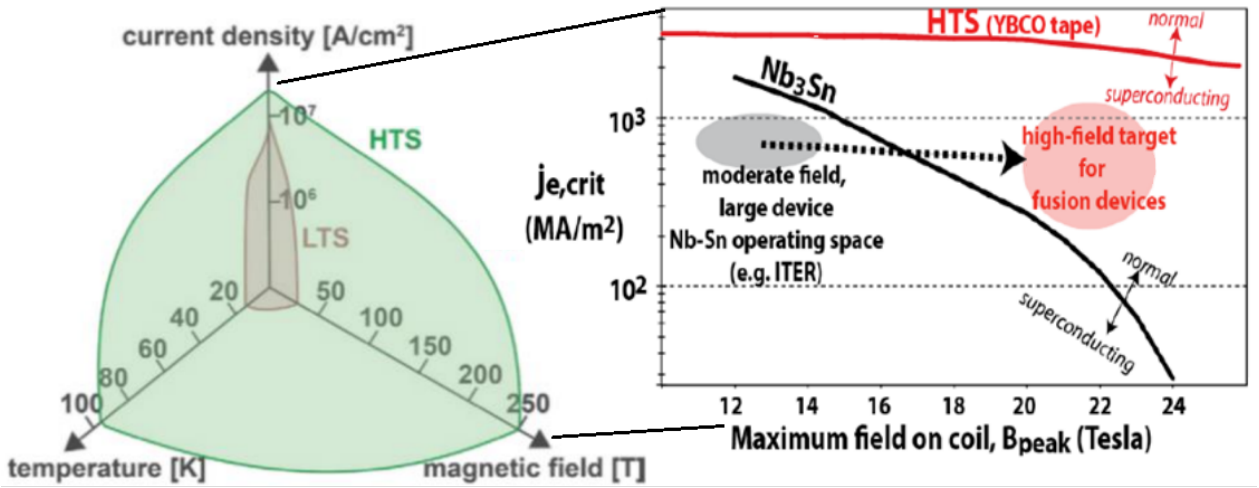

Figure 11: Schematic of the critical surface for a Type II superconducting material (LTS and HTS comparison), defined by the three critical interdependent values of T,B_c and j_c. To operate in superconducting state, the combination of T, B and j must be below the critical surface threshold. HTS largely expand the operation region of superconductivity for the three values [74].

Now, speaking about cables, in order to have a stable operation condition, the current density has to have a margin window from the critical current density value. This margin of safety allows to account fluctuations on the current, required to have a good performance and reduce the risk of losing the superconducting state. Similarly, a window temperature margin allows higher stability, hence a lower operating temperature may be beneficial.

For a high-current superconducting cable, the interest is to achieve a high current density, considering that the current by itself generates a magnetic field, and requires to be operating below the critical current. Hence these three values need to be reasonably set to have both a high-current value, that can be resilient if perturbations arise.

In general terms, outlining an operating current in a wire or sample always depends both on the temperature and surrounding magnetic field, as $j_c = f(T, B)$. It can be understood as follows:

- By setting an operating temperature T_{op} below the critical temperature T_c, a critical magnetic field B_c is defined at the temperature T_{op}.
- Feeding a current, the critical magnetic field B_c is reduced due to the self magnetic field B_{op}, generated by the current itself, to a value of $B_{c,op}$.
- The attainable operating current density point has a specific value j_{op}, formed by the combination of T_{op} and B_{op} .

- A safety margin window both for j_{op} and T_{op} is set, to maintain stable operation and endure possible fluctuation or perturbations.

A graphical description of a current operation point, considering the safety margins of operation for temperature ΔT and current density Δj, is shown in Figure 12:

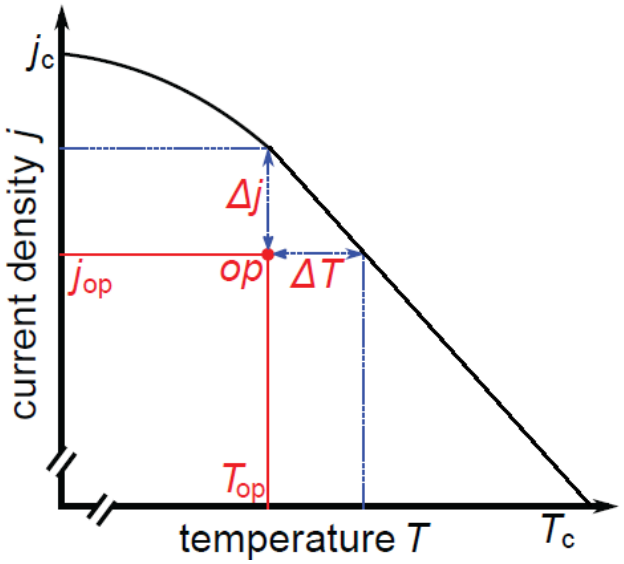

Figure 12: Operating point of a superconductor, plot of Current density vs Temperature, at a magnetic field value B_{op}. The safety margins Δj and ΔT from the critical surface, allow a stable operation that may tolerate fluctuations of temperature and current [70].

2.1.5 Power Law Equation for HTS

In the case of Type II superconductors HTS for high-current applications, considering a superconducting filament, it can conduct current up to a specific value. If this current is surpassed, the material starts to develop a resistance, which implies that ohmic heating starts happening too, and may lead to a temperature rise and the superconducting state being lost.

The resistance can be then measured from the voltage that is developed in the terminals of the filament. Based on experimental observations, an empirical equation has been outlined, that describes the electric field as a function of the current density. This is the so called "Power Law" shown in Equation 3, that applies to REBCO and other commercially available HTS:

$$E = E_0 \left(\frac{j_{sc}}{j_c} \right)^n \tag{3}$$

where E is the electric field measured between two terminals, j_{sc} is the current density in the superconducting region, J_c is the critical current density at the operating values of temperature and magnetic field, n is an material-dependent exponent fitting value that sets how fast the electric field changes with increasing current, and E_0 is the electric field criterion [75].

The electric field criterion is defined by the IEC International Standard 61788-1 as 1 $\mu V/cm$,

value often used for defining critical current density safety limit for high-current superconducting applications [76]. Hence, it is a value that has been practically found to be measurable by diagnostic voltage system, while being small enough so action can be taken to reduce or shutdown the current and avoid losing the superconducting state by joule heating. This is shown graphically in Figure 13.

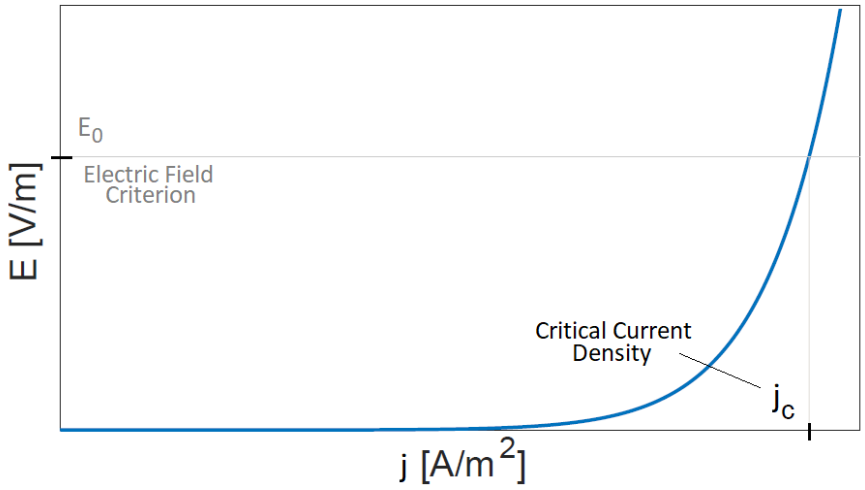

Figure 13: Electric field as a function of the current density, showing the electric field criterion E_0, that defines the critical current density j_c. This general electric field evolution trend can be observed, and fitted, both for LTS and HTS conductors, being a much faster transition in LTS [77].

2.2 High-current HTS cables

The manufacturing process for LTS has been developed since the 1960's and its industrial maturity has allowed the development of a variety of high-field applications for years [78]. As the discovery of HTS is relatively recent in comparison to LTS, "only" in 1986 [52], the commercial availability is comparatively more limited as of now, yet continuously increasing with the demands of HTS in high-magnetic field applications.

Manufacturing of LTS rely on extrusion and other mechanical processes, thanks to the ductility of the materials such as Niobium Titanium ($NbTi$), where long wires can be manufactured at long scale nowadays. In comparison, fabrication of HTS being more recent, using different manufacturing methods, and with still a relatively low demand, makes as of now HTS conductors more expensive than LTS.

HTS conductors generally come into the form of planar tapes, being Rare-Earth Barium Copper Oxide (REBCO) and Bismuth Strontium Calcium Copper Oxide (BSCCO) [79] the options that are commercially available more widely. The "Rare-Earth" of REBCO can be chosen among the 15 elements in the lanthanide family of the periodic table, being Yttrium and Gadolinium (Y,Gd) the ones more widely used.

REBCO is the HTS conductor variety with better performance at high-field applications, and its manufacturing process is significantly different than its LTS counterpart. REBCO

tapes are fabricated by atomic layer deposition process, growing up layer by layer the different materials necessary to form both the superconducting layer, and stabilizer coating, that ensure mechanical integrity and superconducting properties. A nickel alloy (hastelloy) is commonly used as the substrate and mechanical support to the tape, with different manufacturers slightly modifying the composition [80]. A schematic of the different layers than a REBCO tape is composed can be seen in Figure 14:

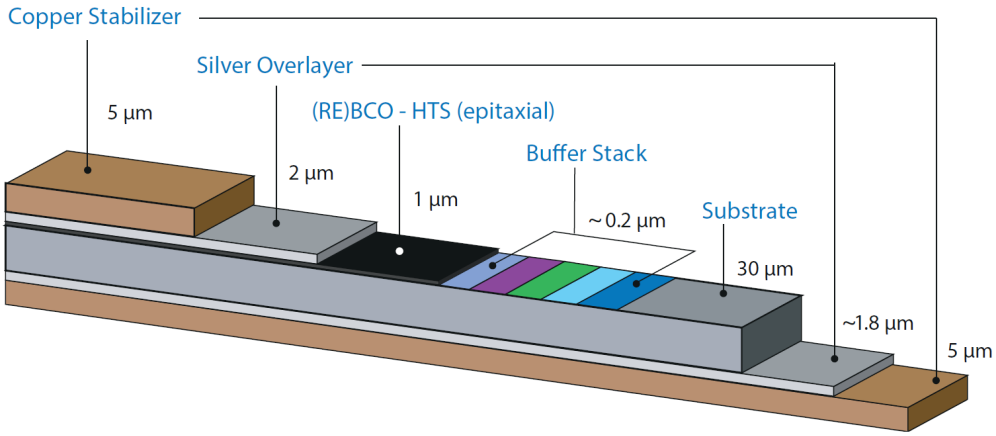

Figure 14: Schematic for the layers that conform a REBCO tape, note the superconducting layer forms only a small fraction of the total thickness. Substrate and stabilizer layers serving as mechanical structure and electrical path respectively, compose most of the tape volume [81].

In LTS filaments, a stabilizer material is added in electrical contact with the superconductor, to conduct the current in case the superconducting state is lost. On the same idea, REBCO tapes include a copper coating, and a silver layer , for the same purpose of protecting the superconductor in case of a transition to a normal conducting state.

Further testing can determine its adequacy depending on the type of application in mind, considering fusion, health care, particle accelerators, or fundamental physics research.

High-current HTS cables come in a variety of shapes, as they are designed by different research groups around the world, each one having a specific focus or criteria, in what parameters to optimize. However, perhaps most high-current HTS cable designs consider some form of twisting or transposition, that facilitates a uniform current distribution. This is an approach that may be necessary for AC operation, given the AC losses derived from the current profile of the operation itself.

Due to the planar form of HTS tapes, careful handling is required to produce transposition or twisting. Although the process might slightly reduce the HTS tapes performance, due to slight damage that may be produced in their superconducting layer, it is possible to develop good performance high-current cables. In high-current HTS cables, mechanical fatigue due to transient electromagnetic forces and as thermal cycling, can gradually degrade the performance of the cable, which adds to the design process research [82].

As AC losses are a lesser problem in DC operation, twisting and transposition is skipped for the simple-stacking concept. The higher cryogenic stability of HTS and proven stability of high-current experiments in simple-stacking, confirm that a high-current HTS cable is feasible with no twisting nor transposition. Furthermore, by eliminating the manufacturing step for twisting and transposition, a more cost effective cable can be produced.

A high-performance HTS cable is possible by using multitude of different cable configurations, using twisting/transposition or not, however, factors such as manufacturing robustness and costs are also important. There is no practical engineering benefit for a complex cable configuration, if the same performance can be obtained with a simpler geometry, where less manufacturing steps may reduce both costs and possibility of errors along the process.

Next is a brief overview of high-current HTS cable concepts potentially applicable to fusion magnets. The purpose is to better grasp the variety of approaches in the applied superconductivity community, divided between simple-stacking (DC operation) and twisted/transposed (AC operation) configurations. The examples also show where available, pictures of real samples, to get a better feel on the sizes and manufacturing of such cables.

The list is not exhaustive, updated cable versions may have been already disclosed and new proposals may be developed often, yet the purpose is to grasp different high-current cable approaches while using HTS tapes. Figure 15 shows a few examples as an introduction, while additional details are expanded afterwards.

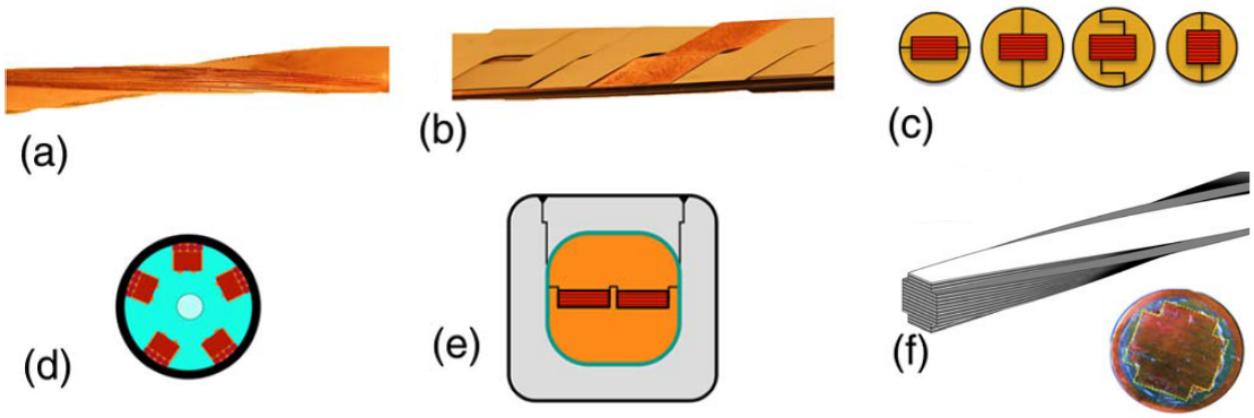

Figure 15: General overview of high-current HTS cables, by research groups worldwide. (a) TSTC. (b) HTS Roebel cable. (c) Round Cu-core TSTC. (d) Twisted REBCO CICC. (e) STARS. (f) HTS-CroCo. Adapted from [83].

2.2.1 Simple-stacking Concepts

- STARS (NIFS, Japan) [84, 85]
  The Stacked Tapes Assembled in Rigid Structure (STARS), is a collaboration project of the National Institute for Fusion Science (NIFS), Graduate University for Advanced Studies and Tohoku University. The HTS tapes are stacked, surrounded by a copper casing as stabilizer, and contained within a stainless steel jacket for mechanical support.

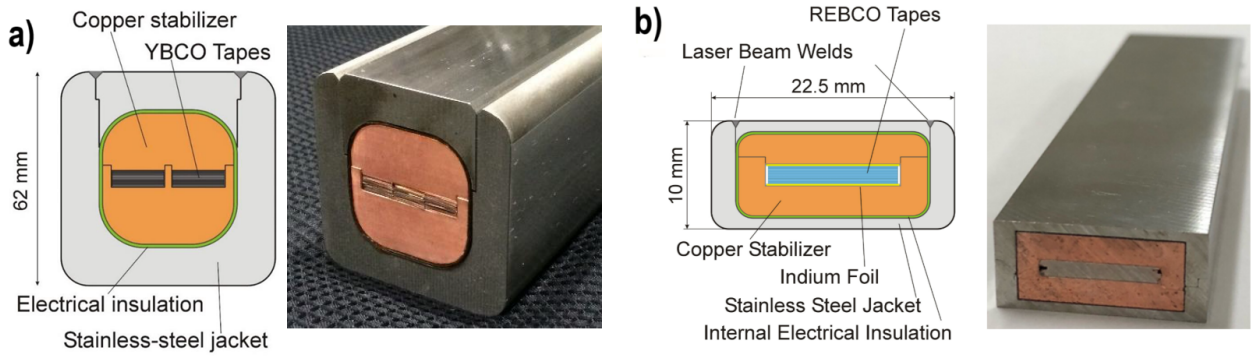

Figure 16: STARS conductor designs with external cooling. They feature REBCO tapes surrounded by a copper stabilizer, and a stainless steel jacket to withstand electromagnetic forces. a) 100-kA-class STARS (2015) [84]. b) 20-kA-class STARS (2022) [85].

- WISE (NIFS, Japan) [86, 87]
  The Wound and Impregnated Stacked Elastic tapes (WISE) is developed at NIFS. It features dry winding process, with the HTS tapes confined within a flexible spiral tube, that is then bent to the desired curvature of the coil. After, the tapes are impregnated with a low-melting point metal (U-alloy 60), so mechanical stresses in the HTS tapes are eliminated from the manufacturing process.

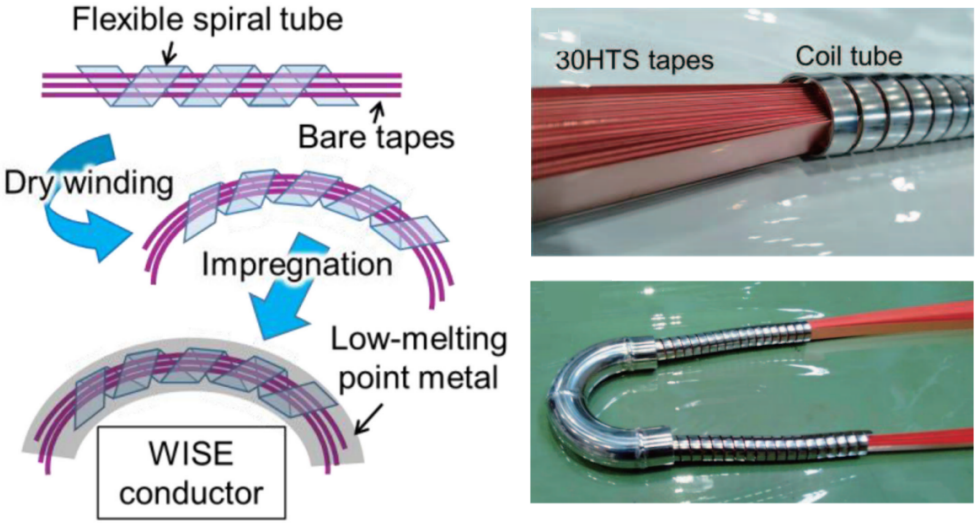

Figure 17: Manufacturing process for the WISE conductor. HTS tapes are bent while contained within a flexible spiral tube, and then impregnated with a low-melting point metal, which eliminates mechanical stresses otherwise produced during the coil shaping process [86, 87].

- SPARC TFMC (CFS/MIT, United States) [88, 89]
  The Toroidal Field Model Coil (TFMC) was a project to test the No-Insulation No-Twist (NINT) coil concept with REBCO tapes. It is on the lines of the SPARC reactor development, for a TFC made with HTS. NINT is a similar approach to simple-stacking, in the sense of using parallel HTS tapes with no twisting. It confirmed reaching at the HTS tape stack center, a peak of 20+ T at 20 K and 40 kA.

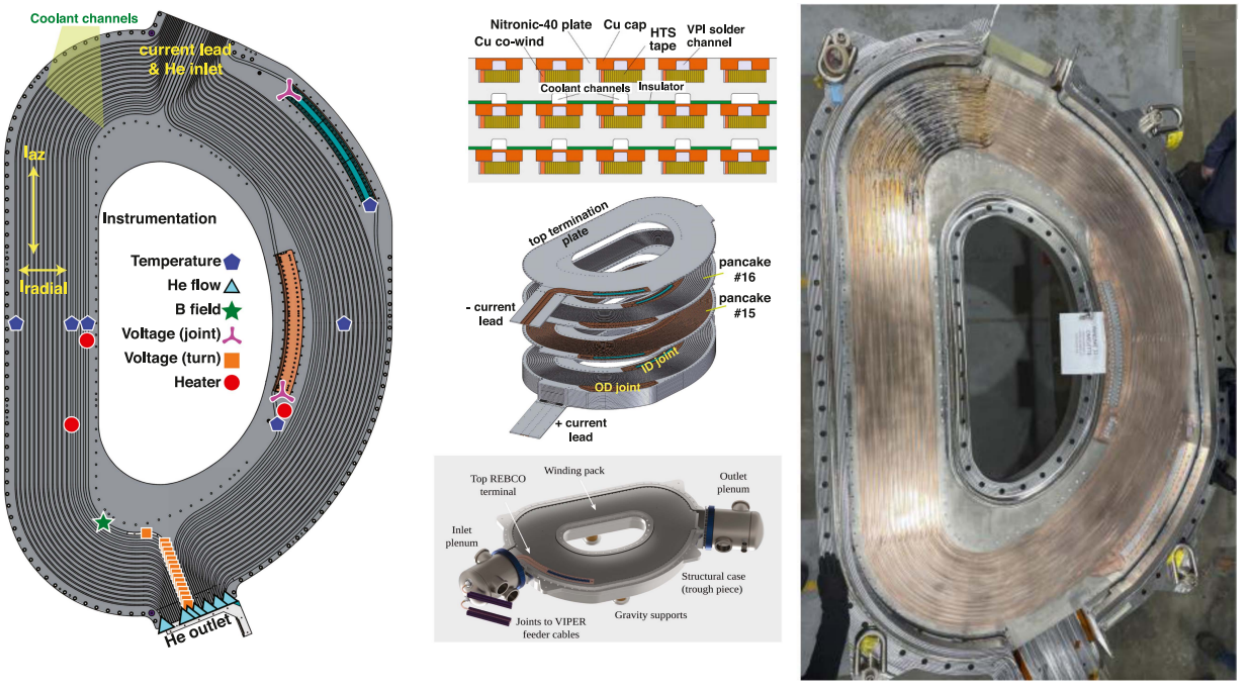

Figure 18: SPARC TFMC No-Insulation No-Transposition coil, where HTS tapes form a similar configuration to simple-stacking. The magnet is composed of 16 REBCO pancake coils connected in series. Left: Schematic of subsystems and assembly. Right: View of the exposed REBCO tapes with no twisting and no insulation [89].

2.2.2 Twisted/Transposed Concepts

- TSTC (MIT,United States) [90]
  The Twisted stacked-tape conductor (TSTC), developed at the Massachusetts Institute of Technology (MIT) and Tufts University. The HTS tapes are stacked, and afterwards twisted along their longitudinal axis. A number of later large-current HTS cable concepts are derived from this idea, such as [91].

- FAIR (NIFS, Japan) [92]
  Standing for Friction stir welding, Aluminum alloy jacket, Indirect cooling, and REBCO tapes (FAIR), meant to be used as large-current cable for fusion magnets. Concept derived from the TSTC configuration, it includes a stabilizer body made of an aluminum alloy, which has similar resistivity than copper at cryogenic temperatures. Once the stack of HTS tapes is finished, the cable is twisted, to facilitate a uniform current distribution in the HTS tapes.

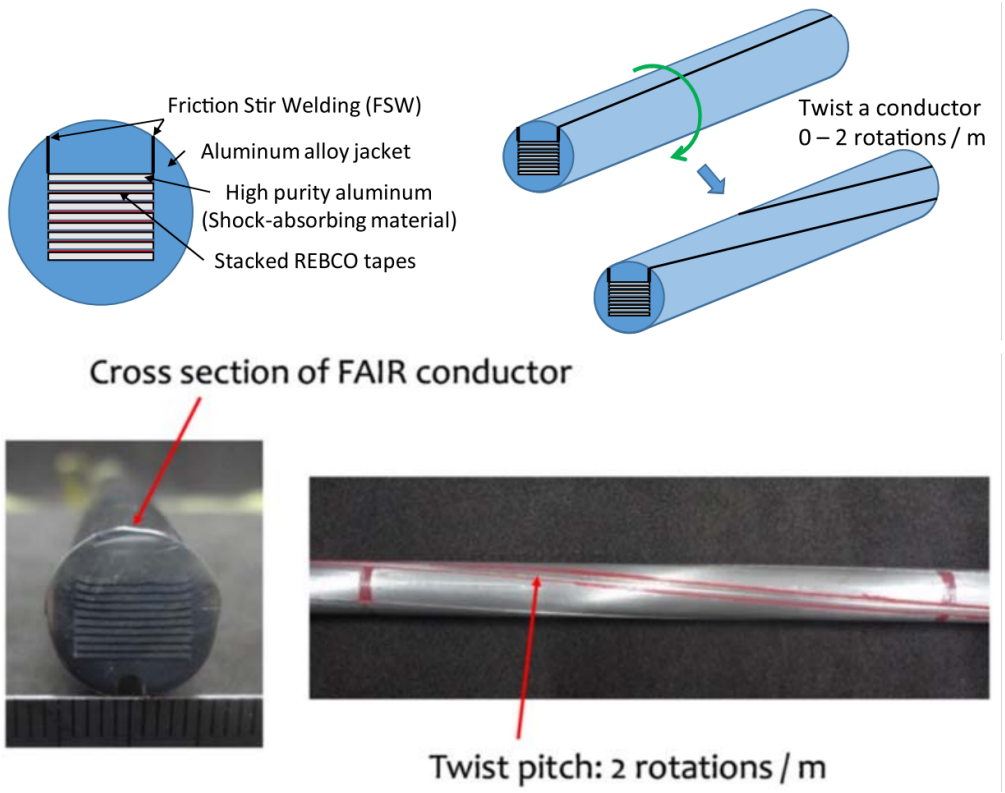

Figure 19: Schematic and prototype of the FAIR conductor. The stabilizer casing is made with an aluminum alloy, a groove carved for the HTS tapes stack, and twisted at a rate of 2 rotations per meter [92].

- VIPER (MIT/CFS, United States) [93]
  The Vacuum pressure impregnated, Insulated, Partially transposed, Extruded, and Roll-formed (VIPER) is a collaboration between MIT and CFS. Four stacks of HTS tapes are placed in a twisted copper former with a cooling channel inside. Finally, a copper jacket and a stainless steel jacket contain the assembly.

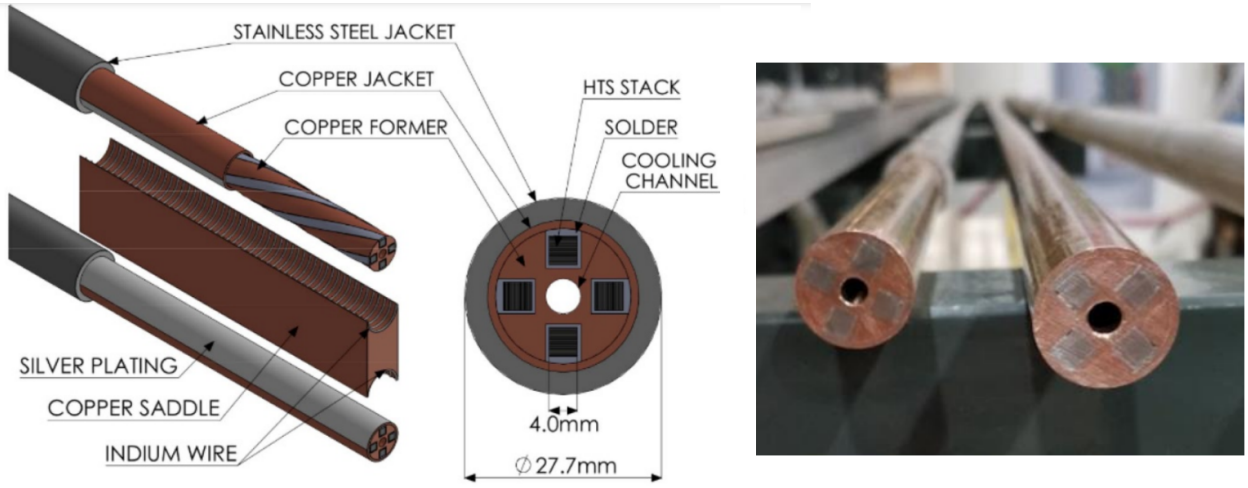

Figure 20: VIPER cable. Left: Schematic of the different components; including copper former with helical grooves and joint elements between two VIPER cables. Right: Cross section of two copper cores, with the stacks of HTS tapes visible [93].

- REBCO Roebel cable (KIT, Germany) [94]
  Manufactured first by Karlsruhe Institute of Technology and the Slovak Academy of Sciences. Roebel is a concept originally used in copper cables that reduces AC losses, achieved on HTS tapes by dividing in interlocking segments and twisting together the strands of HTS tapes. The flat squared cross section of the cable also makes it advantageous for racetrack coils and accelerator magnets.

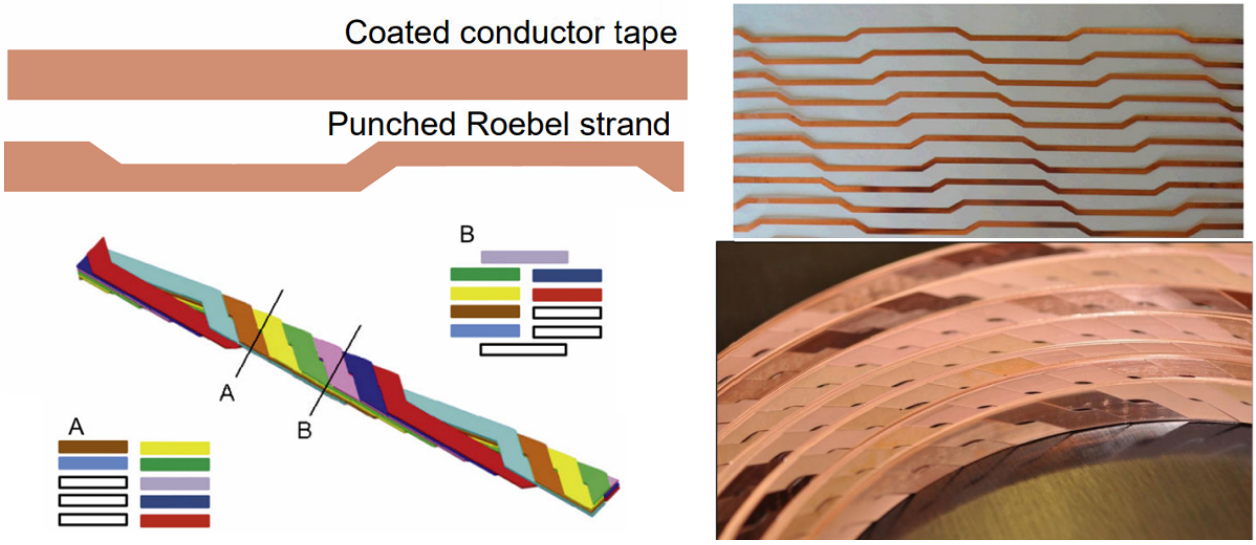

Figure 21: HTS tapes under Roebel configuration. Left: Schematic of the Roebel assembly process, including punching of the tapes for a Roebel strand, and interweaving of strands showing two cross sections. Right: Roebel HTS strands and assembled Roebel HTS cable. [94, 95].

- ASTRA (ENEA/EPFL/KIT/EUROfusion, Europe) [96]
  Concept devised as a collaboration project for EUROfusion, including ENEA, EPFL, KIT, and others; for the EU-DEMO Magnet System (specifically Central Solenoid AC operated magnet). Consists on an internally cooled CICC cable, with stacks of HTS tapes with separate stabilizers units, then joined together in a Roebel configuration. A single ASTRA CICC unit was tested in [97].

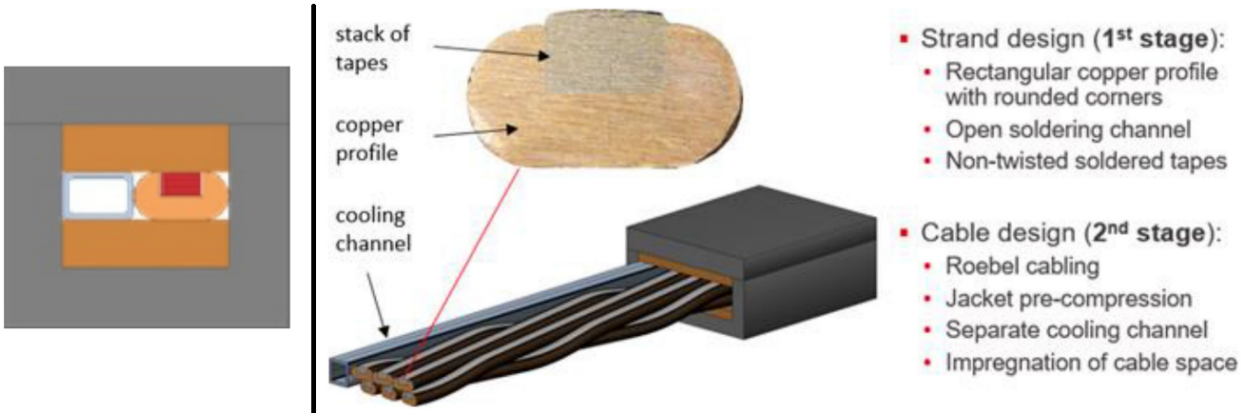

Figure 22: ASTRA conductor concept. Left: ASTRA cable with a single HTS tape stack, including a channel for internal cooling. Right: ASTRA cable design for EU-DEMO CS coil, with multiple stack units transposed in a Roebel configuration, as well as an internal cooling channel [96].

- Al slotted-core HTS conductor (ENEA, Italy) [98–100]
  Project developed by ENEA, within its Superconducting Laboratory. It features a cylindrical aluminum core with helical carved grooves, where HTS tapes are wounded. Meant to be operated at 20 K as of the HTS trend. Following on these steps, the SECAS CICC HTS cable concept is currently under development, while BRAST is a notable mention of a non-twisted concept of braided HTS tapes [101].

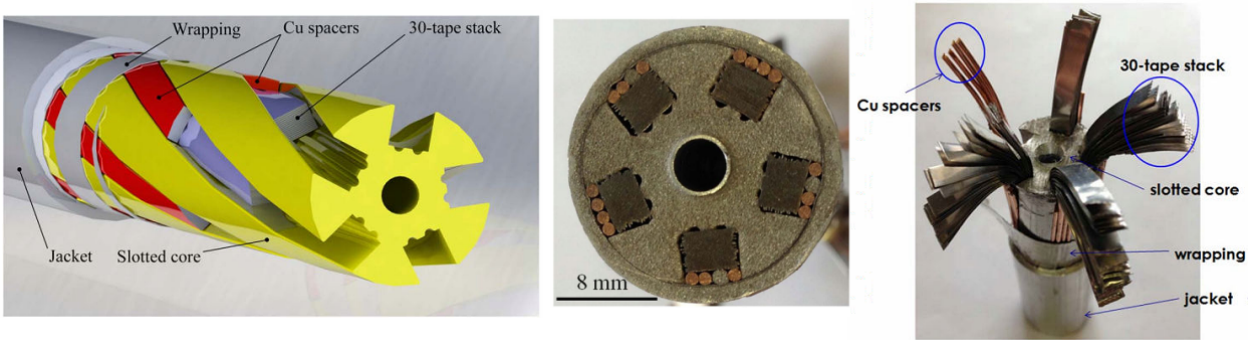

Figure 23: ENEA Al-slotted HTS conductor. Left: Schematic with Al core in yellow, and HTS following a twisted configuration around the center axis. Right: Cut of cross-section of the cable, making visible the HTS wound around the core [98].

- QisTac HTS conductor (ASIPP, China) [102]
  Concept proposed by ASIPP based on the TSTC approach, and to use a braiding of copper wire layers around the HTS tapes, for mechanical sturdiness. Thicker copper cables are wound around the twisted HTS tapes, while a second layer of braided copper wires surround the assemble, and is then soldered together. This circular HTS cable unit may be then used for e.g. a CICC cable to use in fusion magnets.

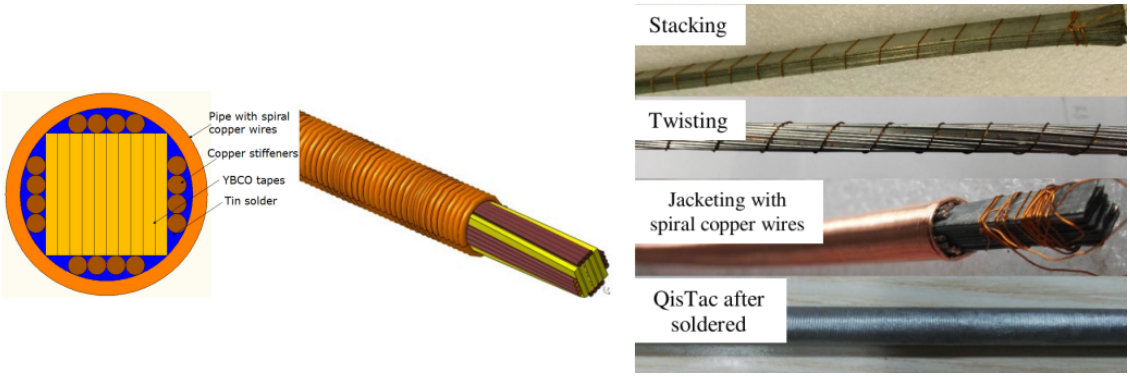

Figure 24: QisTac HTS conductor. Left: Schematic of two layers of copper braiding, one for a roughly circular cross section profile, to then use a second layer of copper wire braided around. Right: Manufacturing steps showing the braiding layers and the final soldering step [102].

- HTS-CroCo (KIT, Germany) [103–106]
  The HTS-CrossConductor (HTS-CroCo) concept was developed at Karlsruhe Institute of Technology (KIT), meant for DC current applications, including power transmission and fusion magnets. It uses stacks of HTS tapes using different tape widths, which increases the total cross section area for the superconductor region, filled with solder surrounding the HTS tapes, while being surrounded by a circular copper casing.

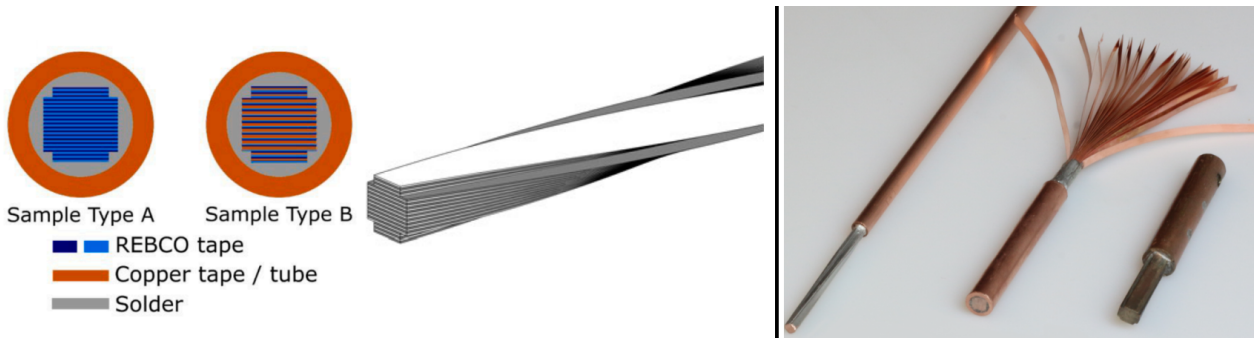

Figure 25: HTS-CroCo conductor. Left: Schematic with cross section sample designs, and a twisted stack of HTS tapes with two different widths. Right: Sample cutout on three shapes [106].

- Quasi-isotropic HTS cable (North China Electric Power University, China) [107, 108]
  Based on the quasi-isotropic HTS strand concept [109], to reduce the effects of critical current reduction due to the magnetic field anisotropy in HTS tapes. HTS tapes are

then arranged in four stack groups with perpendicular orientations, making the magnetic field lines parallel to the HTS tape width dimension in some of the strands. The cable at [110] is based on the same concept.

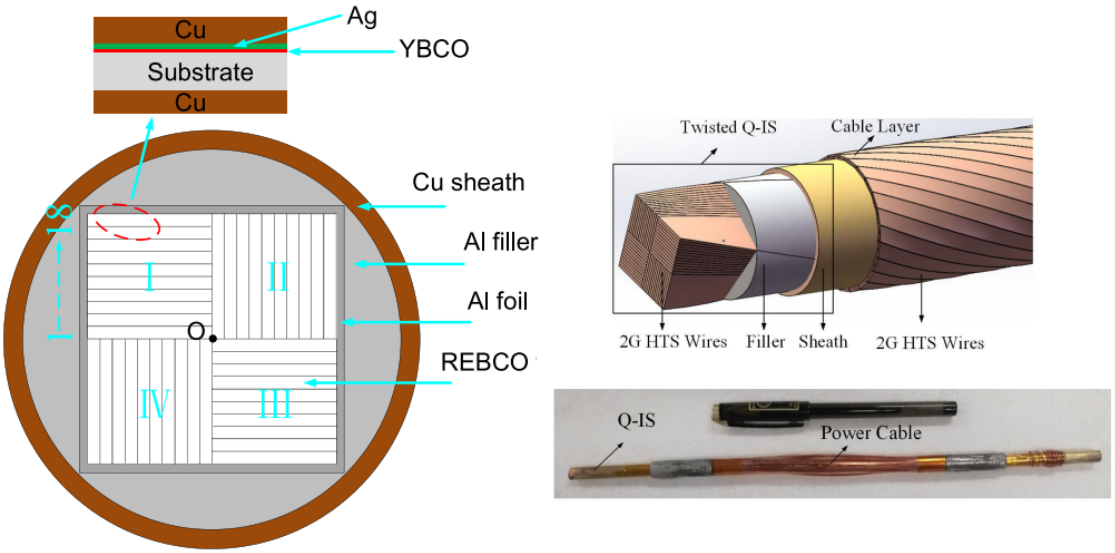

Figure 26: Quasi-isotropic (Q-IS) HTS cable. Left: Twisted four-stack HTS tapes quasi-isotropic strand, with an aluminum filler and copper sheat. Top right: Cable concept with a second outer layer of HTS tapes. Bottom right: Prototype test sample, for cable size dimensioning [107, 108].

- CORC (ACT/CERN/UTwente, United States/Switzerland/Netherlands) [111, 112] The Conductor on Round Core (CORC), consists on winding in a helical manner HTS tapes on a circular core, with a number of layers to increase the current handling capacity. The circular CORC cables allow some bending with marginal critical current degradation, up to the point of a minimum bending radius.

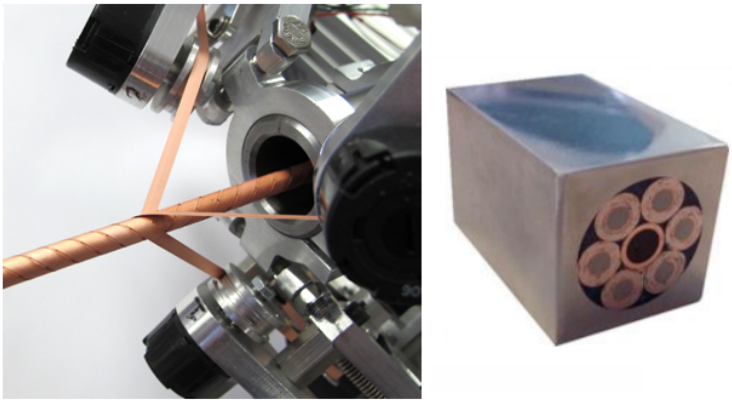

Figure 27: CORC conductor. Left: Cable manufacturing of HTS around circular copper tube core, with three HTS tapes wind simultaneously, and the process repeated for multiple layers. Right: CORC CICC sample, with 6 CORC conductors in a radial configuration, and an internal cooling channel [111].

3 Stable operation aspects of simple-stacking SC magnets

3.1 Non-Uniform Current Distribution (NUCD)

For a qualitative description, let's think what happens in normal conductors. Let's assume the case of 2 concentric circular conductors, with the same cross section, and different radius, they are in electric contact all along the surface contact, so current can be transferred. As the outer conductor has a larger circumference, it results in a higher resistance across its length ($R_1 < R_2$). Additionally, the larger radius also defines a larger self-inductance for the outer conductor ($L_1 < L_2$).

Hence, higher resistance and higher self-inductance result in a higher impedance for the outer conductor ($Z_1 < Z_2$). Then, if these conductors are in physical contact, as is the case in stacked HTS tapes, a higher share of the total current will flow through the inner conductor (either AC or DC current).

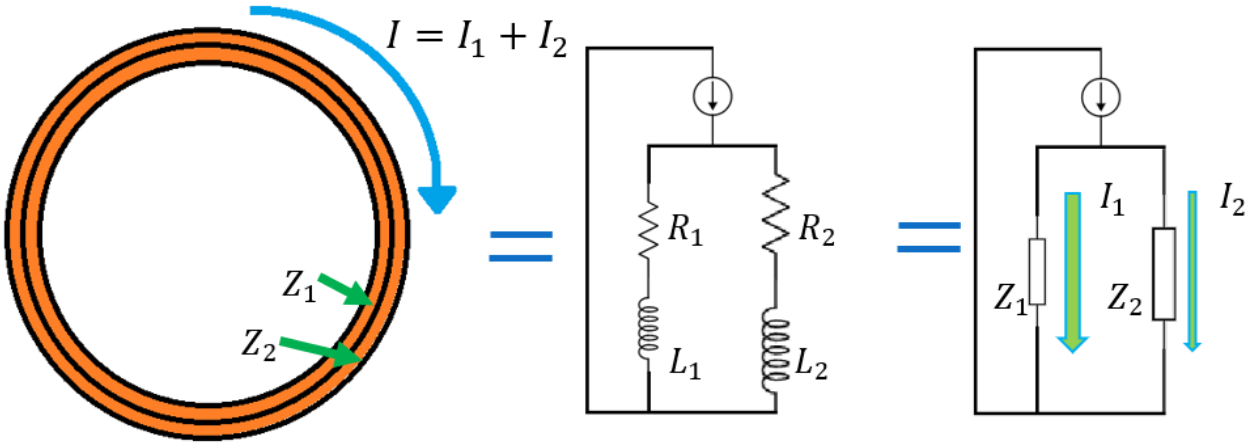

Figure 28: Impedance difference between two concentric conductors in electrical contact. Due to smaller length and cross section area of the inner conductor ($Z_1 < Z_2$), the larger impedance of the outer conductor causes a higher share of the total current to flow through the inner conductor.

In the case of high-current superconducting cables based on HTS tapes, twisting and transposition diminish this problem by equalizing the impedance of all the HTS tapes across the length of the cable, as all the tapes have roughly the same length along the cable.

As confirmed in [113], for a straight simple-stacking HTS cable, current can flow from one HTS tape to the other in a worst-case non-uniform fed DC current. As the total current gradually increases, the current share towards tapes lower in the stack occurs, when the critical current of one HTS tape is approached, and other superconducting paths nearby start conducting the excess current.

For DC current, or low-frequency AC current, a simple-stacking HTS cable wound in a coil, may be able to operate stably. Unavoidably, different impedance paths are produced across

different tapes in simple-stacking, a margin of ramp rate values (or operating frequencies in AC) up to a threshold may be achievable, the so called Ramp-Rate Limitation (RRL).

3.2 Circulation currents

Circulation currents can get formed into a superconducting cable, when current redistributes internally with any change in the input current. They can be understood as looping currents formed in order to balance the current in each strand or HTS tape towards, evolving towards the more stable current distribution according to the strands resistance and inductance.

The focus of the study here is analyze circulation currents that get formed and decay, either in trapezoidal input current, or ramp-down and decay after a constant current input. AC current behavior (when input current changes direction periodically) is not covered in the scope of the present project, yet a few mentions may be done when necessary.

Circulation currents have been observed often in large LTS magnets and HTS, as it will be mentioned later. First, a qualitative explanation is presented here in order to give a better grasp of how they get formed.

Assuming any SC cable or magnet, its superconducting strands may be connected at the endpoints in the current lead section, defined as a joint resistance. Additionally these strands may be electrically connected by an internal contact resistance through the stabilizer. As such, assuming a constant input current, any change in this constant current may form a redistribution of current between strands, causing heat losses when current passes through a non-superconducting path.

In Figure 29 it is shown a schematic of how circulation currents may form, assuming a cross-section of a straight HTS CICC cable. Circulation currents similarly get formed in coiled cables, where the decay time is longer due to the self-inductance of the cable itself.

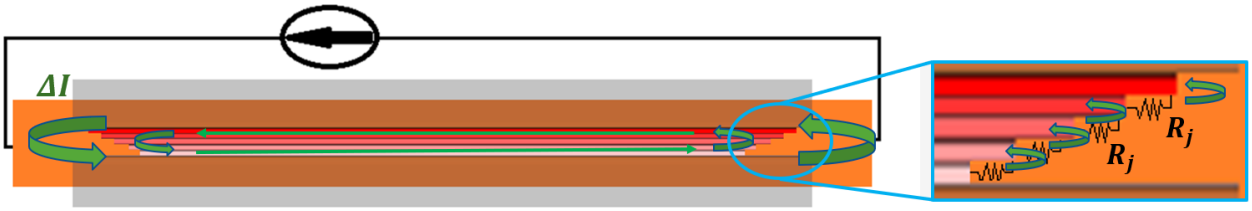

Figure 29: Circulation currents (ΔI) looping inside a simple-stacking CICC HTS cable, after ramping down the input current, and decaying when passing through the joint resistance (R_j) between HTS tapes. Furthermore, the point where the current returns depends on the ratio between longitudinal resistance and contact resistance, hence it may also occur in multiple positions along the cable longitude.

Hence, if circulation currents enhance the current in some superconducting strands, the critical current may be surpassed and a quench provoked. Twisted and/or transposed cable designs diminish the formation of circulation currents, due to the similar inductance of the superconducting strands, yet on simple-stacking their magnitude may be higher given the inductance variation between HTS tapes is always present.

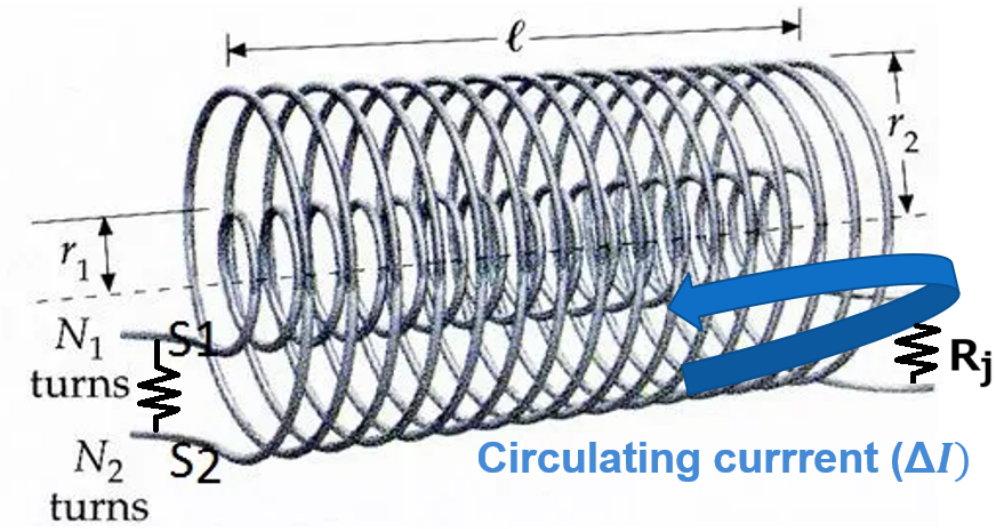

Figure 30: Schematic for two concentric solenoids (S_1 and S_2) connected in parallel, where circulation currents (ΔI) can flow from one to the other via the joint resistances (R_j). The geometry is equivalent to a simple-stacking cable being wound in a coil shape. If the filaments are HTS tapes, large circulation currents mean large current imbalance, which may quench the (internal) HTS tapes where the largest current share flows due to the lower impedance.

3.3 Ramp Rate Limitation (RRL)

Early on, it was observed that large LTS magnets needed to be charged slowly, in order to achieve nominal current and operate stably. This limitation of charging speed, may have also been due to early LTS cable designs didn't equalize the impedance in the SC strands, making that the ones with lower impedance quenched first, and the effect propagated to quench the whole magnet. The low heat capacity of materials operating at 4 K, also imply that small heat disturbances can easily rise the temperature and provoke quenching.

Once going towards Cable-In-Conduit Conductors (CICC) and manufacturing high-current magnets, despite AC operation is available, a large margin of stability is needed and equal impedance between strands, to ensure stable operation. Even so, fast ramp rate has a limit, threshold known as Ramp Rate Limitation (RRL) [114].

3.4 AC losses

While AC losses analysis is relevant for superconducting magnets, DC operated magnets in principle mainly experience AC losses during the charging phase, and in the cases nearby magnets may induce currents into it.

While AC losses exploration is not the focus of this work, we may briefly mention the situation that happens when stacked HTS tapes are twisted, which is an approach that slightly reduce the inductance variation between them.

As explored in [115, 116], a comparison via numerical calculation was done, to observe the

AC losses reduction that may be attained when twisting a superconducting cable, comparing the cases for LTS cables with circular strands, and stacked HTS tape cables. A comparison for these cables is shown in Figure 31:

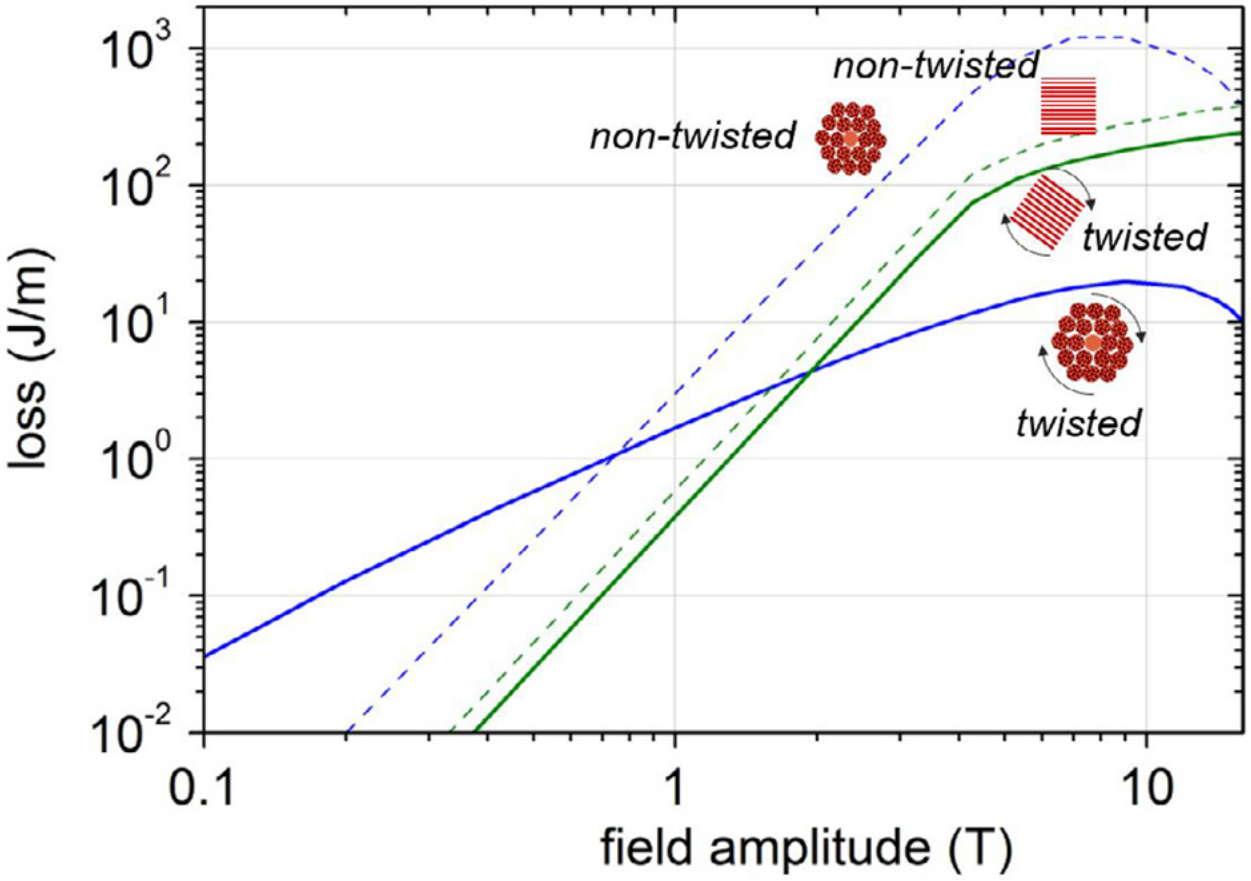

Figure 31: Comparison of AC losses for LTS and HTS cables when twisting is applied, as function of the magnetic field. At high magnetic field there is a two order of magnitude reduction for LTS cables, while for HTS the reduction is within a more modest 36% for most of the magnetic field range calculated [116].

The AC loss reduction may be up to two orders of magnitude in the LTS cable case, rather significant for stable operation. In the case of HTS twisted stacked cables, the AC loss reduction is modest, of around 36%.

Furthermore, thanks to their higher critical temperature, HTS have the advantage of being able to operate at higher temperature compared to LTS. For example, if choosing an temperature operating temperature of 20 K, it gives a two order of magnitude increase in the heat capacity of e.g. copper, used as a stabilizer (see Figure 32).

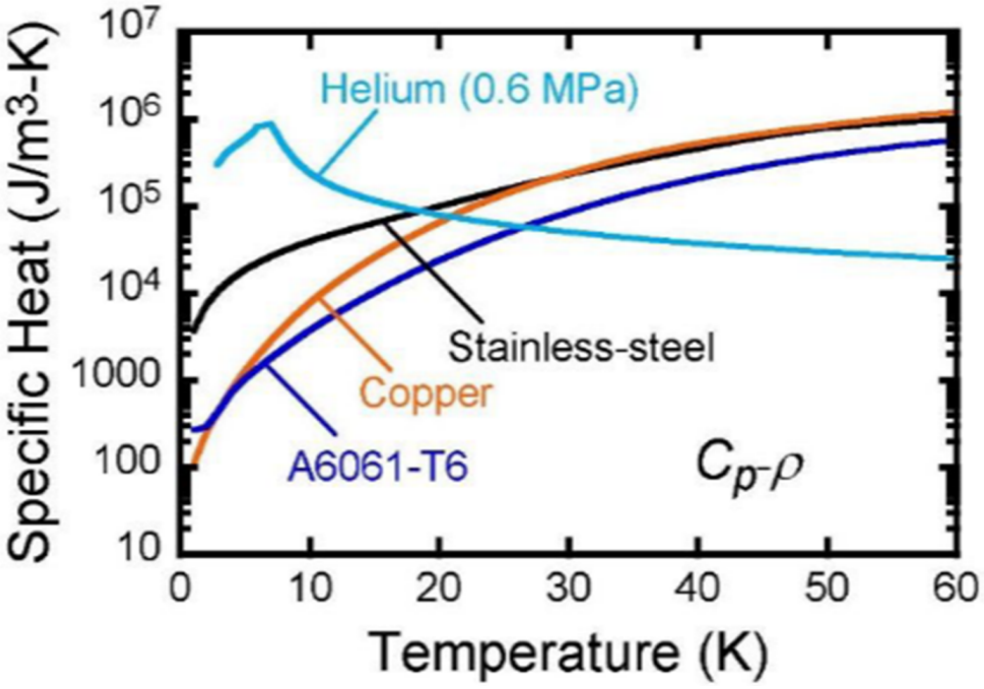

Figure 32: Heat capacity for helium and metals commonly used in high-current superconducting cables, as function of temperature. Note the two order of magnitude increase for metals, when going from 4 K to 20 K, that provides enhanced cryogenic stability in HTS operating at higher temperature compared to LTS [117].

The increased heat capacity implies that for the same amount of energy, temperature rise of materials is lower by operating at higher temperature, as it will be shown in a numerical calculation later. This in a simplified zero-dimensional heat calculation, as the increased heat capacity may cause localized heating, that requires for a more detailed thermal calculation to describe it.

3.5 Quench and Damage

A quench in a superconductor means that the superconducting state is lost, when any of the three critical parameters is surpassed: temperature, magnetic field or current density. As the material becomes a normal conductor, a resistance is formed in the material, which may pose a significant problem if a high-current is at the moment flowing through it.

Then, if a superconducting strand quenches while carrying current, the resulting resistance starts generating joule heating, which may rapidly start increasing the temperature, permanently damaging the strand. That is the reason why superconducting cables need the use of a stabilizer, which is a conducting path where current can flow in the case of a quench, to protect the superconducting strands of damage. Figure 33 shows quench damage observed in two simple-stacking HTS cables, due to mistakes in the detection and current feeding design:

Figure 33: Quench experienced in simple-stacking HTS conductors. Left: A NUCD may have enhanced localized heating in the current lead, rising the temperature that led to a quench [118]. Right: For STARS conductor, a mistake in the quench detection led to a late response when a quench was starting, that led to damage and burning of the sample.

In the case of NUCD, precisely the current imbalance may cause a quench, if the current in some strands becomes higher than the critical value, and it can not timely propagate to other superconducting strands or the stabilizer. If there is inductance variation among the strands, it is necessary that the contact resistance between strands to be low, so the current can flow through the stabilizer and perhaps transfer to other superconducting strands that are still superconducting.

While the example here shows a case for quench damage in HTS, this was deemed because of mistakes in the operation of the experiments and current lead connections, rather than fundamental limitations in the materials. On these lines, in the next section, it is shown a list of historical examples where premature quench was caused by NUCD or other reasons, and how HTS experiments have achieved more stable operation, compared to a number of LTS experiments.

4 Historical examples regarding stability in SC magnets

A SC cable may be more stable if the current in all the strands is the same, which implies that each SC strand carries an equal share of the current, so they all remain with enough margin from the critical current.

The gradual development of large SC magnets, initially from LTS, has allowed to determine that in order to achieve a same current share, twisting and transposition of the strands is necessary. This makes for the strands to have equal impedance and diminishes NUCD, which facilitates a stable operation [119].

Conveniently, for HTS operating at higher temperatures (< 20 K), there is a larger heat capacity and overall cryogenic stability available [117], meaning that the conductor can be more resilient to heat disturbances. This is a significant difference with LTS, where a low heat capacity implies that temperature can easily rise, plus the lower critical temperature means a margin of about 2 K for LTS, where for HTS can be about 10 K.

For large current HTS cables made with HTS tapes, twisting and transposition is commonly used [93, 115, 120–122], yet seems to be less of a need and more of an option in HTS, as twisting gives a marginal reduction in AC losses [116]. Additionally, a number of bending steps may degrade the critical current of an HTS tape if surpassing the tolerable bending radius (as of now on the range of 10 mm for a number of manufacturers for a single HTS tape [123]).

The inductance variation among stacked HTS tapes was evaluated in [124], remaining within a 5% margin, deemed a minor concern for the NUCD, while a number of simple-stacking experiments have confirmed stable operation even in a NUCD condition. However, how stable a simple-stacking HTS under NUCD and inductance variation is still uncertain experimentally for large magnets. A number of examples follow for experiments related with unstable (in LTS) or stable (in HTS) operation of previous experiments.

For the aim of this project, the HTS simple-stacking approach is explored, which means the HTS tapes are not twisted nor transposed, meant for DC current large magnets. By reducing the number of manufacturing steps through the assembly of the conductor, the overall cost may be reduced, which is beneficial to large budget projects such as fusion reactor applications. There is a growing interest to explore non-twisted HTS cable concepts for DC current magnets [125–127].

4.1 LTS

The following examples overview cases for large Cable-In-Conduit Conductors (CICC) experiments. The earlier examples, (before 2010 or so) show unstable operation, lessons learned from the research allowed to improve the CICC designs, to be able to have a more uniform current distribution in the cable.

While circulation currents, it has been found, are unavoidable in a superconducting cable in CICC configuration, stable operation can still be achieved both with LTS and HTS.

- 1994 - Demo Poloidal Coil conductor (DPC-U)
  The conductor had electrical insulation between the superconducting strands, in order to reduce coupling losses. During the charging process it was observed premature quench, even at slow charging rate. It was determined that NUCD caused the premature quench, as the strands that lost the superconducting state couldn't easily transfer the current to nearby strands due to the insulation. By applying heat it was determined that by making normal state the strands that were taking higher current a more uniform current distribution was possible. Figure 34 shows charging events and the point where premature quench was detected, at currents lower than the design value of 30 kA and 5.29 T [128].

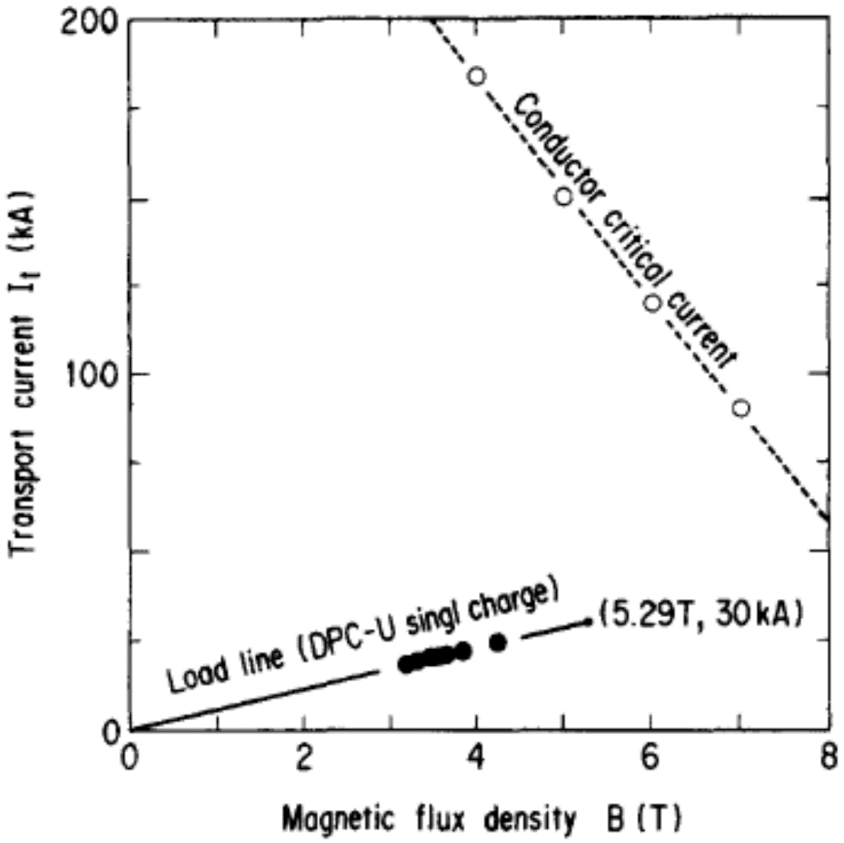

Figure 34: DPC-U conductor transport current tests. The design values where 30 kA and 5.29 T, however the cable consistently quenched at lower values, as indicated by the black dots in the plot. The reason, attributed to the NUCD formed in the superconducting strands, which caused the ones with lower impedance to quench first and degrade the overall maximum current achievable [128].

- 1998-2003 - LHD Poloidal Coils [129, 130]
  During the qualification testing for LHD magnet system, a test was done, named Experiments on a Single Inner Vertical coil (EXSIV). Extra AC losses were detected, compared with the expected value, and different scenarios considered for its possible causes. It was determined that slight asymmetry in the winding of the filaments, caused by the periodic NUCD in the cable, may have produced local coupling losses in some filaments that added to the total AC losses. Figure 35, shows numerical calculation of

the AC losses matching with experimental measurements.

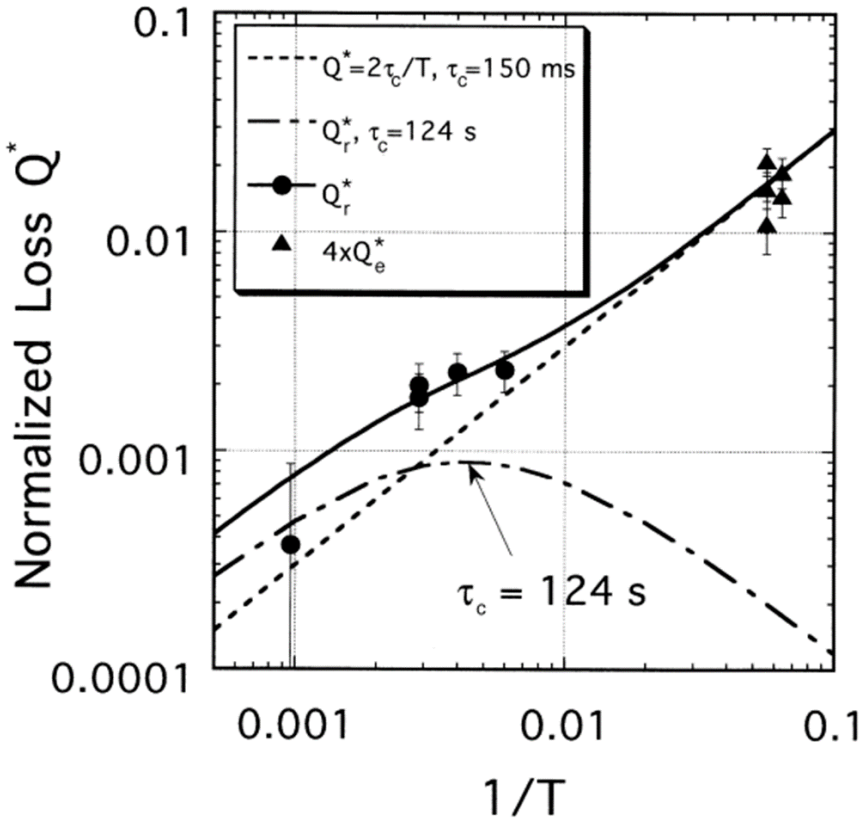

Figure 35: Numerical calculations of AC losses observed in EXSIV experiment. The continuous black line is the sum of the two dotted lines, which correspond to coupling losses with different time constants. The black dots and triangles correspond to punctual experimental measurements at specific frequencies, matching along the numerical calculation [129].

For a second experiment, a changing AC was applied to the sample in order to measure the AC losses. The experimental observations showed higher values than the theoretical prediction, which couldn't be completely clarified the reason why, but it was speculated that a higher number of asymmetries in the strands caused more coupling losses than the original expectation, as shown in Figure 36.

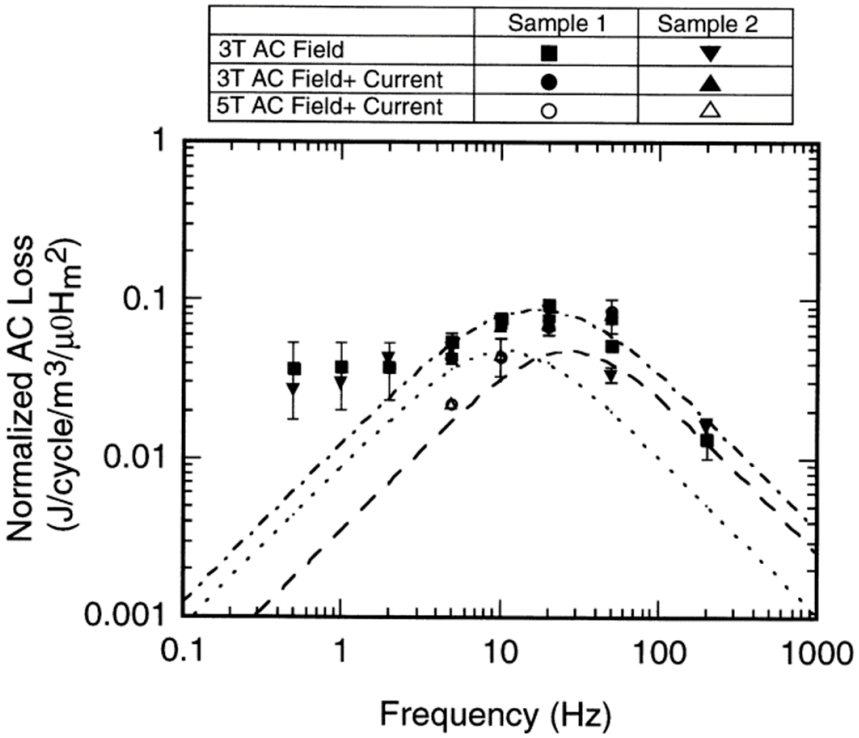

Figure 36: Comparison of total AC losses, for a changing AC magnetic field at different frequencies, in the EXSIV experiment. There was higher AC losses in the experiment at low and high frequencies, with a better matching at mid frequencies. Although the origin wasn't clarified, it was speculated that multiple asymmetries in the strands winding caused them [130].

2006 - SST-1 CICC [131]
A CICC was prepared for qualification tests, in order to be used in the Steady State Tokamak 1 (SST-1) magnet system. The sample was tested under different conditions, including the resilience in the case of the formation of a NUCD. A reduction of the quench current was observed, when intentionally producing a NUCD by heating some of the strands, and applying increasingly faster ramp rate. As a representative case, it was observed that when a NUCD was about 40%, the quench current was reduced by about 5% at 500 A/s.

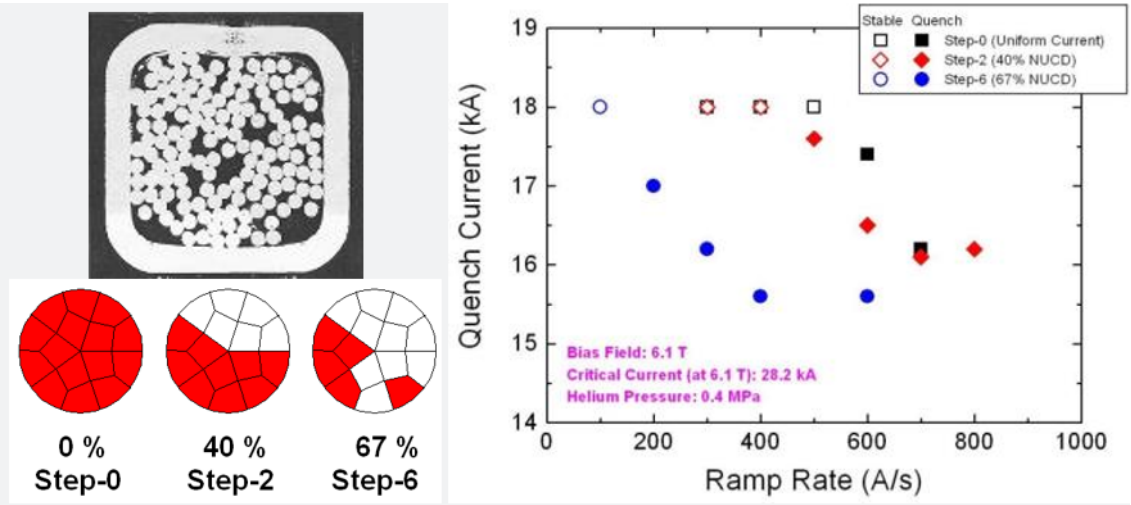

Figure 37: Experiment for stability under NUCD, of the CICC conductor used for the SST-1 magnet system. By causing intentional NUCD via localized electric heaters, a reduction in the quench current was more enhanced, and dependent on the ramp rate that the sample was charged [131].

2009 - ITER PFCI [132]
The ITER Poloidal Field Conductor Insert (PFCI) experiment which was tested inside the ITER Central Solenoid Model Coil (CSMC). The PFCI was made with NbTi, as a relatively low magnetic field was expected (B$\leq$ 6 T). A test at different load factor was performed, (which is the ratio between operating current and critical current of the cable (I/I_c), to observe the current sharing temperature T_{cs} . While the low load factor case (I_{PFCI}=6 kA, B_{CSMC}= 5.9 T) developed a voltage as expected, the high load factor case (I_{PFCI}=55 kA, B_{CSMC}= 5.15 T) experienced a fast voltage rise and quench. The reason was deemed due to the NUCD formed by the inner strands of the PFCI experiencing a high field and quenching earlier, which can be seen in Figure 38:

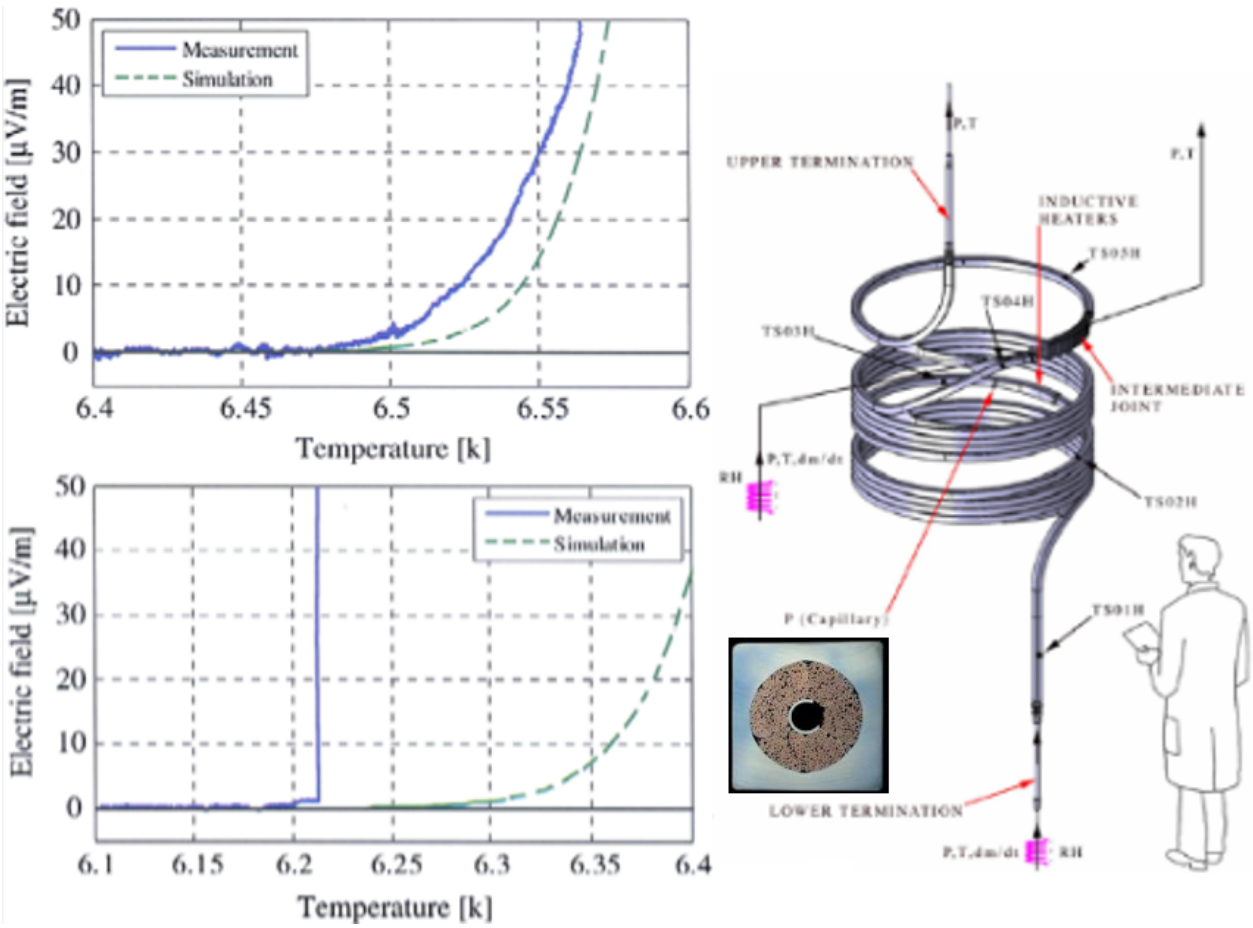

Figure 38: Experimental tests of the ITER PFCI coil inside the ITER CSMC module, tested under different load factors, and compared with a numerical simulation. While at low load factor (top plot) the voltage development is as expected by the calculation, at high load factor (bottom) there is a premature quench, possibly caused by the higher self field experienced by the inner strands [132].

2018 - JT-60SA CS1 module [133]
During the testing of one of the modules of JT-60SA, the CS 1, circulation currents detected via decaying magnetic fields, with different decay constants. As circulation currents are caused by superconductors connected by an electric path, it was confirmed with a second experiment that, although an unintended effect, they can appear both in long-coiled and short-straight CICC samples.

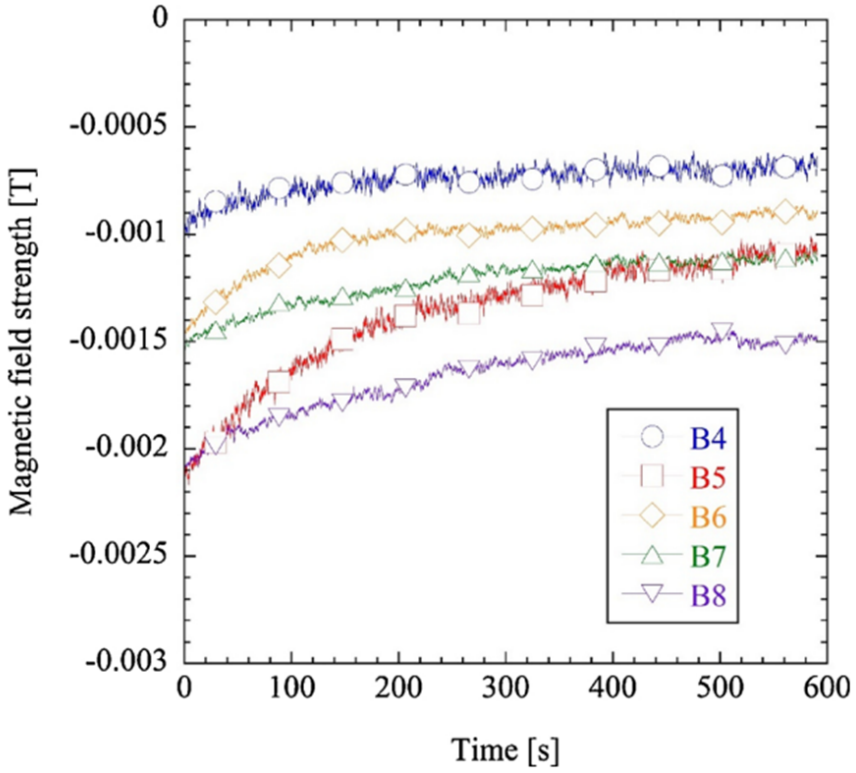

Figure 39: Decaying magnetic field after de-energization, produced by circulation currents during the JT-60SA CS1 module tests. The decay constants have slightly different values depending on the position where they were measured [133].

2021-2022 ITER TFC joint samples [134, 135]
During the testing of ITER TFC joint samples, residual magnetic field was similarly observed with slightly different decay constants, for a twin-box joint configuration. The difference in decay constants was speculated due to some of the strands having lower joint resistance than others, via a numerical calculation comparison.

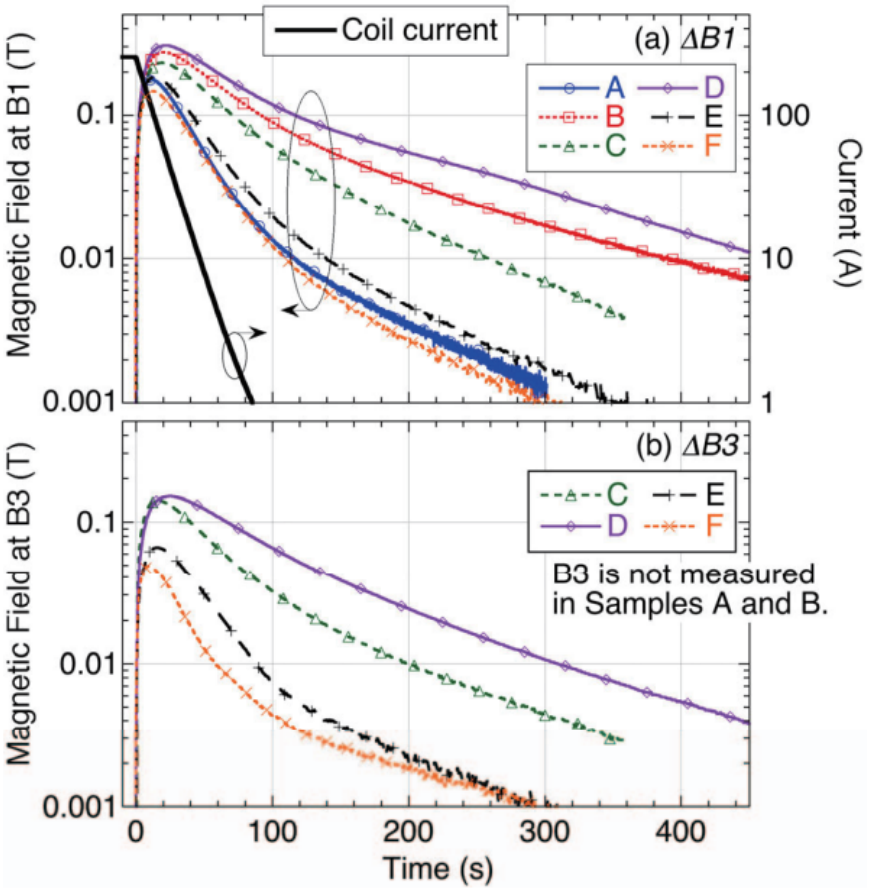

Figure 40: Residual magnetic field observed in ITER TFC joint samples, measured at different positions. The varying decay constants observed, was speculated it was caused due to variation in the joint resistance at different points, as well as dependent on temperature and current tested [135].

4.2 HTS

In NIFS there are three HTS cable designs in development, as it was introduced in the previous section for HTS cable designs: STARS and WISE for simple-stacking configuration [45, 85, 87]; and FAIR conductor for a twisted stack configuration [92].

While there are several HTS cable configurations that have confirmed stable operation at large current for twisted or transposed configurations at AC operation, the examples below focus on simple-stacking HTS cables. These are meant to be operated on DC current, tested under trapezoidal current input or by induction, so input current flows in the same direction.

The last three examples mentioned in this section, are the ones described within the scope of this thesis, using the simple-stacking approach. They are included here with the purpose to track historically these more recent developments, and an example of experimental data is shown for each. While for LTS cable quench current starts noticeably degrading at ramp rates of around 800 A/s and more, on HTS cables the ramp rate can consistently go up to 2 kA/s with no reduction in the quench current [131].

A direct comparison cannot be made between earlier LTS examples and the following HTS examples. Operation conditions, impedance difference between strands, cooling capacity for heat extraction or safety margin from operating to critical current is different among earlier LTS cables compared to the simple-stacking concepts with HTS shown here. Decades of research experience and operation of large-current LTS cable have allowed to reach robust and stable operation concepts either on AC or DC current. The point is to briefly illustrate that stable operation is available with HTS under NUCD and fast ramp rates, where a premature quench may have likely been reached if such cables were LTS conductors operating with those same conditions.

- 2014 - 100-kA-class STARS conductor [136]
  A 3 m racetrack coil sample high-current HTS conductor, which was an earlier validation for the simple-stacking concept in a coil shape with inductance variation. The sample also included a low-resistance bridge-type mechanical joint, to explore stability of interconnected HTS segments. A current was induced in the conductor by ramping the bias magnetic field, stable operation up to 1 kA/s achieved with no premature quench. Peak obtained current in the sample were 118 kA at 4.2 K, while a current of 100 kA was sustained stably for 1 hour.

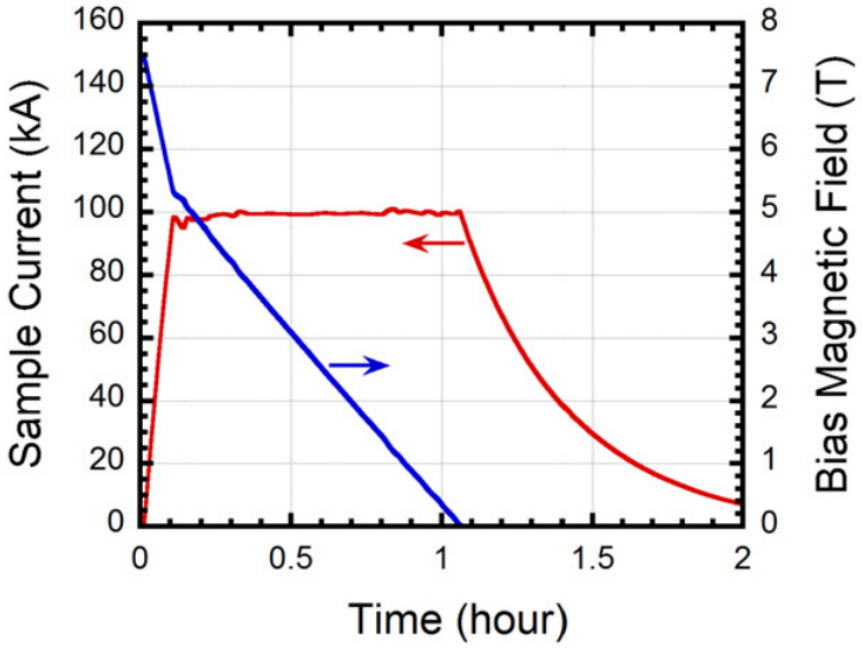

Figure 41: Current induced by ramping a bias magnetic field (blue line) in the 100-kA-class STARS experiment at 4.2 K. A current of 100 kA (red line) was sustained for 1 h with no premature quench [136].

- 2019 Short-straight HTS cable (1.3 m) [113]
  Experiment to test the resilience of 5 REBCO tapes (4 mm) under a worst-case scenario of NUCD, produced by feeding the current from the edge of one REBCO tape only. Stable operation and current transfer between stacked REBCO tapes is observed in the voltage measurements, while a numerical calculation reasonably reproduced the experimental observations [137].

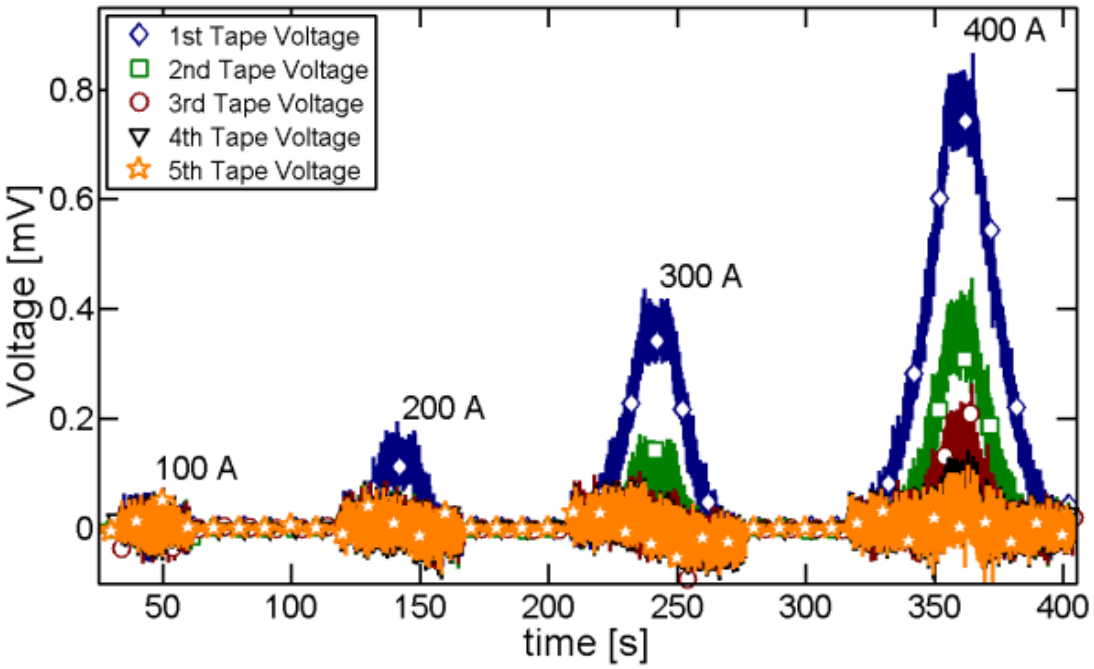

Figure 42: Voltage measurements of the Short-straight HTS cable (1.3 m) under worst-case scenario of NUCD. Trapezoidal input current was applied at increasing flat-top current value, with no premature quench detected. The step-wise increase of voltages in trapezoid shape indicate a step-wise transfer of current among REBCO tapes [113].

- 2022-2024 - 20-kA-class STARS coiled sample (6 m) [85]
  High-current HTS cable 20-kA-class STARS experiment, coil with 3-turn and 15 HTS tapes of 12 mm width. After trapezoidal input current, a residual magnetic field lasting for up to 100 s was detected, indicating circulation currents. Stable operation at 18 kA (load factor of 90%), 1 kA/s, 20 K, 8 T; and stable operation up to 2 kA/s with no premature quench [85].

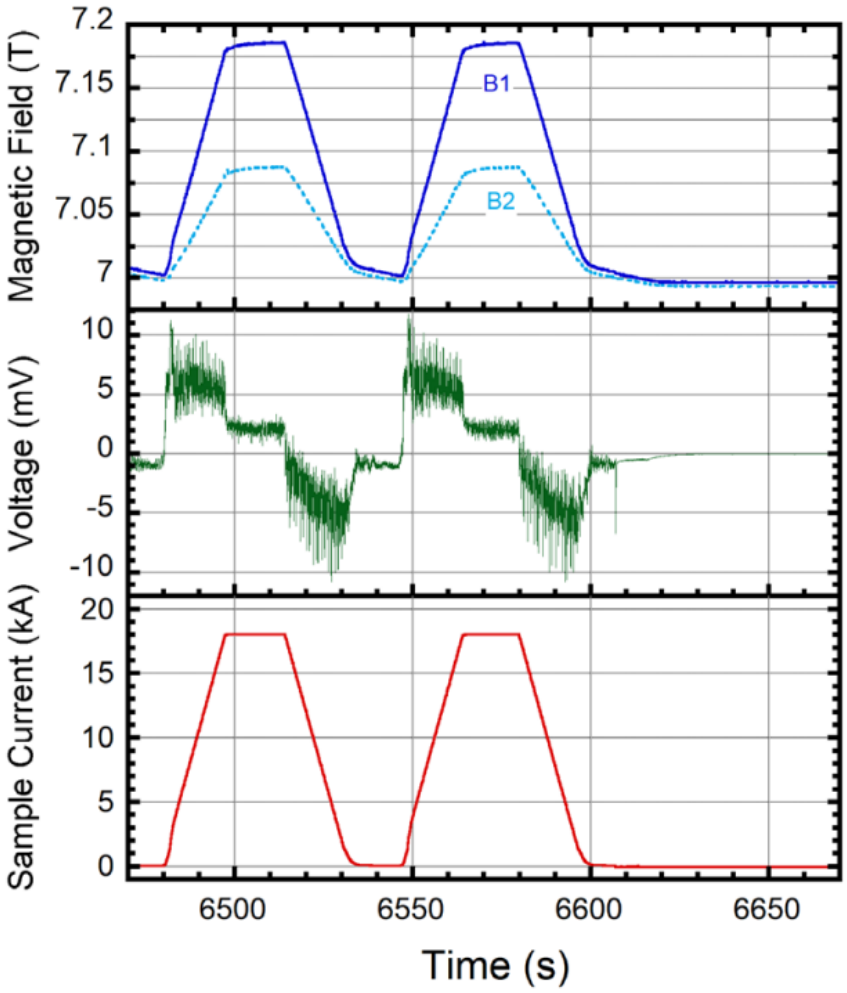

Figure 43: Test of the 20-kA-class STARS conductor under 100 repetition testing at 18 kA and 1 kA/s, last two pulses shown completed with no premature quench. Voltage measurements show stable low value as expected, while the magnetic field measurements shown a decay after the current became zero, caused by circulation currents decay [85].

- 2023 - L-RAISER HTS solenoid
  The Inductance (L) RAISing ExpeRiment (L-RAISER) solenoid experiment is part of the explorations done for this projects, regarding stability of HTS under fast ramp rate and inductance variation. 30-turn and 5 HTS tapes 4 mm width. Stable operation with no RRL nor premature quench was obtained at 550 A, 77K , 2 kA/s. In the following chapters a detailed description of the experiment is presented

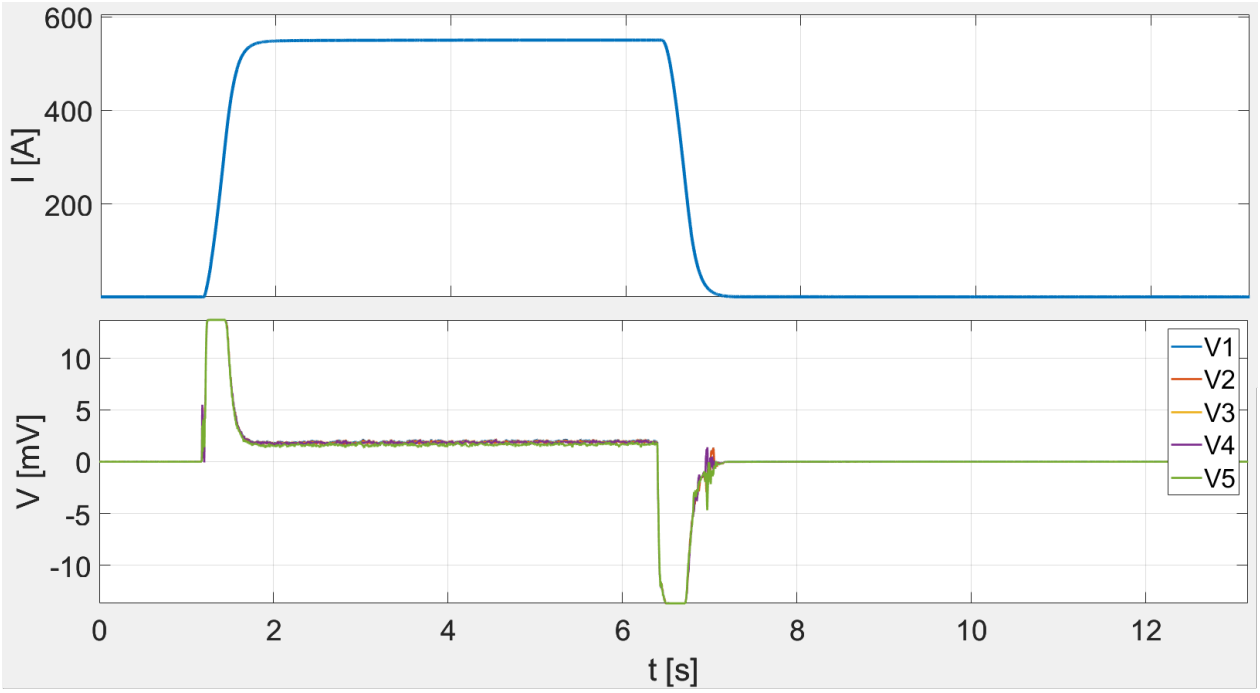

Figure 44: L-RAISER solenoid, experimental test at 550 A and 2 kA/s ramp rate (top). A stable operation for a trapezoidal input current with no premature quench was achieved. The voltage signals momentarily rises in the ramping phases (inductive component), and stabilizes during the flat-top current (resistive component).

5 Simple-stacking experiments

5.1 Short-straight HTS cable 1.3 m

This experiment was done in 2018 by Meulenbroeks et al. [113], in order to explore the stability of stacked HTS (ReBCO) tapes in direct electric contact though the copper layers under a NUCD. The experiment was performed submerged in liquid nitrogen and tested with a maximum current of around 600 A.

Recall that ReBCO tapes have an hastelloy layer serving as mechanical structural support to the tape, yet by having a high resistivity compared to copper, they also difficult the current transfer between HTS tapes, at the cost of better mechanical properties of the tape. Still, current may transfer through the copper coating that is in contact between ReBCO tapes.

The five REBCO tapes used in the cable were placed inside a copper conduit, in order to increase the available stabilizer of the cable. Then the current was fed only through the edge of the topmost ReBCO tape, to purposefully produce the worst-case scenario of NUCD. The HTS cable managed to operate stably, and current to transfer between HTS tapes under a trapezoidal input current up to 600 A. A schematic of the cable and experiment is shown in Figure 45.

Table 2: Technical specifications for short straight HTS cable (1.3 m). Being a straight sample, no inductive component is considered, operating at 77 K.

HTS tapes length	1.3 [m]
Inductance variation	No
Operating Temperature	77 [K]
Ramp Rate	up to 1000 [A/s]
Maximum current tested	600 [A]
External magnetic field	No

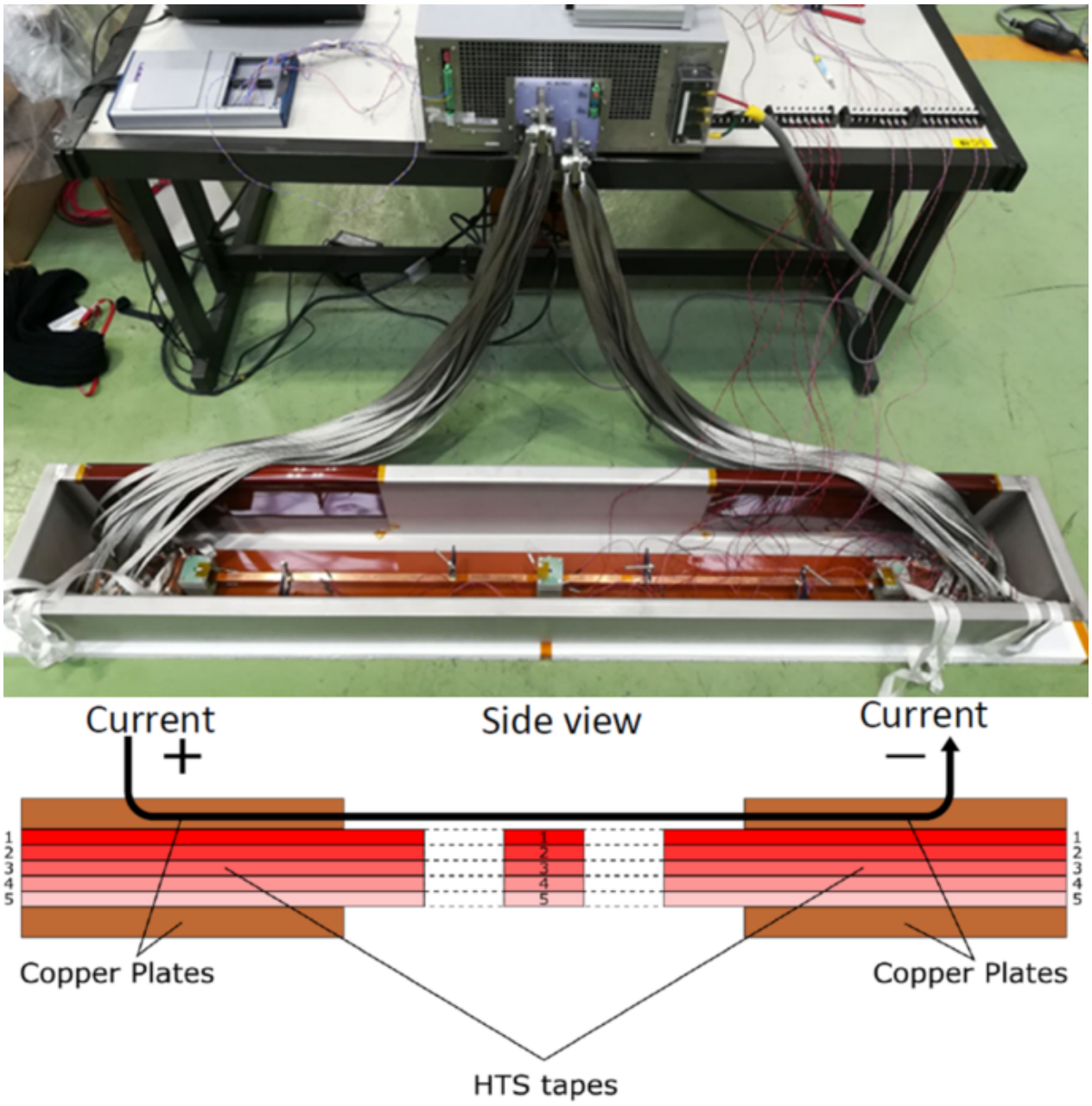

Figure 45: Short-straight HTS cable experiment, with 5 HTS tapes and worst-case scenario of NUCD, by feeding current from the edge of one HTS tape. The schematic shows a cross section where the HTS tapes and the current lead can be seen. The experiment had a copper conduit for increased thermal stability (not shown in the schematic). From [113].

The experiment included a copper conduit to serve as an additional stabilizer to the five HTS tapes, while mechanical clamps were used to press the HTS tapes to reduce the contact resistance among them.

It was confirmed that stable operation is possible even in the worst-case scenario of NUCD, as voltages did not rise significantly from the mV level up to the flat-top phase, which otherwise would indicate a quench. The cooling was provided by directly submerging in liquid nitrogen, so stability conditions were thought could be different, if e.g. using liquid helium or gas helium. Experimental data can be seen in Figure **??**:

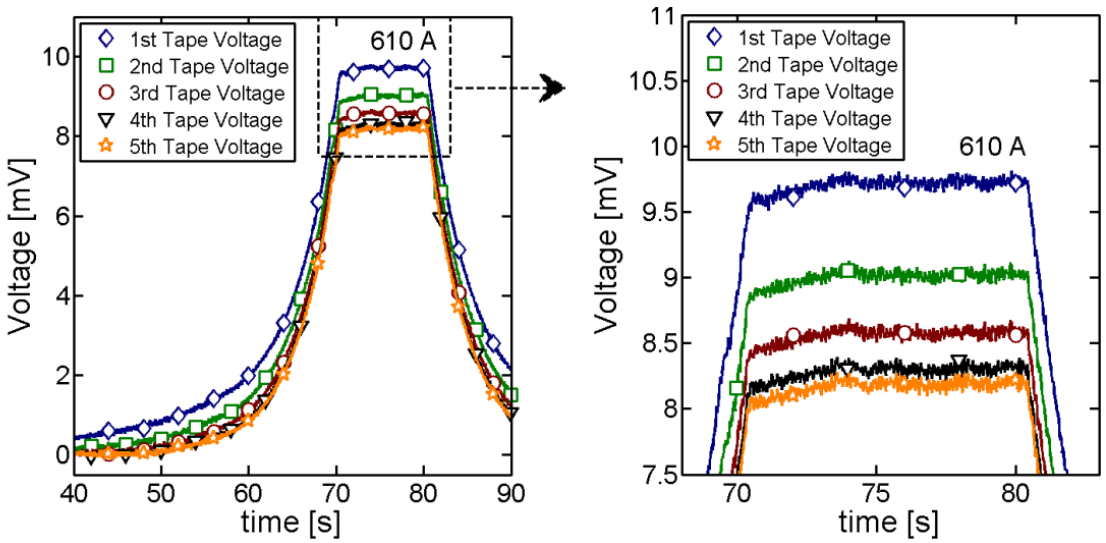

Figure 46: Voltage measurements of the Short-straight HTS cable (1.3 m) under worst-case scenario of NUCD, at a trapezoidal input current of 610 A. Despite voltage difference among REBCO, indicating different current in each, stable operation is possible even close to the total critical current [113].

5.2 20-kA-class STARS 6 m conductor sample

The 20-kA-class conductor is a 6 m coiled sample in a CICC configuration, with a stainless-steel jacket meant to withstand electromagnetic forces intrinsic of a large current magnet. Table 3 shows some of the technical specifications:

Table 3: Technical specifications for 20-kA-class STARS (6 m) coiled sample experiment. Three temperatures (20 K, 40 K, 77 K) where tested during two experimental campaigns.

HTS tapes length	6 [m]
Self-inductance	10.6 [μH]
Operating Temperature	20, 40, 77 [K]
Ramp Rate	up to 2000 [A/s]
Maximum current tested	18 [kA]
External magnetic field	Up to 8 [T]

On the first experimental campaign in March 2022, it was first observed a residual magnetic field after the input current became zero, indicating the presence of circulating currents

(sensors B_1 and B_2). Hence, in the second experimental campaign in February 2023, two additional Hall sensors were placed close to the current lead and on an intermediate position, to further explore the circulation currents decay location (Figure 47).

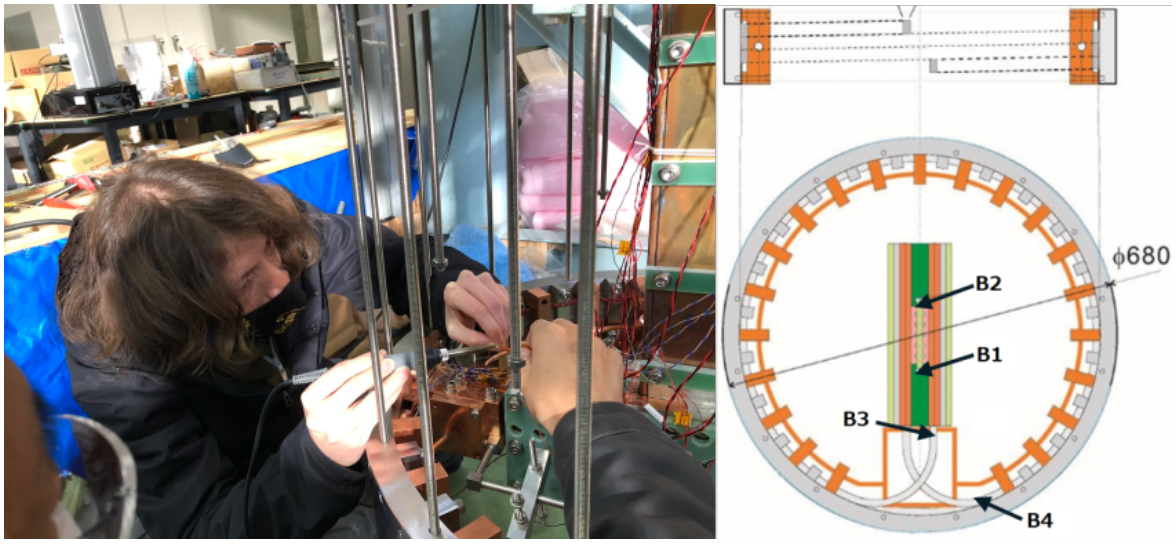

Figure 47: Soldering of sensors B3 and B4, used in the second experimental campaign for 20 kA-class-STARS experiment, to further explore the residual magnetic field detected in the first experimental campaign.

The residual magnetic field was confirmed to be higher in magnitude close to the current lead region (B_3), compared to the position farther away from it B_4. The measured residual magnetic field, for a representative trapezoidal current input with ramp rate of 1 kA/s, is shown in Figure 48:

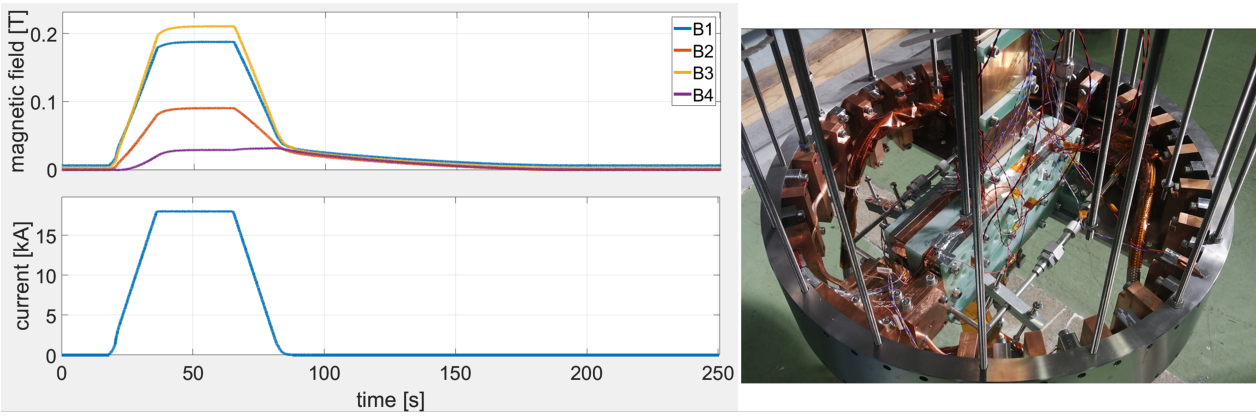

Figure 48: Residual magnetic field measured in the 20-kA-class STARS experiment, after a 1 [kA/s] ramp-down at $t > 80$ s. The circulation currents last for up to 100 seconds after the input current became zero, and decays at the same rate in all measured positions. The magnitude of the residual magnetic field is higher in the current lead (B_3) compared to the coil body farther away from there (B_4). From [85].

5.3 L-RAISER 10 m solenoid coil sample

The Inductance (L) RAISing ExpeRiment (L-RAISER) experiment was designed in order to further clarify if stable operation is possible, even with higher self-inductance of a simple-stacking HTS magnet, while inductance variation exists among HTS tapes. The resulting self-inductance is 60% higher than that of the 20-kA-class STARS experiment.

we can see in Table 4 the general technical specifications of the experiment, and the following sections describe the assembly process.

Table 4: L-RAISER (10 m) technical specifications. The HTS tapes where surrounded by two copper tapes, while being hold by a GFRP case, and submerged in liquid nitrogen for testing at 77 K.

HTS tapes length	10 [m]
HTS tapes width	4 [mm]
Self-inductance	16 [μH]
Operating Temperature	77 [K]
Ramp Rate	up to 2000 [A/s]
Maximum current tested	550 [A]
Bobbin material	GFRP

The bobbin of the L-RAISER solenoid was manufactured from GFRP, which can be used in cryogenic temperatures, and have a similar coefficient of thermal expansion than that of copper and other metals. As such, when submerged in liquid nitrogen as it was the case of this experiment, the thermal shrinking remains in the same range as of copper and other metallic mechanical structures.

The current flows into the HTS tapes through copper current leads, where it can be fed in the worst-case scenario of NUCD, such as what was done on the first experiment with a straight cable. Later, by changing the configuration of the HTS tapes, two additional cases were tested with uniform current distribution.

From here on, it follows a more detailed explanation of the preparation and manufacturing of the experiment, which hopefully may serve of guideline into the development of similar kind of experiments, based on HTS tapes.

5.3.1 Assembly

- **Preparation and dummy tape**

  The whole cable of L-RAISER is composed of 5 HTS tapes, surrounded by two copper tapes as the innermost and outermost tapes. The copper tapes work as stabilizer, to help conduct the current in case of a quench, while also serving as a cushion to protect the HTS tapes from mechanical damage from the pressure plates.

  As practice before start winding the solenoid with HTS tapes, a winding test is made with steel tape, to have a feeling of the process, and be able later to better handle the

HTS tapes without damaging them in the winding process.

Figure 49 shows the trial winding process with the steel dummy tape. Afterwards, a copper tape was wound in the bobbin to serve as the first cushion layer before the winding of the HTS tapes.

Figure 49: L-RAISER Assembly 1. Left: Dummy steel tape used for preliminary winding practice. Right: Copper tape, first tape in the stack, used as cushion and stabilizer to protect the HTS tapes from mechanical damage by the pressure plates.

- **HTS tapes winding**

  Once the first copper tape is wound, the winding of the HTS tapes begins, the cable consists of 5 HTS tapes of 10 m length, hence 50 m in total, plus around 0.3 m in each end, to make the connection with the current leads. A HTS tape roll contained enough length for the total of 53 m, hence to form the simple-stacking cable configuration, the winding process was repeated five times for each HTS tape.

  To transfer the HTS tape to the bobbin, the HTS tape roll and the bobbin were placed in two independent rotating stands. Once mounted, by rotating both stands at the same time, the HTS tape is transferred to the bobbin, as shown in Figure 50. Pressure plates are gradually mounted and dismounted, in order to keep the HTS tape in place while the next HTS tape layer was wound.

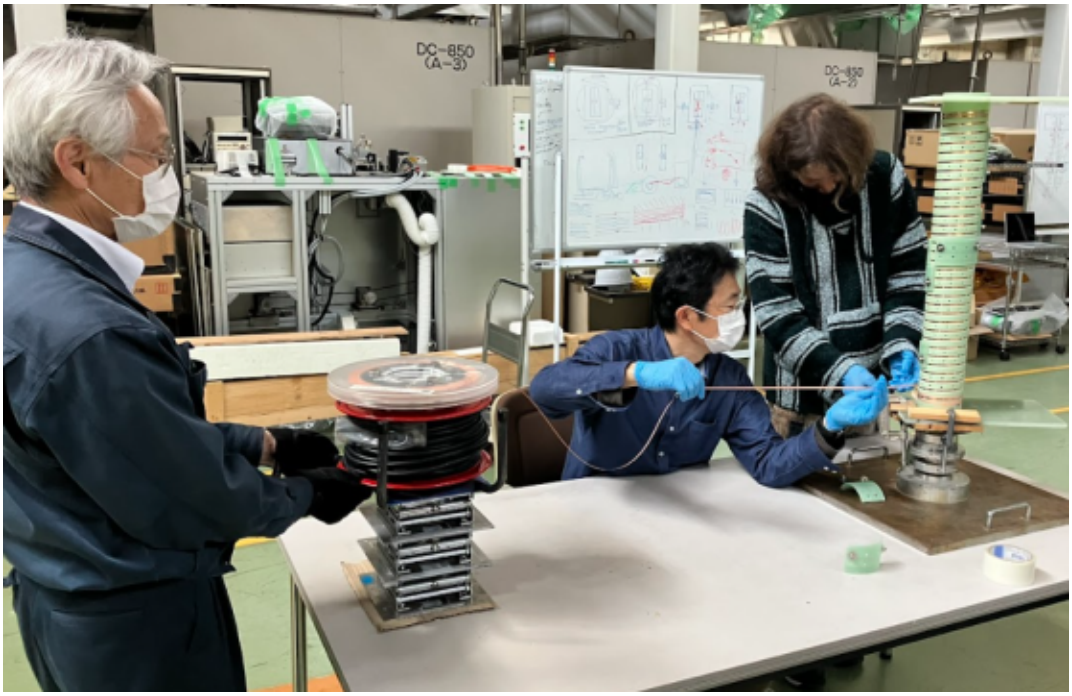

Figure 50: L-RAISER Assembly 2. L-RAISER bobbin and HTS tape roll mounted on two separate rotating structures, so the HTS tape can be wound into the bobbin, securing the HTS tapes with spaced pressure plates.

Figure 51: L-RAISER Assembly 3. Left: Starting the winding of one HTS tape, wound from top to bottom. Right: After finishing the winding of each HTS tape, they are temporarily secured with Kapton tape, before attaching them to the current leads.

When one 10.6 m HTS tape was finished to be wound, the endpoints were temporarily secured with Kapton tape, to allow the connection with the current leads later.

Figure 52: L-RAISER Assembly 4. Outer copper cushion tape wound after the 5 HTS tapes, for mechanical damage protection from pressure plates to HTS tapes. As the copper tapes where 5 m long, unlike the 10+ m from the HTS tapes, two copper tapes per layer were used.

After finishing the 5 HTS tapes winding, another copper tape was wound on top of the stack, as the outermost tape, again, as stabilizer cushion to reduce possible damage to the HTS tapes, shown in Figure 53.

Figure 53: L-RAISER Assembly 5. Left: 5 HTS tapes plus 2 copper tapes wound and secured by pressure plates. Center: Preparation of bolts to collocate all the pressure plates in the bobbin. Right: Finalizing process for all bolts to secure and press the HTS tapes, to reduce contact resistance and have good current transfer among them.

When the stack of 5 HTS tapes plus two copper tapes were finished, the pressure plates all around the bobbin were placed, to reduce the contact resistance between HTS tapes that could facilitate current transfer between them. As they surround and press the HTS tapes along their length, it would be expected that the contact resistance would be roughly the same along the length as well.

- **Voltage taps**

  Once the tape stack is finalized and the pressure plates put in place, the attachment of the sensors began, starting with voltage measurement across each HTS tape. The endpoints of the HTS tapes were loosened and voltage taps were soldered in the superconducting layer side of the REBCO tapes (with a prior cleaning with liquid flux to remove the local oxide layer in the HTS tapes), to measure as close as possible the voltage appearing across the length in the superconducting layer itself, shown in the left side of Figure 54.

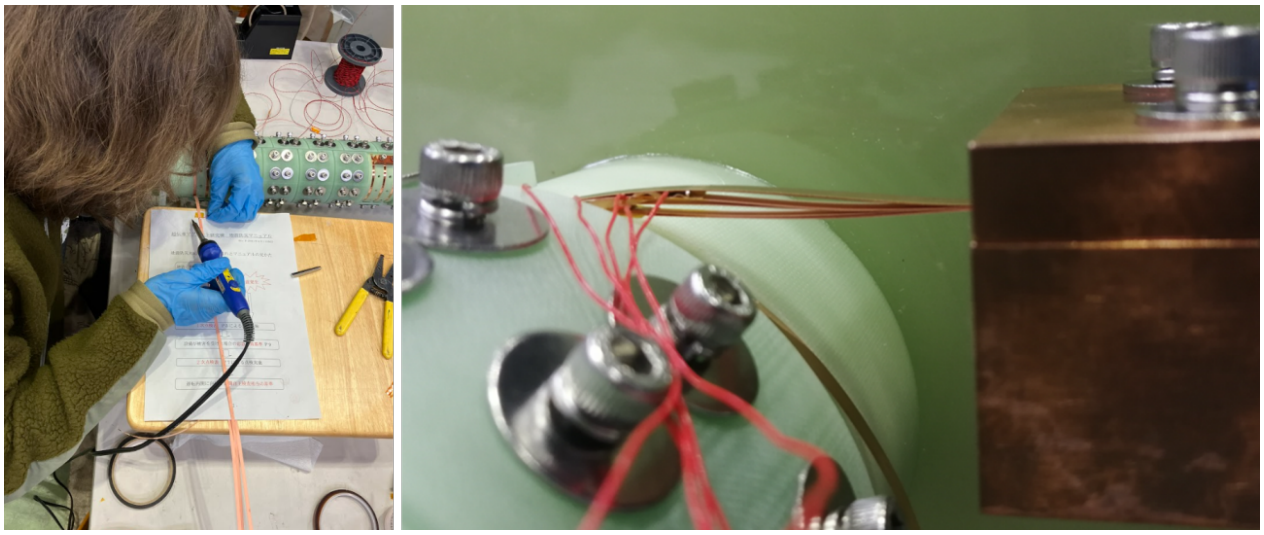

Figure 54: L-RAISER Assembly 6. Left: Soldering of voltage taps in the superconducting layer side of each REBCO tape. Right: Voltage taps attached close to the copper current lead.

  Once the five voltage taps had been soldered, the tape stack was placed into the copper current lead, closed down and bolted, to complete the electrical connection. Three cases of current feeding were tested, which will be explained afterwards. For the first case, the closed current lead with the soldered voltage taps can be seen in the right side of Figure 54.

- **Magnetic (Hall) Sensors**

  Similarly as what was observed on the 20-kA-class STARS, magnetic (Hall) sensors were installed on L-RAISER to observe the decay of the circulating currents via the decaying residual magnetic field. Six Hall sensors were prepared and installed in pairs, at three different positions in the bobbin, two on the center, and two pairs on each current lead next to the connection between the tapes and the current lead (Figure 55).

  Each Hall sensor had the four required cables soldered, and they were all powered in series to the same power source, to ensure the same current in each of them, and the same rate of increase or decrease in the magnetic field. Additionally, they were covered in Kapton tape to facilitate removal later on, so they could be reused in this or other experiments.

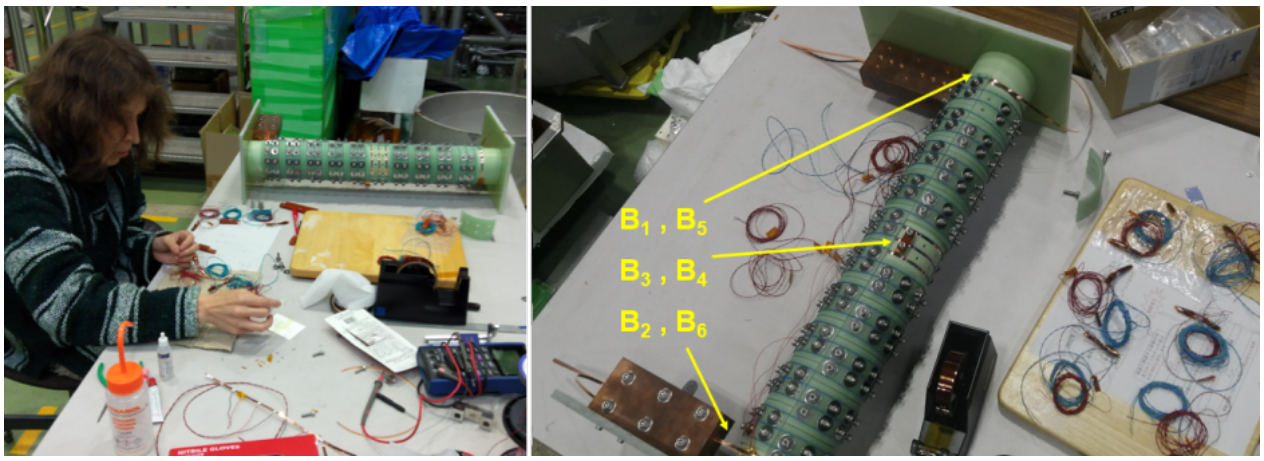

Figure 55: L-RAISER Assembly 7. Left: Soldering of the Hall sensors cables for power and signal acquisition. Right: Six Hall sensors prior to their installation, two of them in each of the current leads, and two in the central region of the solenoid. Orange lines indicate their positions.

Figure 56 shows the Hall sensors attached in one of the current leads (left side), and on the center of the bobbin (right side).

On the bobbin center, two Hall sensors (labeled B_3 and B_4) were placed as a redundancy, as the magnetic field may behave similarly. Due to space limitations, they were placed directly on top of the tape stack and as close as possible, so the magnetic field could be more easily measured.

In case the magnetic shielding produced in the HTS tapes could reduce the measured magnetic field parallel to the HTS tape, and thanks to the available space, two measuring positions both perpendicular (B_1 and B_2) and parallel (B_5 and B_6) to the magnetic field lines direction were placed.

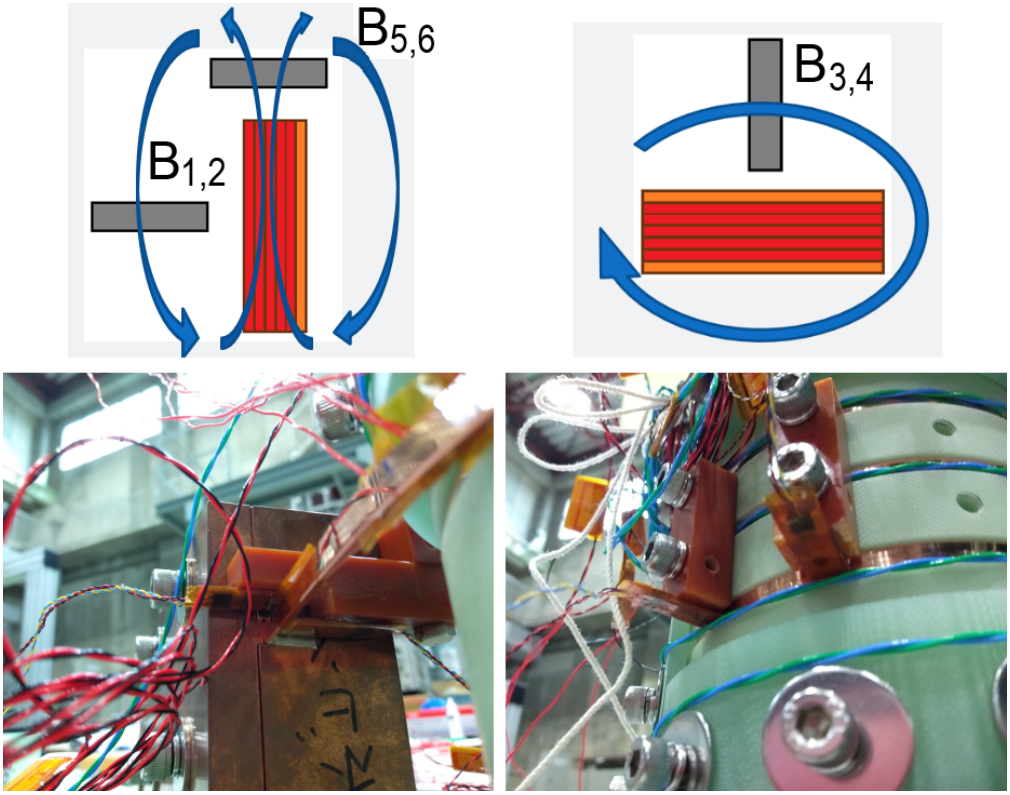

Figure 56: L-RAISER Assembly 8. Hall sensors installed on the solenoid, blue lines indicate the magnetic field created by the HTS tapes. Left: Hall sensors (B1, B2, B5, B6) in the current lead attached near the current feeding point, where circulation currents were expected to return among HTS tapes. Right: Hall sensors (B3, B4) installed in the center of the solenoid, on top of the HTS tapes.

> The Hall sensors were meant to detect the residual magnetic field evolution and its total decay time. As such, the measured magnetic field magnitude was less relevant, and rather it was roughly estimated based on an analytical calculation, to confirm that a measurable signal was going to be obtained under their chosen location.

Finally, the L-RAISER solenoid was placed on a steel container surrounded by styrofoam, to have a good thermal insulation from the environment. The current source cables were connected to the current leads, the cables for recording voltage tap and magnetic hall sensor signals were connected to the data acquisition system. Then, once the setup was completed, liquid nitrogen could be poured into the vessel to start the experiment, covered with a styrofoam lid to reduce liquid nitrogen evaporation rate. The final setup is shown in Figure 57:

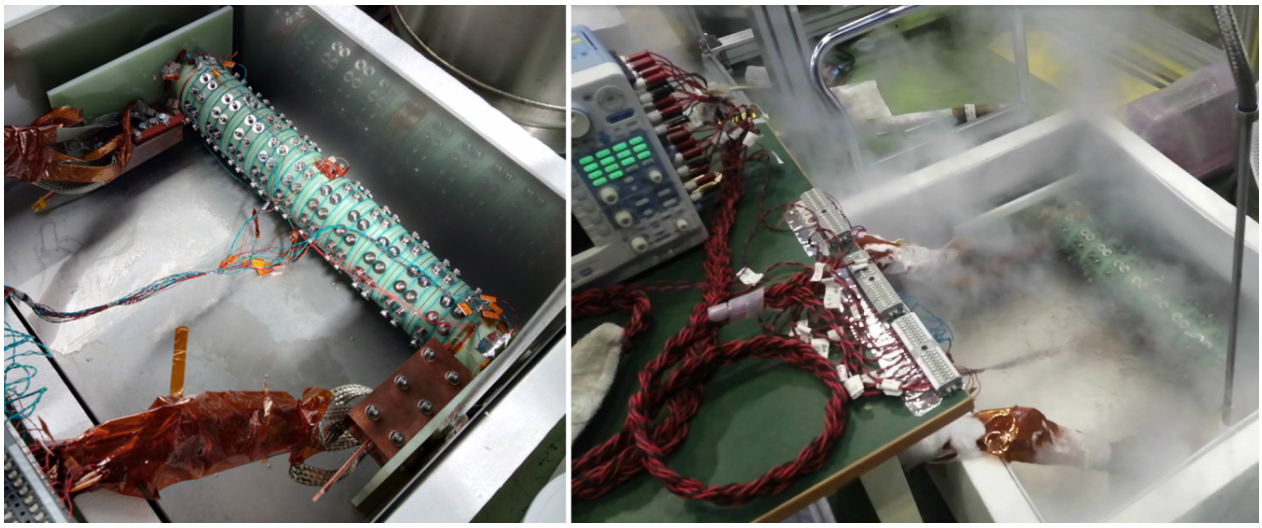

Figure 57: L-RAISER Assembly 9. Left: Solenoid placed on steel container surrounded with styrofoam, to decrease the evaporation rate of liquid nitrogen. Right: Container filled with liquid nitrogen, to cool down and begin experiments.

Figure 58: L-RAISER Assembly 10. Styrofoam lid placed, diagnostics system set, and power supply with controllable current plugged, to begin experiment and data acquisition.

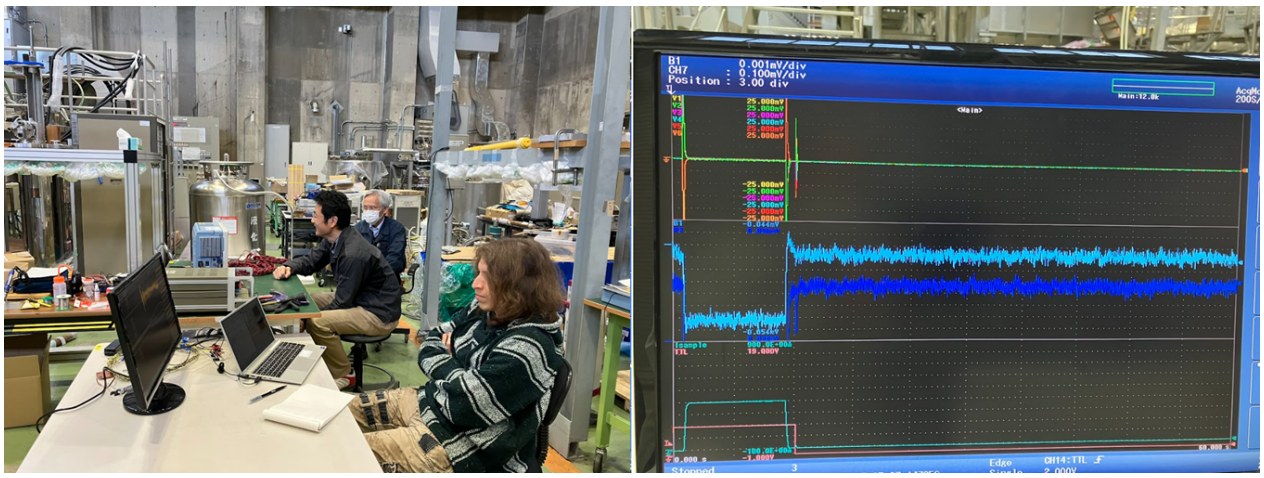

Figure 59: L-RAISER Assembly 11. Data acquisition under different trapezoidal current waveforms, varying ramp rate and flat-top maximum current. Right: Representative shot data collected, at 400 A current and 1000 A/s ramp rate.

5.3.2 Experimental results

Once both the voltage taps and Hall sensors were attached, the planned three cases were performed, as it is described next. The current was fed via six bolts attached to the current lead, while the configuration of the HTS tapes could be modified to test different current input scenarios.

Three current feeding cases were outlined, which gradually increased the uniformity of the current that was fed into the HTS tapes, while decreasing the joint resistance between them, which could enhance the circulation currents magnitude and decay time. For each of these three cases the current lead was opened, the connection between HTS tapes modified, and then closed again, to test the next defined case. Figure 60 shows each of these three cases which were respectively:

- **Non-uniform current feeding**
  Initially the tape stack was connected while the current was fed through the topmost HTS tape, to replicate the condition of worst-case scenario of NUCD tested on the short-straight HTS cable experiment.

- **Staircase Indium foil connection**
  The HTS tapes are cut in a staircase shape, while the voids are filled with indium (In) foil, that facilitates a uniform current distribution.

- **BSCCO tape joint**
  The REBCO tapes are cut in the current lead section, and a BSCCO tape extension is soldered to each one, further reducing the joint resistance.

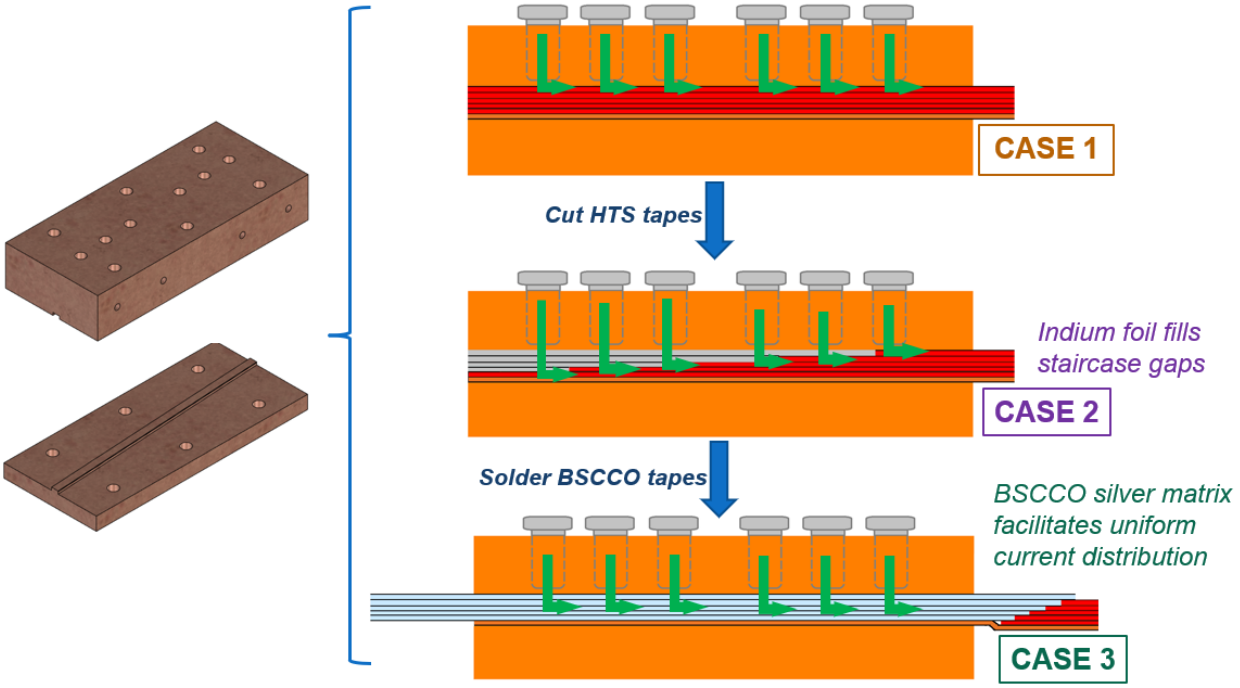

Figure 60: Three cases tested for current feeding in the HTS tapes. Case 1 is a worst case scenario of NUCD, with current fed in the top-most REBCO tape. Case 2 is for uniform current feeding, by cutting in a staircase shape the REBCO tapes in filling the gaps with indium foil. Case 3 cuts the REBCO tapes from the current lead, to solder BSCCO tapes along extensions on the left, being a uniform current also facilitated by the silver matrix of the BSCCO tapes.

- **Case 1: Worst-case NUCD**
  The HTS tapes are directly placed along the current lead canal, while removing the outermost wound copper tape from the current lead region, to directly feed the current to the outermost HTS tape.

  The copper current lead connections were treated with liquid flux, to remove the oxide layer in the current lead, as well as the whole connecting region in each HTS tape, finally cleaning with isopropyl alcohol to remove flux remnants and stop continuous chemical interaction within the copper region. Once the surfaces were clean, the current lead was closed, bolts tightened, and the current source cables connected. The final connection is shown on the right side of Figure 61:

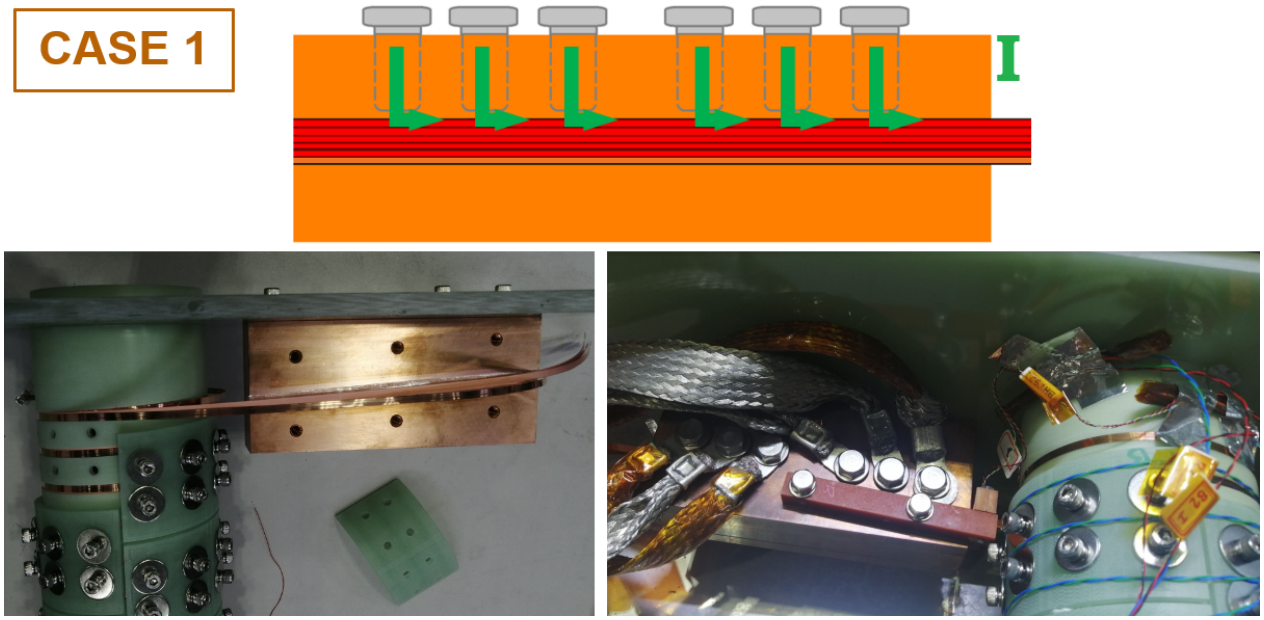

Figure 61: L-RAISER Case 1: NUCD current feeding. Left: The current lead previous to being closed, with the current being fed from the opposite side from the camera point of view. Right: Current lead closed, and power supply wires in place, where the current flows from bolts to copper current lead and then to the REBCO tapes.

Then after submerging the sample in liquid nitrogen (LN_2) the experiment began. The solenoid was tested at 100 A and a slow ramp rate, to confirm the superconducting state of the HTS tapes.

Then the solenoid was tested at higher current, reaching a maximum current of 180 A and 1 kA/s stably, condition at which a slight voltage rise was detected in V_1, which corresponds to the innermost HTS tape. This is shown in Figure 62:

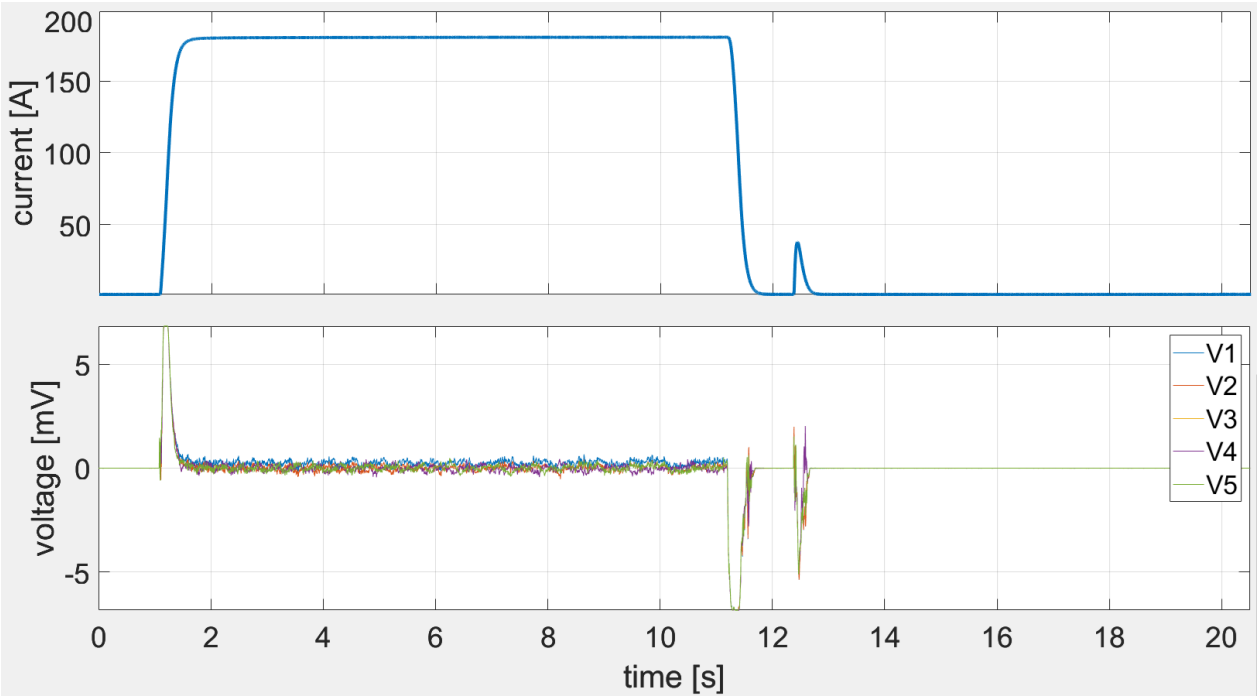

Figure 62: L-RAISER Case 1, 1. Slight rise in voltage V1 (innermost HTS tape), for 180 A and 1000 A/s. As the total current surpasses the critical current of one HTS tape (around 120 A at 77 K), current is being transferred to other HTS tapes despite the voltage rise.

From this point, the current was slightly increased up to a trapezoidal input current of 200 A at slow ramp rate, to carefully observe if the voltage rise in V_1. The flat-top value of 200 A was reached, with a noticeable increase of the V_1 voltage, shown in Figure 63:

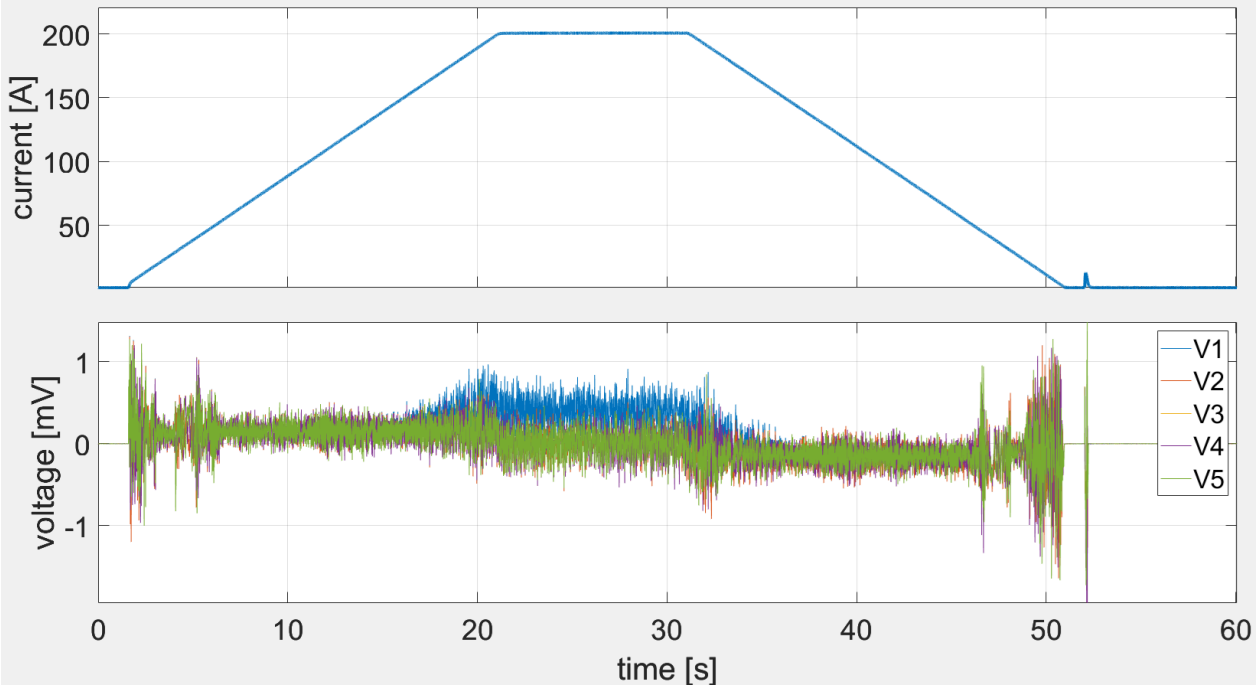

Figure 63: L-RAISER Case 1, 2. The total current is increased slowly (10 A/s) up to 200 A. Near reach and during the flat-top phase, a voltage rise is detected in V1 (innermost HTS tape), which indicates a high-current share in that HTS tape, yet operating stably.

At this point, since the maximum current was already higher than the critical current of a single HTS tape, it indicates that current was being transfered to other tapes, and higher current values might be achievable.

However despite the apparent stability and current transfer between HTS tapes, as what was observed in the short-straight HTS cable, in order to reduce the risk of damaging the HTS tapes under a worst-case NUCD, the experiment was stopped to continue with the next case.

- **Case 2: Staircase joint with Indium foil**
  The main aim of the L-RAISER experiment was to test the stability of a coiled cable under a fast ramp rate. For this, a uniform current feeding facilitates stability, as current can distribute more equally between the HTS tapes, even if current redistribution starts occurring due to the inductance variation between HTS tapes.

  As such, the current lead was opened and the HTS tapes were cut in a staircase shape, then indium foil was cut to fill the remaining gaps in the staircase shape, as shown in Figure 64. The copper sections that make the electrical connection were treated again with liquid flux and cleaned with isopropyl alcohol. Then the current lead was closed and bolted again to finalize the electric connection.

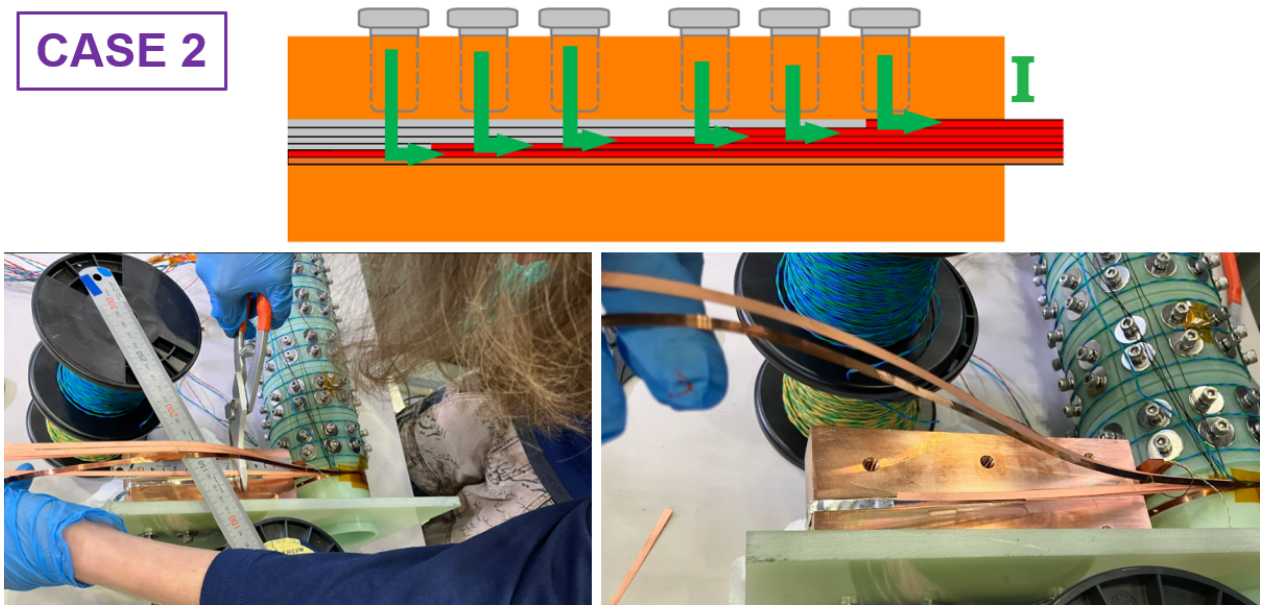

Figure 64: L-RAISER Case 2. The configuration was changed from NUCD to uniform current distribution. The REBCO tapes were cut in a staircase shape, and the step gaps filled with indium foil. The lower resistance via the indium foil facilitates a more uniform current distribution, by eliminating intermediate REBCO tapes that have the more-resistive hastelloy substrate embedded.

Under the improved joint condition, the current feeding was uniform, and a current up to 500 A could be reached without a measurable voltage increase across the HTS tapes. Fast ramp rates were tested to see if a quench could occur in the sample, reaching up to 2 kA/s ramp rate with no apparent indication of instability or quench, besides the inductive voltage formed during the ramping phases.

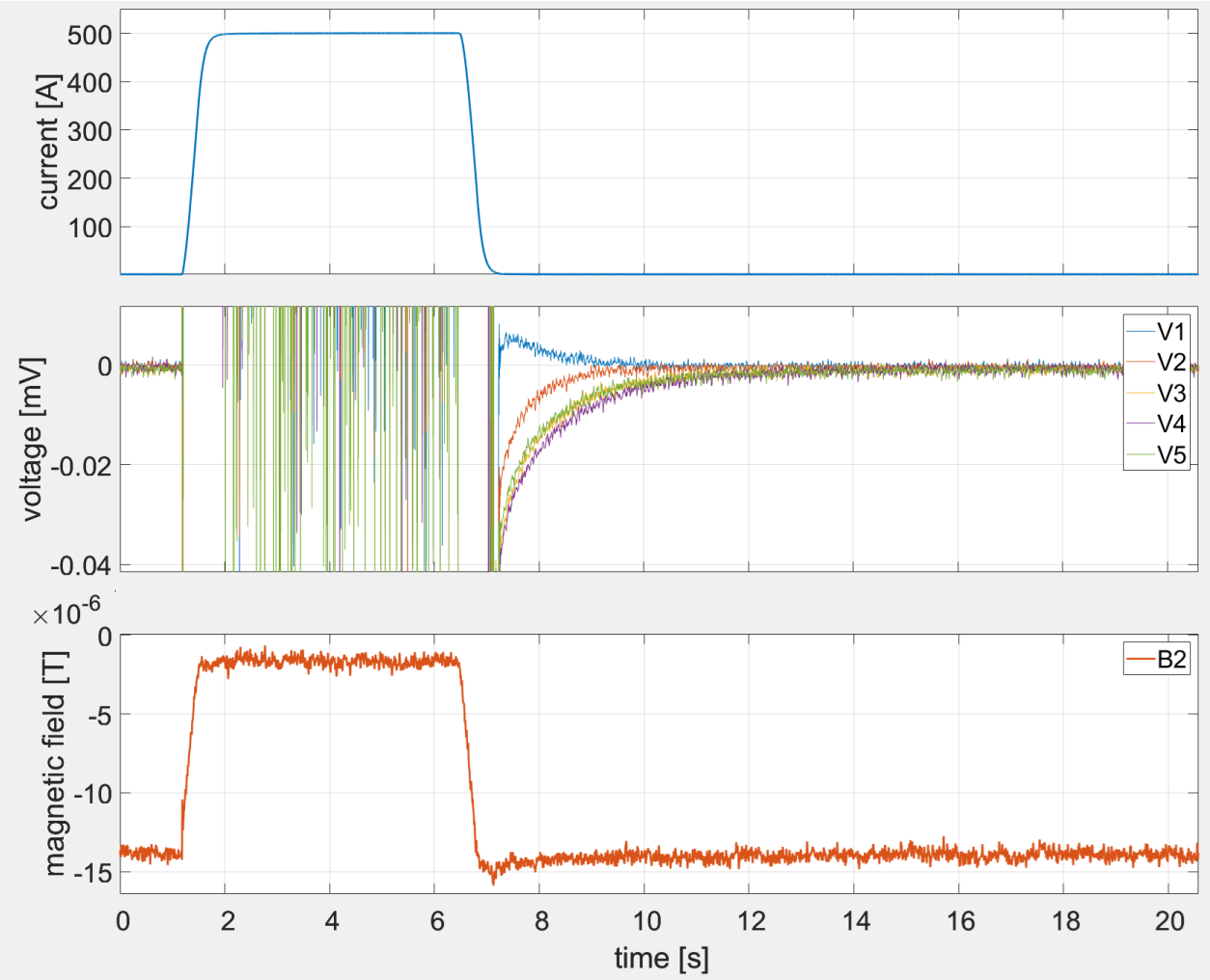

Figure 65: L-RAISER Case 2, 1. Trapezoidal input current up to 500 A and 2000 A/s. The voltages in all HTS tapes remain on the same low-value range during the flat-top phase (not visible in the plot). The voltage signals are zoomed in, and a decay in the signals can be detected for 3 s after the input current became zero, indicating circulation currents (note the innermost tape V1 has the opposite sign compared with the other voltages). The same decay can be in the magnetic field data for sensor B2.

This time, the reduced joint resistance also allowed to observe a residual magnetic field, as formerly observed in the 20-kA-class STARS experiment, with a decay up to 3 s. Furthermore, by zooming in the voltage tap signals after the input current had become zero, a decay in each voltage tap was visible, indication of the circulation currents decaying on the sample.

- **Case 3: BSCCO tape soldered to REBCO**

  For the next step, the goal was to find a way in which the joint resistance between HTS tapes could be further reduced, while having a uniform current feeding. Then it was decided to use BSCCO tape extensions for each REBCO tape.

  The REBCO tapes were cut as close as possible to the edge of the current lead, and a BSCCO tape soldered in each REBCO tape with a solder area as long as possible. The BSCCO tapes, having a silver matrix connecting the superconducting filaments, also facilitate a uniform current distribution to flow through the REBCO tapes. Clamps were placed to increase the mechanical pressure additional to the bolts that make the electrical connection, that may help reduce the joint resistance between the BSCCO tapes.

  The BSCCO tapes cover the whole length of the current lead and furthermore, an extra length was extended on the opposite side, and all the BSCCO tapes soldered in that side. This allows reducing the joint resistance by increasing the total joint area where circulating currents can flow back among the REBCO tapes. Figure 66 shows the BSCCO tape extensions schematic, and how they were attached into the current lead.

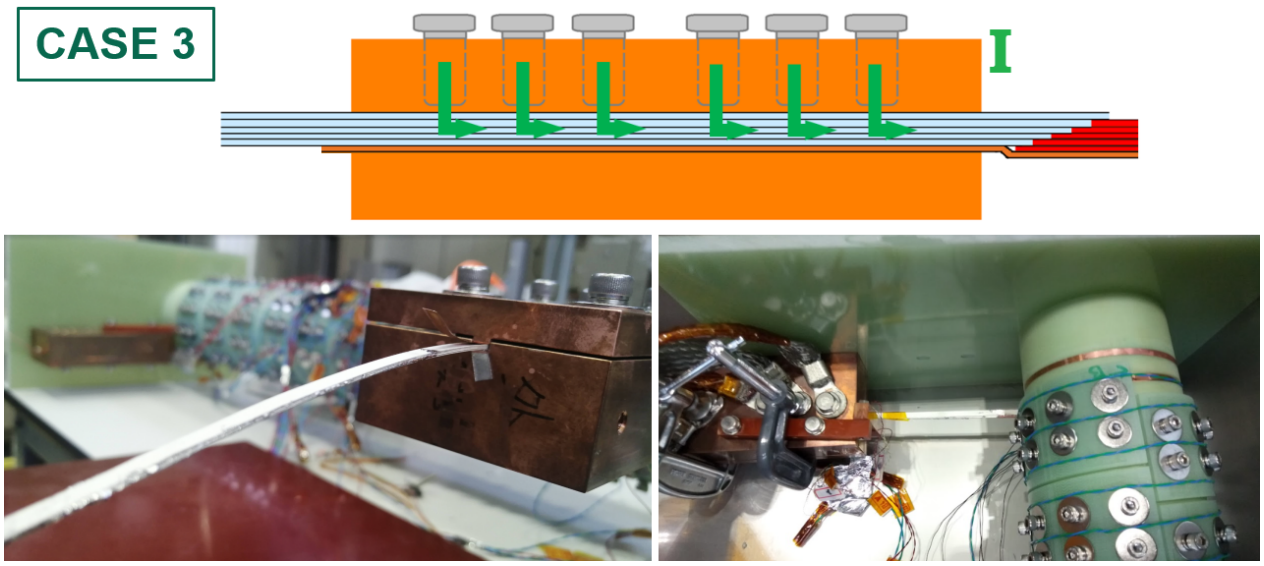

Figure 66: L-RAISER Case 3. All the REBCO tapes are cut, soldering one BSCCO tape for each REBCO tape, with a solder area as wide as possible based on the space between the bobbin and the current lead (around 40 mm length). An extension of about 14 cm is left on the opposite side of the current lead, and all the BSCCO tapes soldered. The combination of large solder area and high mechanical pressure in the current lead, contributes for an overall lower contact resistance. The BSCCO tapes, having a silver matrix where superconducting filaments are embedded, facilitate uniform current distribution.

Under the BSCCO tape configuration, the attained current was also available for 500 A, while the residual magnetic field by the circulation current lasted for up to 10 s, as it can be seen in Figure 67.

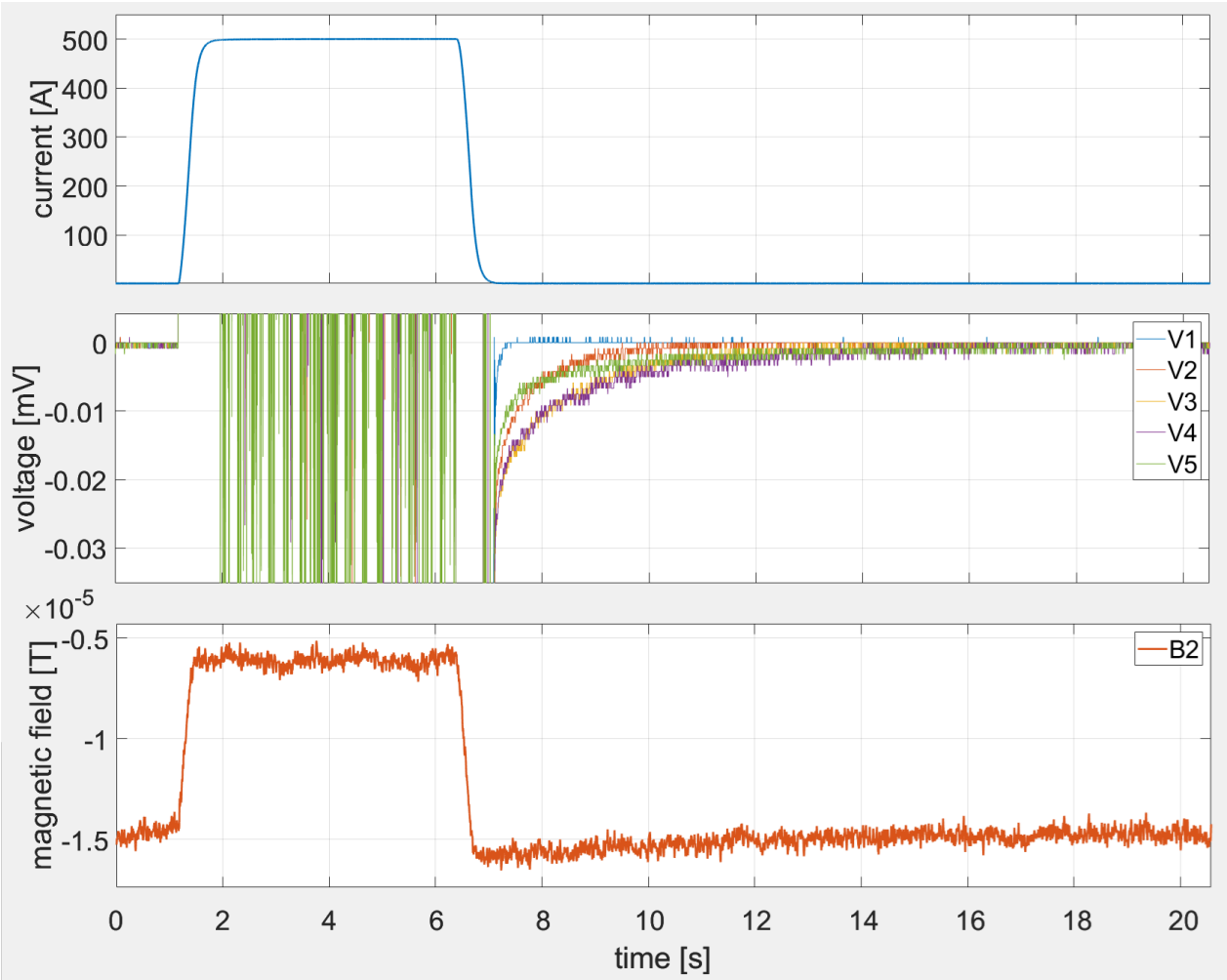

Figure 67: L-RAISER Case 3, 1. Voltage remains the same in all HTS tapes during the flat-top phase, indicating uniform current distribution, as of the previous case, also at 500 A and 2000 A/s. A decay in the voltage taps and magnetic field signals is detected, for up to 10 s after the input current had become zero.

The experiment was pushed further to determine what may be the critical current of the L-RAISER solenoid, and a slow ramp rate of 10 s was applied to find out. The critical current was determined around 550 A, where a gradual increase of the voltage was observed in all tapes, heading towards a quench. The current source was shut down to avoid damaging the HTS tapes, and similarly the decaying magnetic field was present for around 10 s.

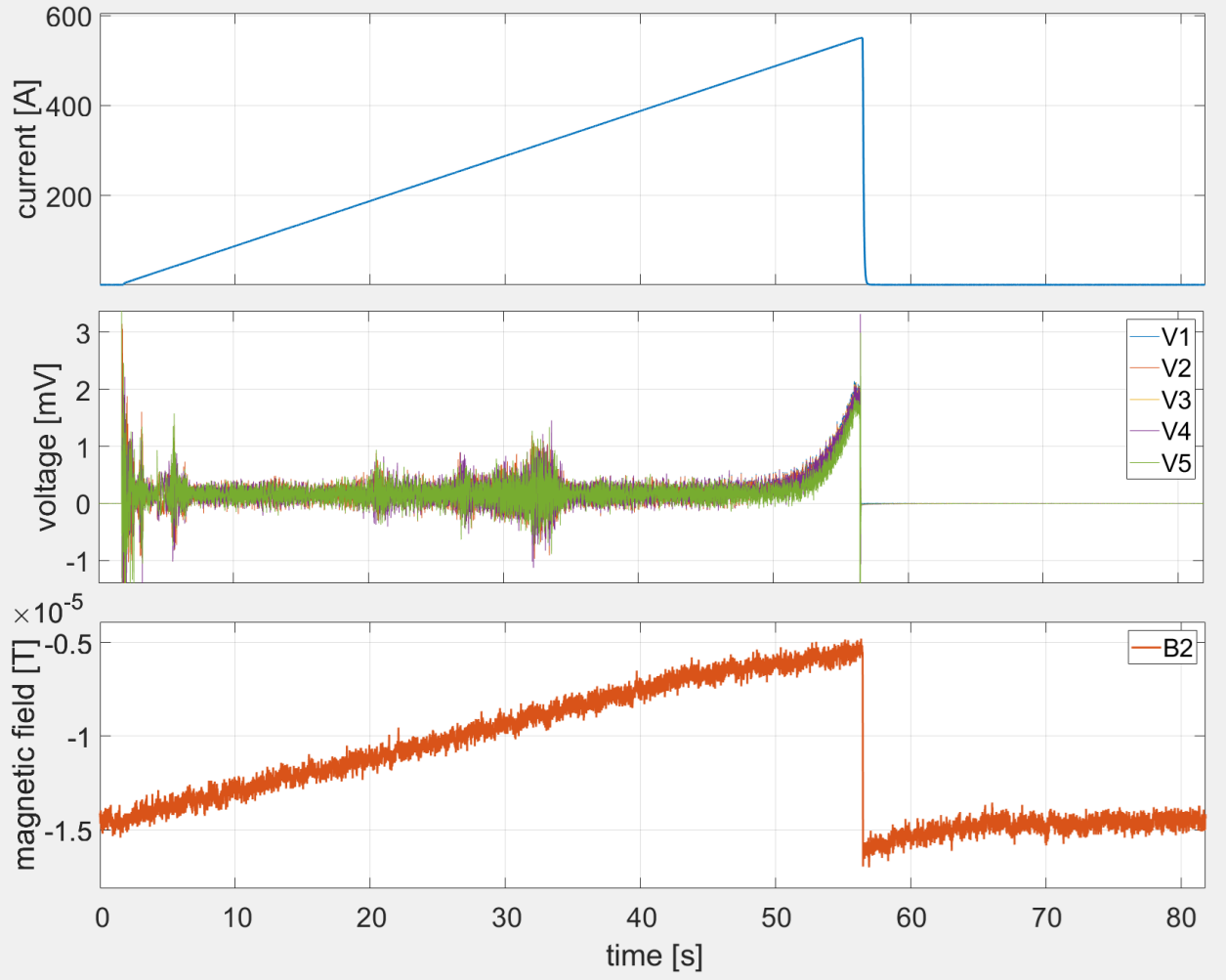

Figure 68: L-RAISER Case 3, 2. To find the critical current of this cable configuration, a trapezoidal input current of 550 A, 10 A/s is applied. After around 510 A, a steady voltage rise in all HTS tapes is detected, indicating a quench is on development, so input current is shutdown. After the shutdown, a decay in the magnetic field signal is detected for up to 10 s, caused by circulation currents. A small decay can be slightly seen in the voltage taps zoomed out plot.

Once establishing that the critical current was around 550 A, faster ramp rates were tested, where it was observed that HTS tapes could withstand a fast charging up to 2 kA/s without quenching, as shown in Figure 69. Perhaps the lower ramping time produced less AC losses that were leading to a quench in the slow ramping-up case. Given the joule heating is the the total heat energy produced in a time window, a fast ramp rate may produce less heating, compared to a slow ramp rate where joule heating is produced during a longer time.

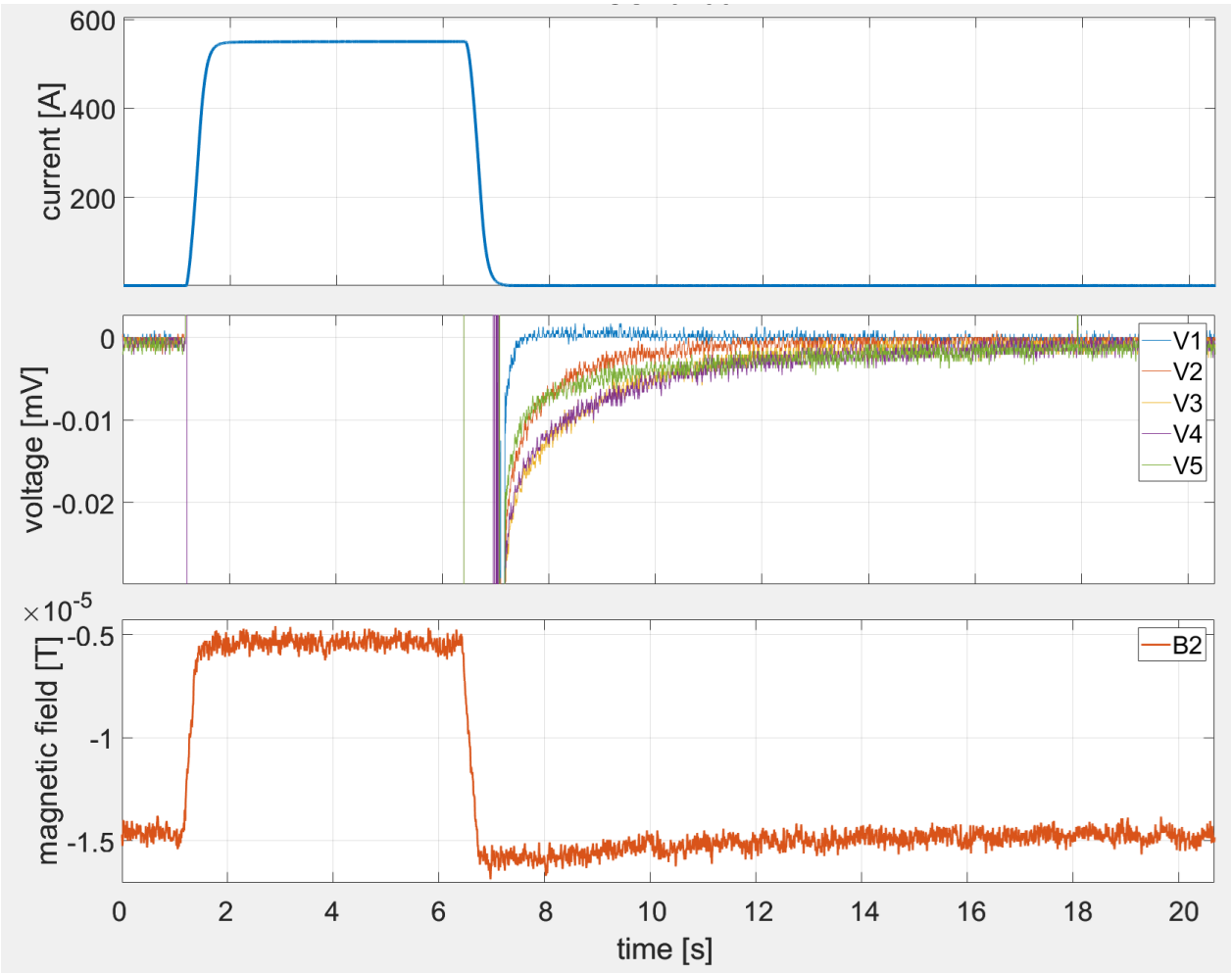

Figure 69: L-RAISER Case 3, 3. A trapezoidal input current with 550 A and 2000 A/s is applied. In this case, stable operation is achieved during the flat-top, likely due to the lower joule heating generated in a fast ramp rate compared to a slow ramp rate ($Q = RI^2\Delta t$). The decay, both in voltage taps and magnetic field B_2, last up to 10 s in this configuration with lower contact resistance overall (zoomed-in signals).

All the figures for the magnetic measurements so far, show only the measured value at B_2, which was located in the current lead region, and which showed the clearest magnetic field decay for more of the shots.

Sensors B_5 and B_6 failed, so it was not possible to obtain data for their positions. On the other hand, sensors from B_1 to B_4 showed all the decaying magnetic field at a similar rate. The residual magnetic field magnitude was slightly higher on the current lead locations, compared to the central region, similar to what was observed in the 20-kA-class STARS experiment.

It is expected that faster ramp rates may have been possible according to the experimental results observed, however the current source controller only allowed a ramp rate up to 2 kA/s.

Figure 70 shows the highest current and ramp rate attained for the experiment, 550 A and 2 kA/s. The voltage taps show a similar signal for all tapes, with the peak inductive voltages that are produced during the ramping phases. The magnetic sensors data shows how the residual magnetic field decays at the same rate in all positions.

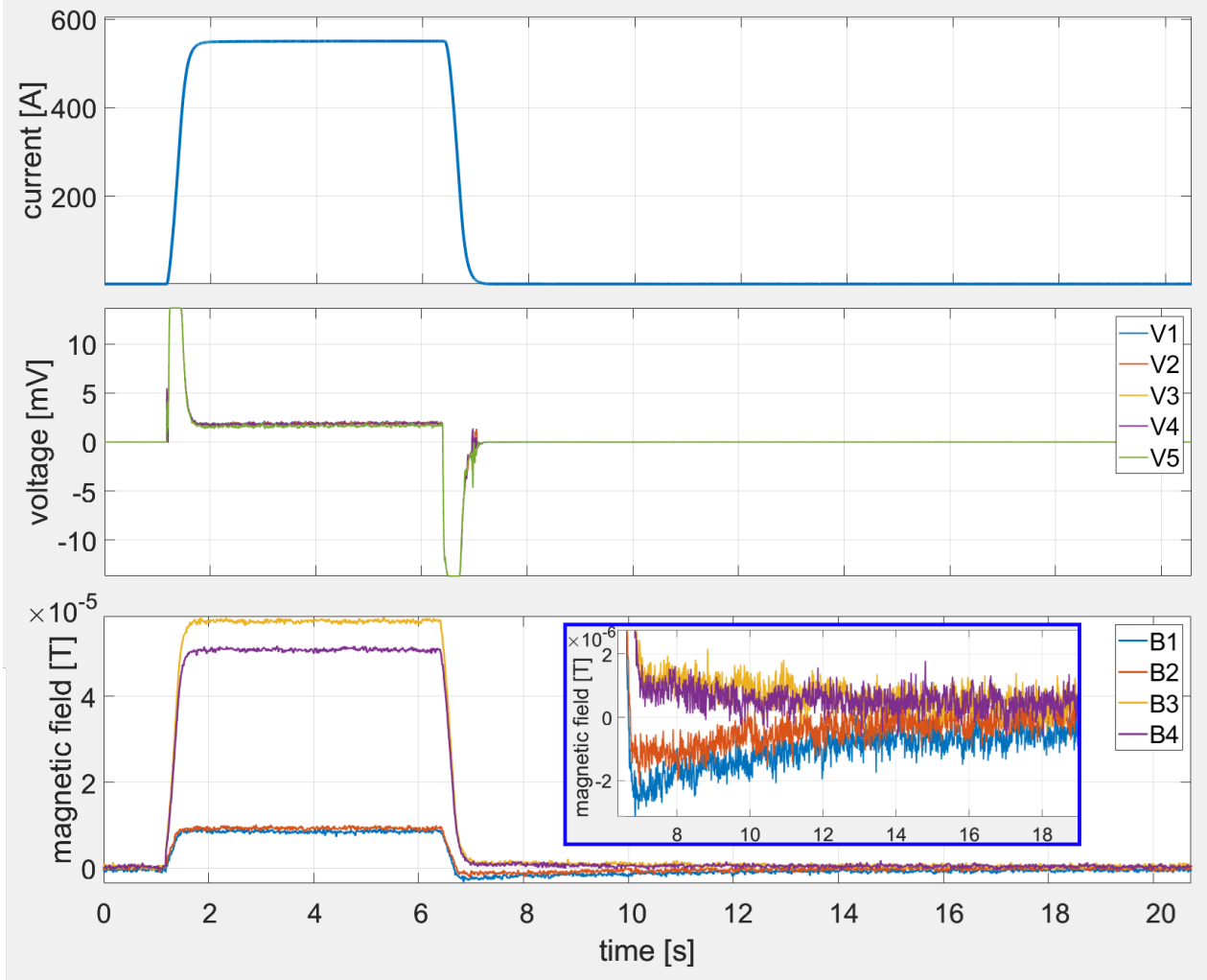

Figure 70: L-RAISER Case 3, 4. Same trapezoidal input current for 550 A and 2000 A/s. The signals in all the magnetic sensors is included, where a decay within 10 s can be seen, on a similar rate for all. During the ramping phases, there is an inductive voltage rise, and during the flat-top, the cable operates stably at a fixed voltage value for all the HTS tapes.

6 Numerical calculation for current distribution in HTS

6.1 Formulation and general assumptions

A numerical simulation was developed, in order to predict the operation of a simple-stacking HTS cables, accounting the superconducting properties of REBCO. Afterwards, comparison between experiment and simulation is done.

Better understanding how current gets distributed, under both a constant and changing input current, is convenient to clarify the reason of the stable operation that has been observed so far in HTS conductors, unlike what was observed in the past with LTS conductors.

General conditions for the numerical calculations are:

- ***Temperature***
  Considered constant for the model, presently for ranges from 20 K to 77 K. Given the operation conditions below the critical current, the joule heating generated is assumed low enough to be exhausted by a cooling system, plus the high cryogenic stability of HTS and increased heat capacity of materials at temperatures above 20 K (compared to lower heat capacity of LTS at 4 K).

- ***Critical Current and Magnetic Field***
  Three scenarios are considered at a constant temperature. The critical current case is specified later for each numerical calculation.

  - *Constant critical current*
    Considered as a constant value, 20% higher of the value obtained at the operation current of a given cable
  - *Critical current dependent on total current* ($I_c = f(I_{total})$)
    The critical current decreases linearly as a function of the input current, to account for the effect of the self magnetic field.
  - *Critical surface*
    A surface fit for the critical current $I_c(T, B)$ was made, based on publicly available experimental data from Robinson Research Institute of Victoria Wellington University, for Fujikura FESC 2G HTS tapes [138, 139], to extrapolate to high-current and high magnetic field scenarios. BSMag code [140] was used to compute the magnetic field distribution, and compared with the publicly available CryoSoft Solids suite for YBCO [141].

The models presented here aim to make a description of how current may get distributed among HTS tapes in a conductor, considering the superconducting behavior, plus the share of currents between strands due to electric (resistance) and magnetic (mutual inductance) interaction.

Other aspects of a large magnet operation are simplified as much as possible, yet they may need to be taken into account for a comprehensive modelling of all phenomena involved. To name a few of these effects, they include electromagnetic forces, hysteresis and coupling AC losses, cooling thermal analysis, and nuclear heating in the case of fusion magnets [142, 143].

6.2 Constant Temperature RL circuit

For the simple-straight cable experiment, the first scenario is where mostly the resistance (R) is involved in the redistribution of current among the HTS tapes, inductance (L) effects are negligible. When going from a straight to a coil configuration, the inductance needs to be taken into account.

Once the operating temperature is defined, the copper resistance is defined by the geometry of the conductor, and the other parameters can be defined as follow:

- Superconducting resistance (R_{sc})
  Computed with the Power Law (Equation 3), dependant on length (Δx), critical current (I_c), instantaneous current (I_x), critical electric field criterion ($E_c = 10^{-4}[V/m]$), and n-value for HTS (typically given as $n = 25$). E_c and n value are fixed for all the numerical calculations in this work.

$$R_{sc} = \frac{E_c}{I_c}\Delta x(\frac{I_x}{I_c})^n \tag{4}$$

- Joint Resistance (R_j)
  Defined in the connection of the HTS tapes with the current lead. Defining a joint resistance is tricky, given the circulation currents may return via multiple paths in the current lead region. Although a fixed value may not be ensured, an estimate for the order of magnitude is done.

  The scenario considered is for a staircase configuration with indium foil connecting the REBCO tapes with the current lead. Considering uniform potential due to a uniform current feeding, the resistance of the bulk copper is assumed negligible. The connection of two superconducting layers of two contiguous HTS tapes, is done via the path including the thickness of both the HTS tapes copper coating, and the indium foil, as shown in Figure 71:

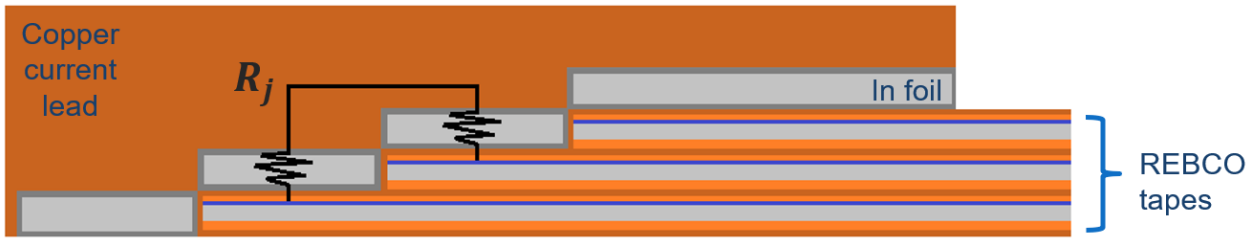

Figure 71: Estimation of joint resistance (R_j) between two REBCO tapes via the current lead. Assuming equal potential in the copper bulk, the resistance includes the thickness of both indium foil and the REBCO tape copper coating, considering the area of the staircase steps.

Under those assumptions, the joint resistance is the result of adding both indium foil and copper coating from both REBCO tapes, considering the resistivity [144] and dimensions of each material, as:

$$R_j = 2(R_{CuHTS} + R_{In})$$

$$R_j = 2\left(\frac{\rho_{Cu}h_{Cu} + \rho_{In}h_{In}}{wl}\right) \tag{5}$$

where ρ is the electrical resistivity as a function of temperature, h is the thickness of the layer, w is the width of the REBCO tape, and l is the length of the staircase step. Table 5 shows the values for 20-kA-class STARS and L-RAISER geometries:

Table 5: Staircase geometry values for 20-kA-class STARS and L-RAISER, to estimate joint resistance R_j

	20-kA-class STARS	L-RAISER
Width [mm]	12	4
Staircase step length [mm]	18	32
Temperature [K]	20	77
Joint resistance [$n\Omega$]	1.5	30

While this is an estimation based on bulk material geometry and assuming a good bonding between different materials, in reality, an experimental resistance may be several times higher than the theoretical expectation, due to microscopic irregularities that bond the two surfaces. Larger experimental joint resistances where observed in the 100-kA-class STARS conductor [42, 43], as well as significantly larger contact resistance between REBCO tapes than expected in the short-straight HTS cable [113, 137].

- Mutual inductance (M)
  Computed in function of the coupling factor k, defined as the ratio of the areas between the inner (L_i) and outer conductor (L_j). Also note that, given the geometry with concentric and coaxial circular coils with the same turns, the maximum theoretical value of mutual inductance is that of the inner conductor ($M \leq L_i$). The relationship between the mutual inductance M and coupling factor k are given by:

$$M = k\sqrt{L_i L_j} \quad , \quad k = \frac{A_i}{A_j} \quad , \quad L_i > L_j \tag{6}$$

- Coupling factor (k)
  As it is related with the amount of power that may be transferred from one HTS tape to the other, it is considered within two possibilities:

  – Geometric
    It is the ratio of inner and outer areas as described in the mutual inductance. It assumes that all the magnetic field lines in common are perpendicular to the cross sectional area of the coils, as an ideal coupling based on the geometric alignment between two coaxial coils.

  – Reduced
    In a real conductor there are changes of magnetic permeability (e.g. air, copper, stainless steel jacket, surrounding ferromagnetic structures, etc.), which may change the direction of magnetic field lines in space. Eddy current losses and hysteresis losses may also be produced in surrounding materials, that reduce the power transfer from one HTS tape to the other, which is reflected as a reduced coupling factor, lower than the geometric case.

- Contact resistance (R_c)
  The contact resistance between HTS tapes may depend on the mechanical pressure between them, the thickness of the solder material with which they are bonded, or both (as by using Indium foil) . A low contact resistance facilitates the share of the current across HTS tapes, which is important for stability when there is a non-uniform current distribution present. For this model, as there are only contact resistances at the edges next to the current feeder, they are considered to be zero to set a uniform current feeding.

The full formulation of the equations is included in Appendix A.

The smallest circuit scenario is to include two HTS tapes to define the circulation current between them, while adding a stabilizer branch allows to grasp the induced current in the stabilizer during the ramping phases. This 2 HTS tapes circuit is shown in Figure 72:

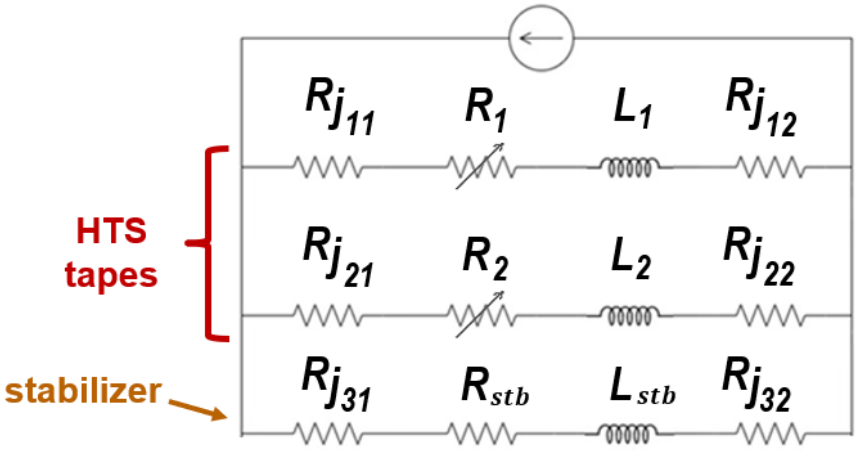

Figure 72: Constant Temperature RL Circuit for 2 HTS tapes plus stabilizer branch. The superconducting resistance R is represented as a variable resistor, the self-inductance L is set by the geometry of the strand, and R_j is the joint resistance between branches at both current lead ends.

The RL circuit model reproduces the current distribution among a given number of HTS tapes. In the case of having 2 HTS tapes, a direct comparison can be made with the circulation currents analytical model for two filaments derived in [85], given as:

$$\tau = \frac{L_1 + L_2 - 2M}{2R} \tag{7}$$

$$\Delta I = \frac{L_2 - L_1}{4R} \frac{dI_0}{dt} \exp\left(-\frac{t}{\tau}\right) \tag{8}$$

where ΔI is the circulation current, L_1 and L_2 the smaller and larger inductance of each filament, dI_0/dt the value of the ramp rate applied (not the time derivative of the input current), M the mutual inductance, R the joint resistance between filaments, and τ the decay time constant.

Note that the analytical circulation current model is derived for the condition of a trapezoidal

input current. Then we can directly observe from Equation 8 that the magnitude of the circulation current ΔI increases with the inductance difference $L_2 - L_1$ (scaling with the size of the coil) and the ramp rate dI_0/dt applied. At first glance, although the inductance difference term may suggest that the size increase becomes increasingly prohibitive, other phenomena is involved in the limitation of the circulation currents magnitude, and how the current evolves while accounting superconducting current paths.

In order to validate the simulation model, a comparison was done with the analytical equations for circulation currents, in a 2 HTS tapes case. The analytical equations were derived for a constant joint resistance value, so when running simulation with a low load factor of the HTS tapes, where the resistance in a branch remains roughly constant, the simulation matches the analytical equations, shown in Figure 73 for a representative trapezoidal current waveform:

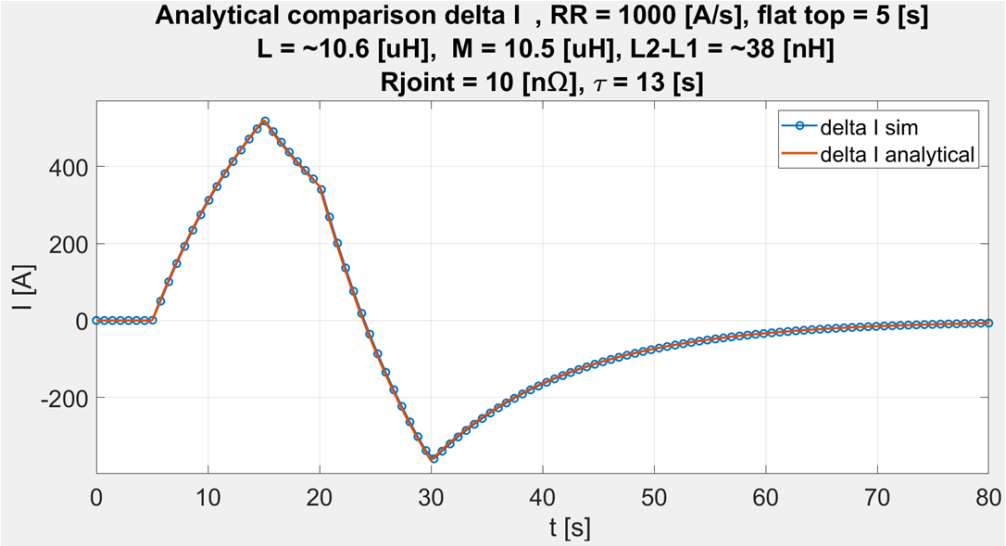

Figure 73: Circulation currents calculation. Comparison of analytical equations for circulation currents under a constant joint resistance (orange line), versus simulation model for 2 HTS tapes (blue line) with variable superconducting resistance. The simulation can reproduce the analytical case, under the condition that the current in the HTS tapes is low enough, to not significantly change the superconducting resistance of the HTS tapes.

To grasp better the comparison between the analytical equation and the simulation, is convenient to add a clarification. The circulation current analytical equation (8) for 2 HTS tapes is defined on a loop that connects them via a joint resistances with a fixed value.

For the simulation, additional to the joint resistances, there is the additional term of "superconducting" resistances in the loop, depending on the load factor (I/I_c, ratio between the current in the branch to the critical current of the branch). As such, overlap with the analytical equation happens when the load factor is low, while at high load factor the simulation accounts the additional variation of overall resistance in the loop where the circulation currents flow.

6.3 Constant Temperature R circuit

On the other hand, to evaluate how the current distributes in a straight simple-stacking HTS cable, a resistance (R) only model was developed. The R circuit model does not consider inductance terms, as they are negligible in a straight cable configuration, yet it allows to subdivide the cable in the longitudinal direction of the cable, to account the effect of the contact resistance into the current redistribution.

The equations of the model are derived via Kirchhoff's Voltage Law (KVL), to define the loop currents along the defined resistance grid, that includes superconducting resistances R_{sc}, stabilizer resistances R_{st} and contact resistance R_c.

Similarly, the superconducting resistances R_{sc} are computed based on the Equation 4 as given by the Power Law. The contact resistance R_c is defined by the contact area and geometrical dimensions of the copper that connects the superconducting layers between the HTS tapes. The stabilizer resistance R_{st} accounts the equivalent resistance obtained by the cross-sectional area and length of all the copper present in the HTS tapes and copper conduit.

A resistor grid for five HTS tapes, a stabilizer branch, and contact resistances between HTS tapes, is shown in Figure 74:

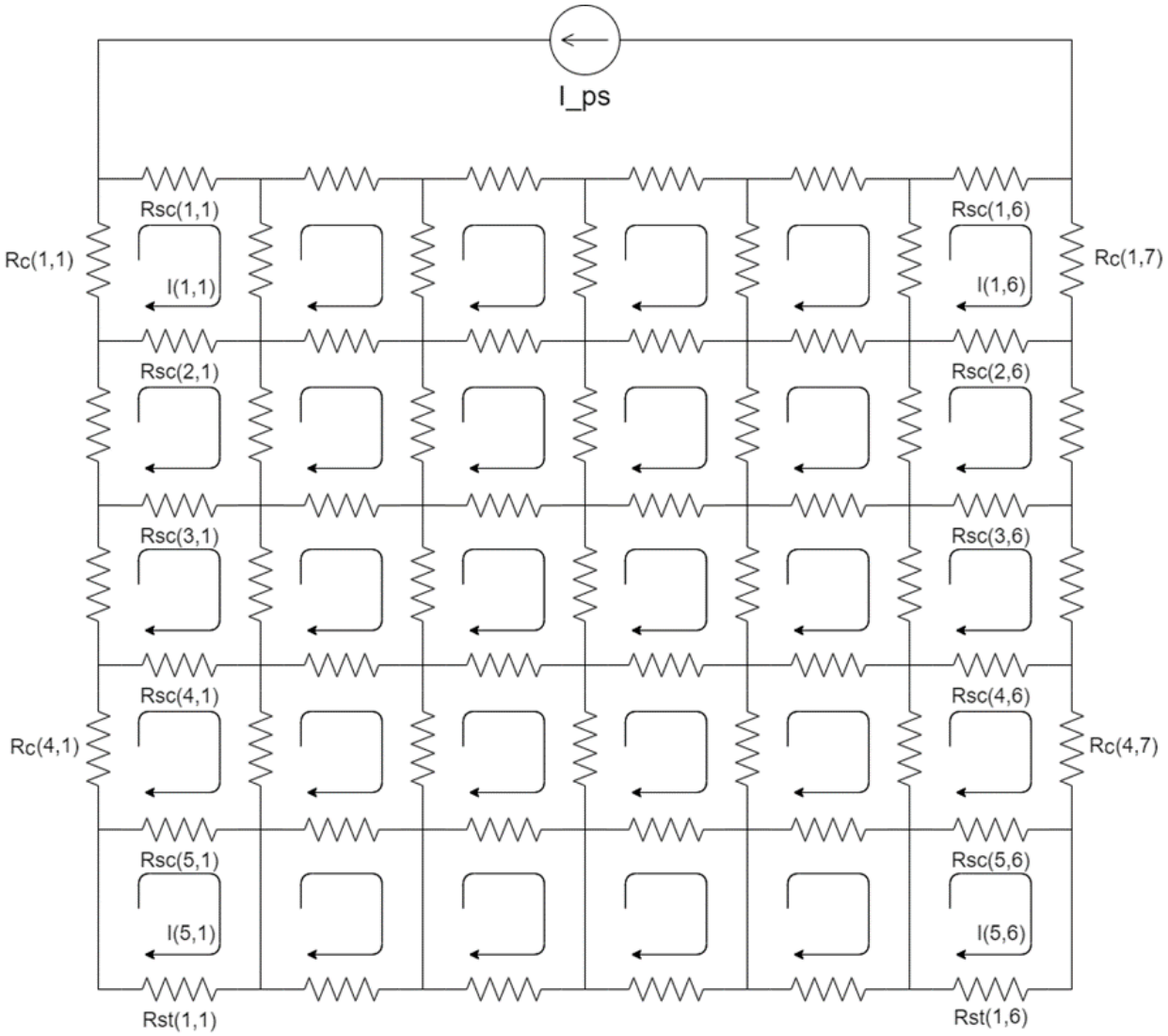

Figure 74: R circuit model, for 5 HTS tapes plus a stabilizer branch (lowermost branch), making 6 mesh divisions along the longitude of the cable. The model considers contact resistances between each 6 divisions was chosen as the minimum mesh value where a grasp of the current distribution can be observed. Applicable for the worst-case scenario of current feeding and NUCD, as observed in the Short-straight HTS conductor experiment.

By dividing the cable in six meshes in the longitudinal direction, is considered adequate to be able to grasp the current redistribution that may occur in the HTS tapes, while keeping a small mesh size, reasonable computing time and convergence of the numerical solver.

6.4 Simulations for experiments

In this section the numerical calculation results are shown for both models, comparing the simulation results with experimental data, for the three experiments (short-straight HTS cable, 20-kA-class STARS, L-RAISER). Additionally, based on the insights and results, an extrapolation is done to how current distribution may look in a large simple-stacking HTS magnet, in this case the double pancake inside the ITER Toroidal Field Coil (TFC).

The calculations are based on a five HTS tape model, which was the number of tapes used in the short-straight HTS cable and L-RAISER experiments. For the case of the 20-kA-class STARS, as it used 15 HTS tapes in total, a simplified 5 HTS tape model is also used, by assuming proportionality in the calculation conditions, so one HTS tape in this model version represents the added effect of 3 HTS tapes. The general model for 5 HTS tapes plus a stabilizer branch, as what was used in the coiled cable calculations, is shown in Figure 75:

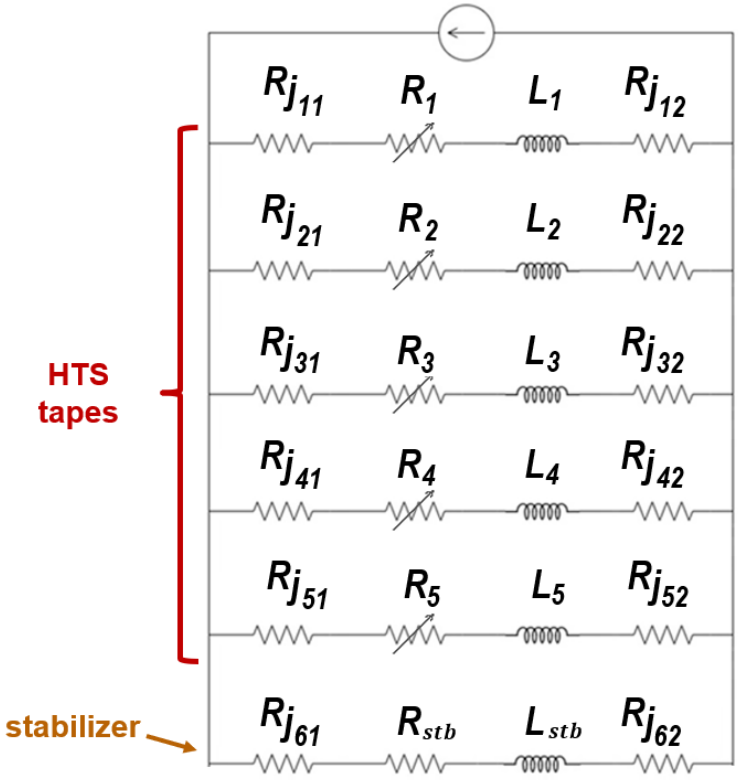

Figure 75: RL circuit model for 5 HTS tapes, plus stabilizer branch. Applicable for coiled cable configurations where inductance variation is present, such as the L-RAISER experiment. Uniform current feeding is considered (no vertical contact resistance), and joint resistance that control the circulation currents decay rate and recirculation to other HTS tapes.

6.4.1 Short-straight HTS cable

The R circuit shown in Figure 74 was used to compute the current distribution and measured voltages for the straight sample.

While the evolution of voltages was as expected, the voltage values were found to be two orders of magnitude lower to what was obtained in the experiment. The reason was the contact resistance value, which was higher in the experiment than the theoretical value initially used in the calculation, which was measured and indeed resulted to be two orders of magnitude higher in the experiment. Once using the experimental contact resistance, the voltages obtained for the simulation and the measured experimental data were found on close agreement, as shown in Figure 76:

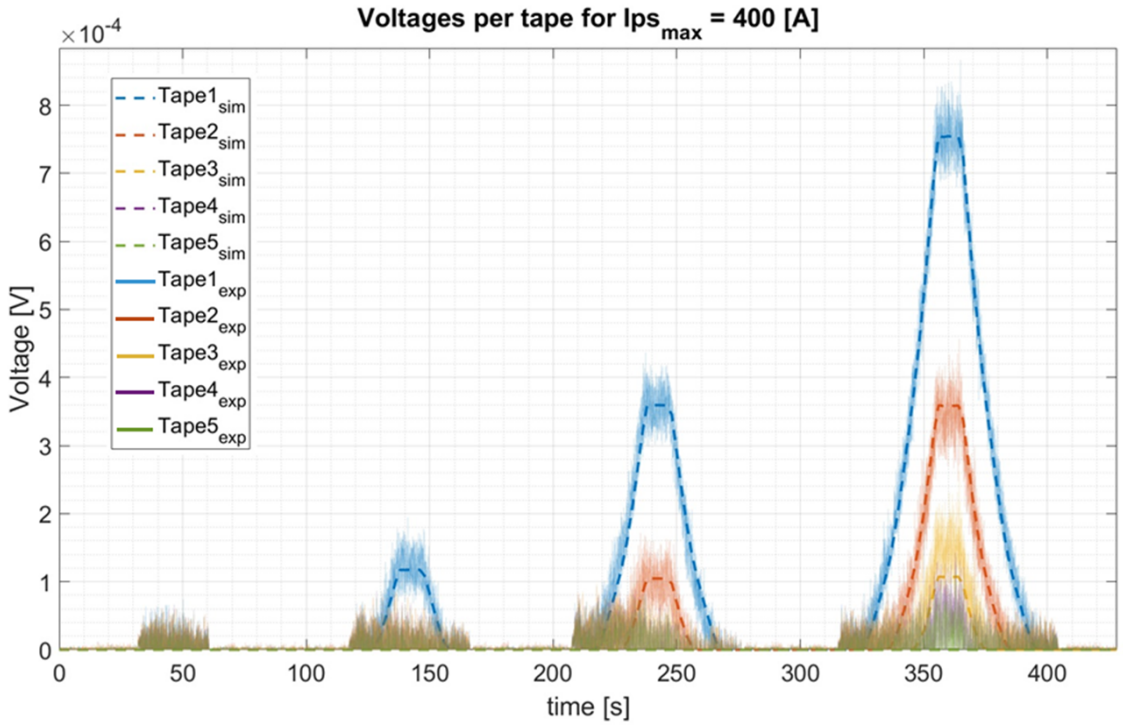

Figure 76: Simulation of the Short-straight HTS Cable, 1. Voltage comparison between experimental data and numerical simulation, under a worst-case NUCD current feeding. The simulation manages to reasonably reproduce the experimental measurements [137].

The current distribution could not be directly measured from the experiment, but it was derived from the numerical calculation based on the voltages and tape length, according to the Ohm's Law ($V = RI$).

For a better visualization, a two dimensional representation was performed in a square grid, where the colors indicate the amount of current that flow in each superconducting resistance, considering that each HTS tape was divided in 6 segments. The current distribution of the superconducting layers is shown in Figure 77, for the time instant where the current in the sample reached 127 A:

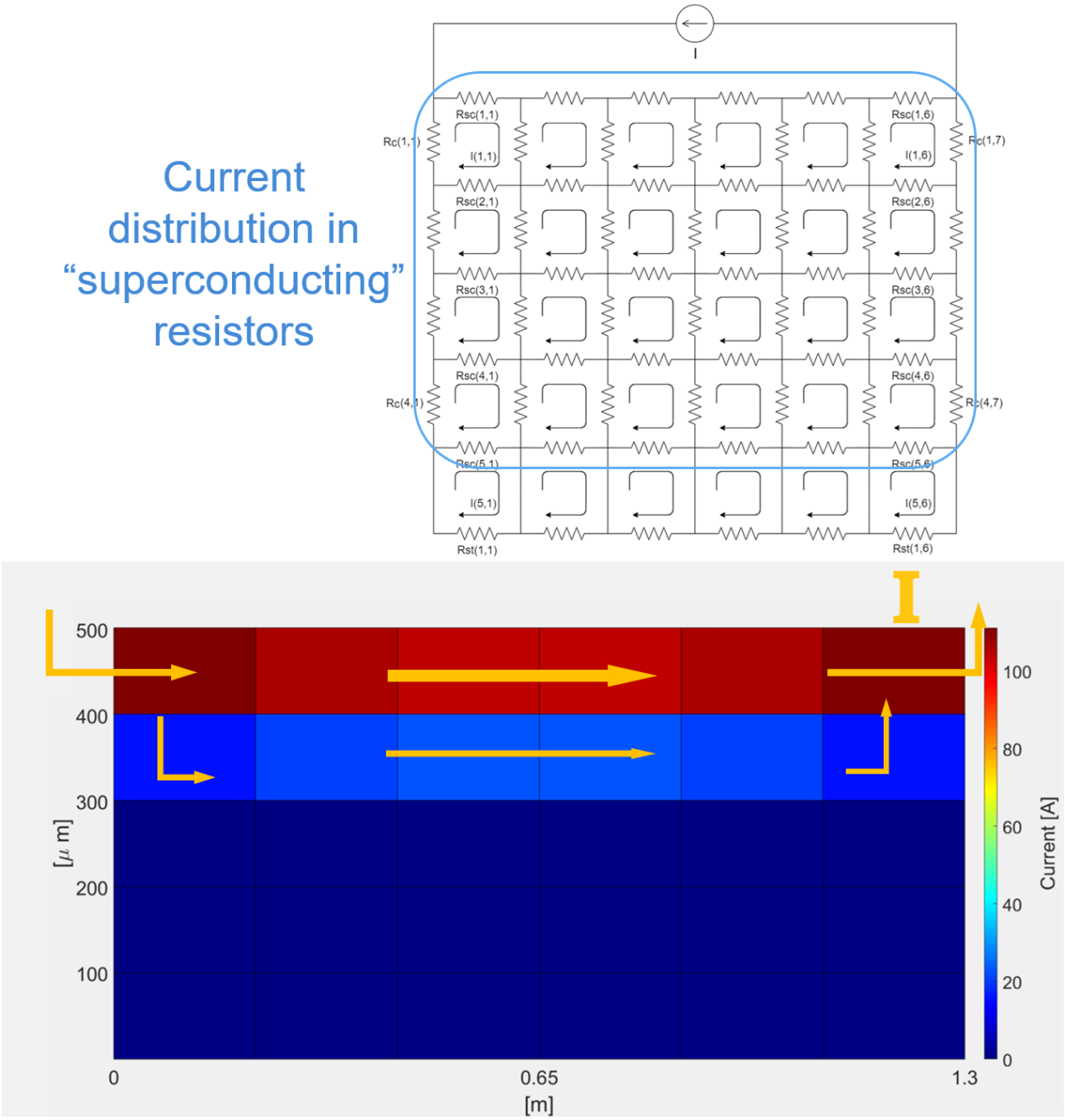

Figure 77: Simulation of the Short-straight HTS Cable, 2. Current distribution for 1.3 m stacked HTS cable, considering 6 mesh divisions in the horizontal direction, at total current of 127 A. Each square corresponds to one "superconducting resistance" for each RE-BCO tape superconducting layer, and the color indicates the current magnitude flowing through it. Once the critical current is almost reached in the HTS tape closer to the current feeding point, then a step-wise current transfer occurs to the HTS tape right below it.

We can see that, under a worst-case scenario of NUCD, and current fed through the edge of the tape stack, the current in the closest HTS tape is saturated before the current starts flowing into the next HTS tape. Hence, when reaching close to the critical current value, there is a transfer of current towards the immediate HTS tape below.

The step-wise current transfer keeps occurring in a stable manner, as the total current keeps increasing. Figure 78 shows how the current distribution may look at the time-step where the current was 400 A:

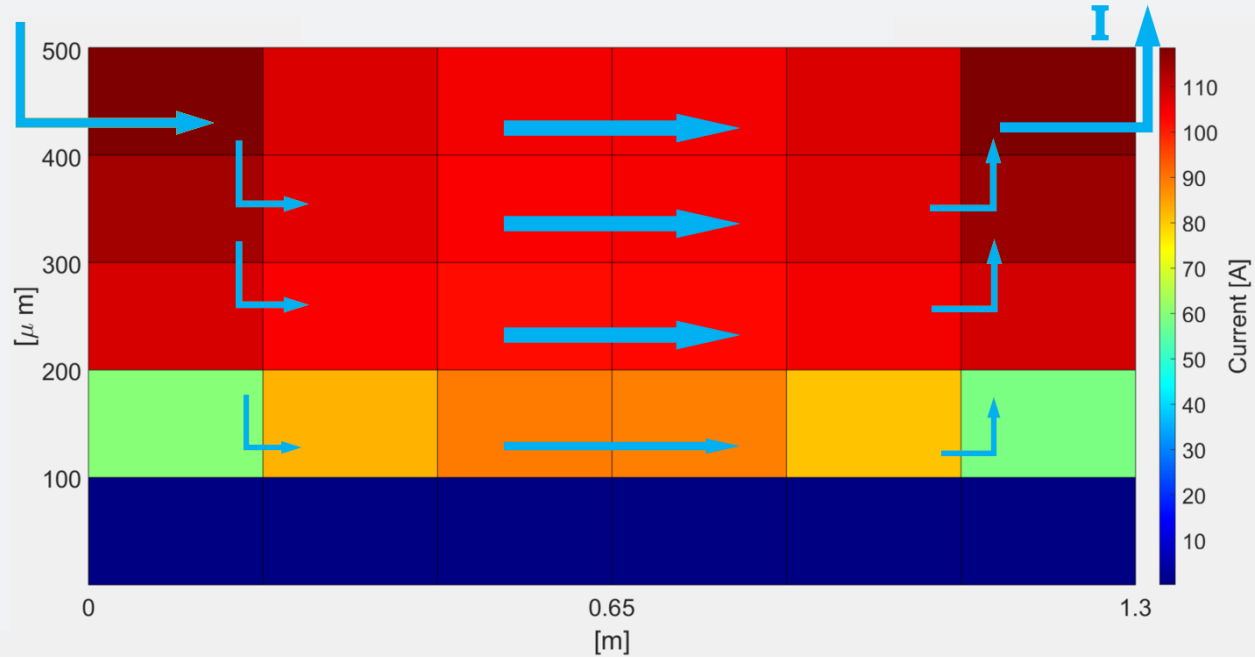

Figure 78: Simulation of the Short-straight HTS Cable, 3. Current distribution for a 1.3 m stacked HTS cable, considering 6 mesh divisions in the horizontal direction, at total current of 400 A. As the critical current of one HTS tape is closed to be reached, the superconducting resistance increases, then a stepwise current transfer occurs successively, gradually forming the voltage steps seen in Figure 76. From [137].

It was confirmed that stable current transfer between HTS tapes in a simple-stacking approach is available, even when the current initially flows in a non-uniform manner. The following numerical calculations explored the behavior of the simple-stacking concept in coiled cable configurations.

6.4.2 20-kA-class STARS

Now for a coiled configuration, and to continue with the comparison with the experiments so far, we look into the 20-kA-class STARS case. Figure 79 shows the schematic of the coil and isometric view, while the tracing of the HTS tapes as single filaments is done by BSMag Matlab library [140].

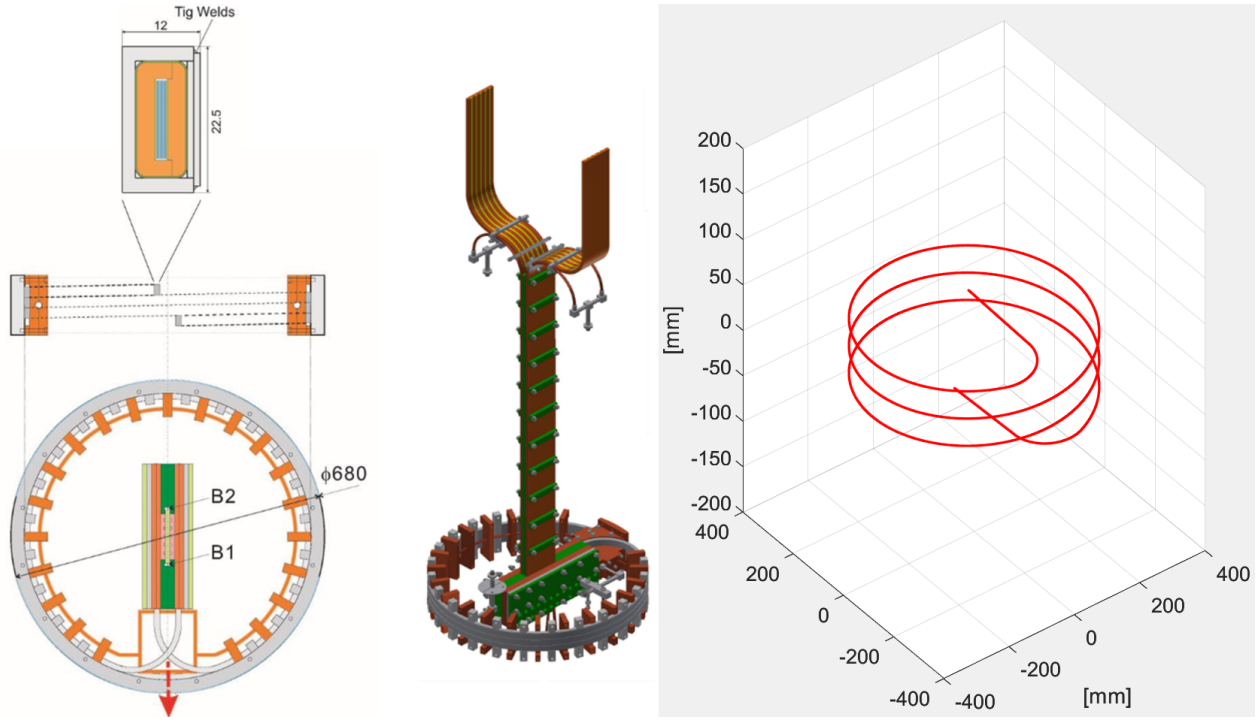

Figure 79: 20-kA-class STARS 6 m coiled sample. Left: Top-view schematic. Center: Isometric view of 20-kA-class coiled sample plus current lead extensions. Right: Filament tracing for the HTS tapes length.

From the filament tracing, the self-inductance of each HTS tape is computed via the Neumann's equation for mutual inductance, by dividing each filament into a mesh, and computing within the same filament the mutual inductance of the mesh elements. The calculation results in an average value of 10.6 μH, with slight inductance variation from innermost to outermost filaments. For the stabilizer filament, it is considered to be towards the central axis of the coil, at the center of the inner stabilizer region.

The joint resistance between REBCO tapes was estimated to be on the range of 1 $n\Omega$, considering the staircase connection between tapes with Indium foil, and the mechanical pressure applied to the HTS tapes with bolts in the current lead section. The critical current was estimated by considering the 15 HTS tapes used and operating at 20 K, for a value of around 54 kA with self magnetic field. The coupling factor k between HTS tapes was adjusted accordingly, within a smaller but close value to the theoretical value.

A numerical calculation was then performed, considering no background magnetic field, and using as input for the calculation the same current waveform, that was recorded experimentally. Figure 80 shows the calculation of the current distribution for a simplified 5 HTS tapes model, showing on top the decaying residual magnetic field produced by circulation currents, and on bottom the current per HTS tape, where they overall reproduce the same experimental decay time.

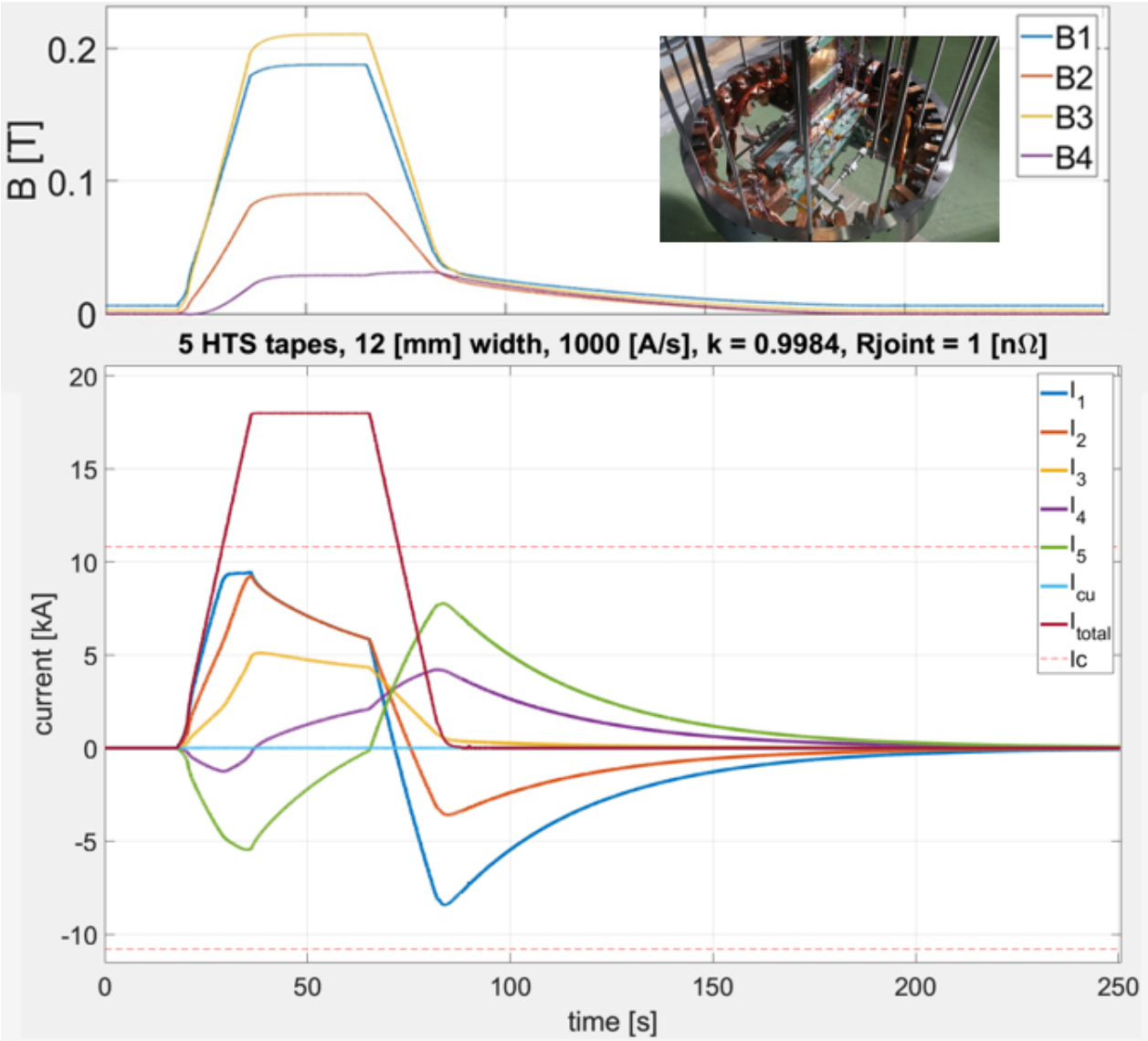

Figure 80: Simulation of the 20-kA-class STARS, 1. Top: Experimental data for magnetic field measurements, under a trapezoidal input current of 18 kA and 1 kA/s. Bottom: Numerical calculation using a 5 HTS tapes RL simplified model, obtaining the current distribution per HTS tape. The decay time between experiment and simulation matches, while there is a current evolution influenced by the joint resistance and mutual inductance.

6.4.3 L-RAISER

The Inductance (L) RAISing ExpeRiment (L-RAISER), aimed to further test the stability of a simple-stacking HTS coil with a fast ramp-rate. Figure 81 shows the schematic of the solenoid and the tracing of the filaments for the HTS tapes contained within the main body of the solenoid.

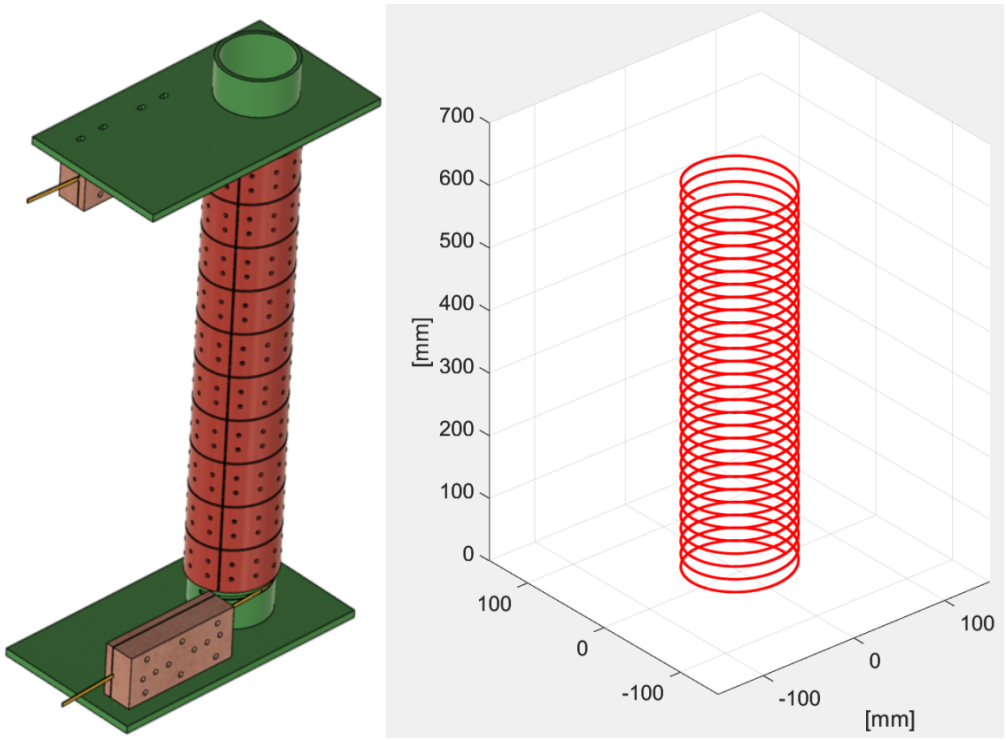

Figure 81: L-RAISER 10 m solenoid. Left: Isometric view schematic, with HTS tapes hidden by pressure plates, that surround them along the length of the solenoid. Right: Filament tracing for the 5 HTS tapes within the bobbin region. Coil leads are omitted

A similar procedure was done for the 20-kA-class STARS calculation. The self-inductance is calculated via the Neumann's equation for an average value per tape of 16 μH, and the critical current is assumed as constant at 600 A as the threshold at self-magnetic field. The coupling factor k is assumed by the geometric value obtained by the area ratio between the HTS tapes according to Equation (6), for which a joint resistance would be expected to be higher than what was obtained .

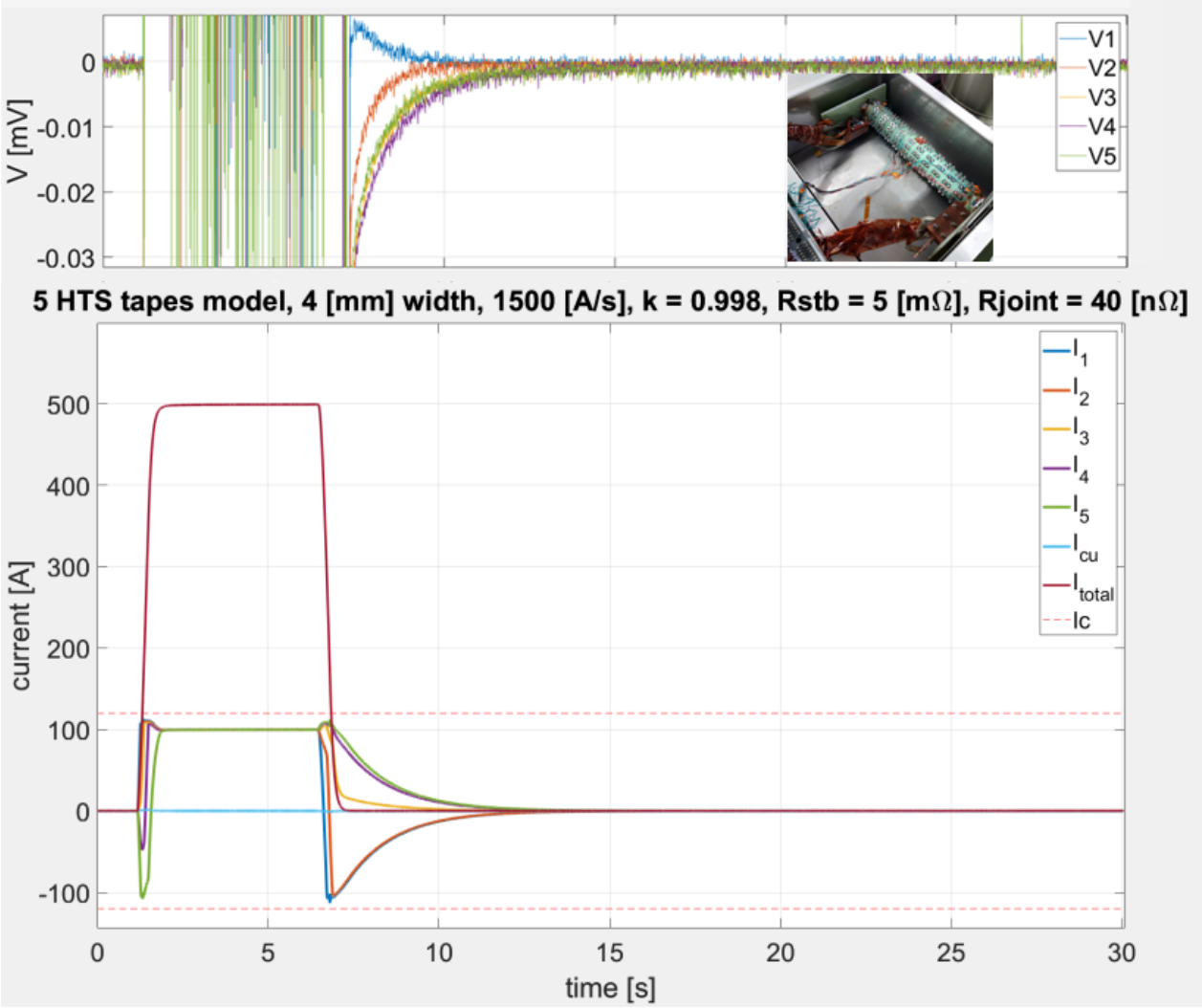

Figure 82: Simulation for L-RAISER, 1. Top: Experimental data for 500 A and 1500 A/s, corresponding to the Case 2 of REBCO with a staircase shape (voltage taps decay within 3 s). Bottom: RL circuit simulation for 5 HTS tapes, for a direct comparison with experiment. After the input current becomes zero, the decay is within 3 seconds, as observed in the experiment.

6.5 Calculation for special cases

While there is agreement between the decay time in the experiments and the one obtained via numerical simulations, there are additional factors that need to be taken into account. The following section delves into exploring changing some of the calculation assumptions, which modify the waveform, and may have implications on a simple-stacking HTS cable stability operation range, besides matching the decay time between experiment and simulation.

6.5.1 Slow ramp rate in the 20-kA-class STARS conductor

The 20-kA-class STARS conductor was only tested on ramp rates equal or above 200 A/s. As known, when there is a fast ramp-rate while charging a coil, the NUCD is enhanced if there is impedance difference in the filaments. A numerical calculation was performed at slow ramp-rate, where the current distribution would be expected to be more uniform, the result is shown in Figure 83.

The current variation between HTS tapes is significantly lower when applying a trapezoidal input current under a slow ramp-rate, computed for 10 A/s. We may observe the current evolution in each phase that:

- Ramp-up: Currents evolve closely to each other in magnitude.
- Flat-top: Currents stabilize to a constant value (slightly different between each other due to the different length of the filaments).
- Ramp-down: Currents gradually decrease while being close to each other in magnitude.
- After ramp-down: Circulation currents decay according to the effective inductance of the coil, which accounts the mutual inductance of the HTS tapes (for a 2 HTS tapes case, as described previously, with $\tau = \frac{L_1+L_2-2M}{R_j}$). The decay time is on the range of 100 s, as observed experimentally in the 1 kA/s case.

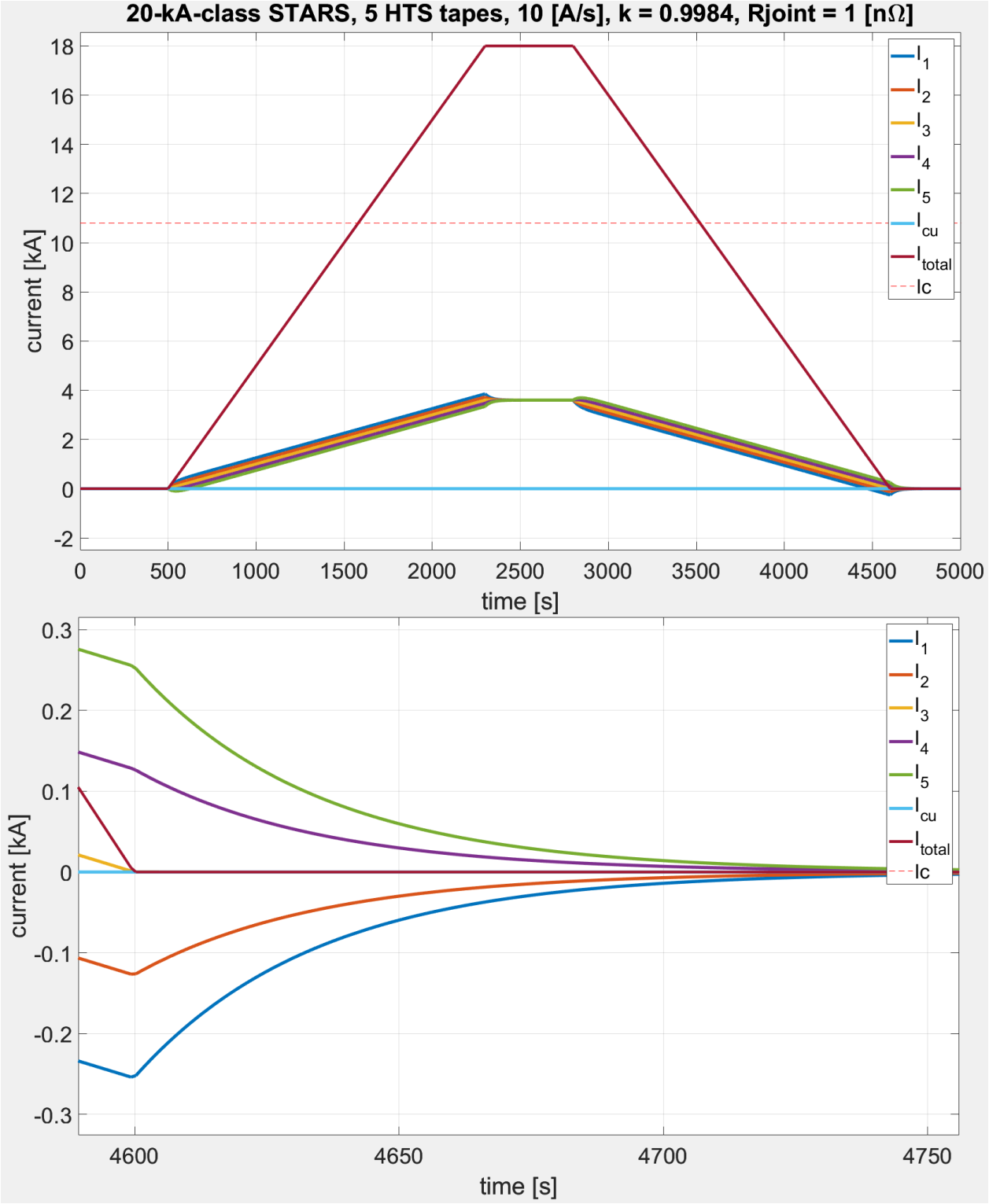

Figure 83: Simulation of the 20-kA-class STARS conductor under trapezoidal input current at 10 A/s ramp-rate. Currents evolve close in value to each other during the ramp-up, stabilize to a constant value in the flat-top, and decrease with lower variation among them. After the input current becomes zero, currents decay to zero according to the effective inductance and overall joint resistance (e.g. $\tau = \frac{L_1+L_2-2M}{R_j}$ in a 2 HTS tapes case).

6.5.2 Coupling factor comparison

In the modelling of the equations for the resistance inductance (RL) model, the mutual inductance between HTS tapes define how strongly HTS tapes magnetically interact with each other, and the amount of current that they induce between them. A stainless steel jacket and surrounding materials (ferromagnetic or not) may slightly modify the mutual inductance (coupling factor) between HTS tapes, and consequently, the decay time. This can be seen in the Equation 7 for the circulation currents time constant, where the decay depends both on self-inductance and mutual inductance.

Neumann's equation may be used to obtain the mutual inductance between current filaments, solely based on geometry of these filament respect to each other, and assuming they are under a vacuum environment. However, whereas this mutual inductance may be defined on geometry alone, in reality, interactions and energy losses with the environment may effectively reduce how strongly the filaments interact magnetically between each other.

Assuming the joint resistance is known, having a fixed value due to the geometry materials and temperature, coupling factor k may be slightly modified depending on the overall configuration of surrounding materials. A slight change in the coupling factor modifies the evolution of the current waveforms in each HTS tapes, and notably, the overall decay time of all the currents.

This mutual inductance change may be not so negligible in the 20-kA-class STARS conductor sample. Instead of SS316 (non-magnetic), a SS304 (slightly magnetic) stainless steel alloy was used for the conductor jacket and surrounding electromagnetic supporting ring. While experimentally, observing the coupling factor change effect would need adding or changing structural materials, a simulation can show the effect of a slight change in the coupling factor, shown in Figure 84.

A similar situation may be expected in larger magnets, where there may be a larger volume of materials nearby, where energy may be dissipated when current is changing in the HTS tapes, shown in Figure 85. These explorations aim to give elements to point out what could be a more realistic current distribution happening in a real simple-stacking cable, more details are outlined in the Discussion section afterwards.

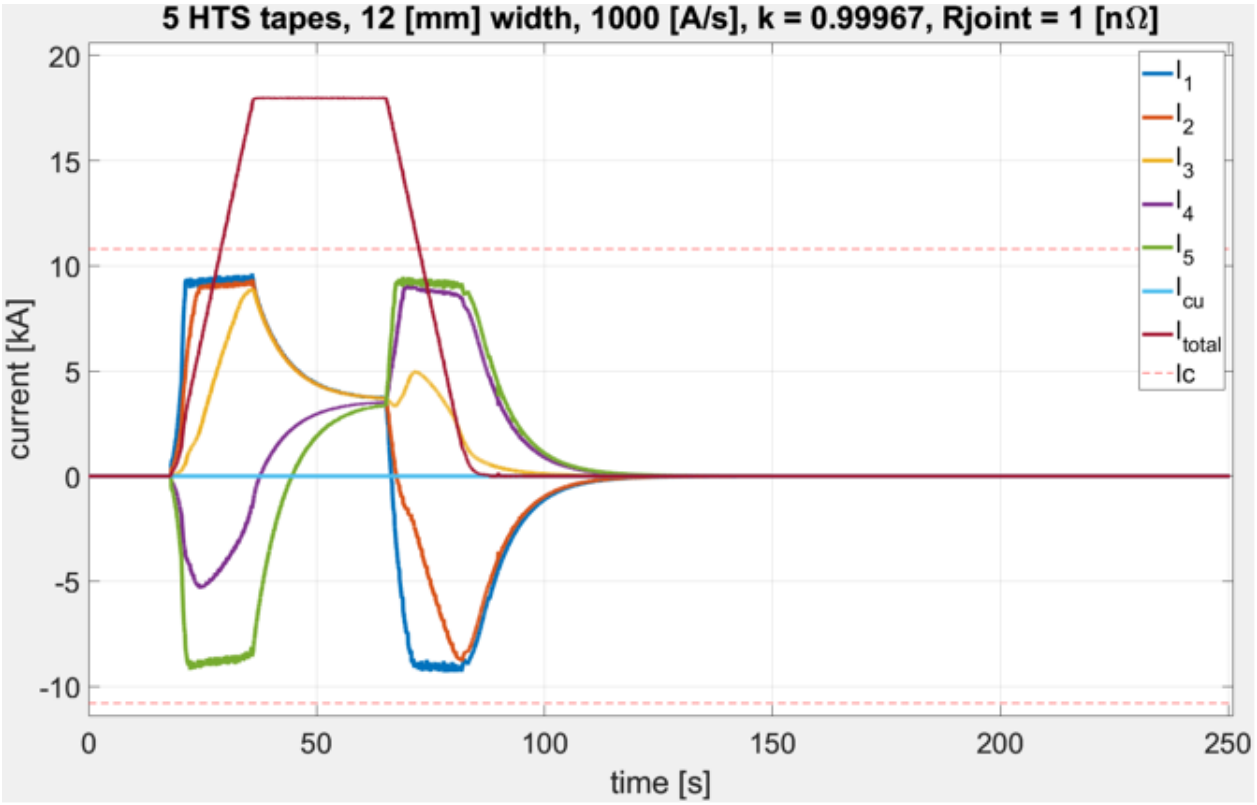

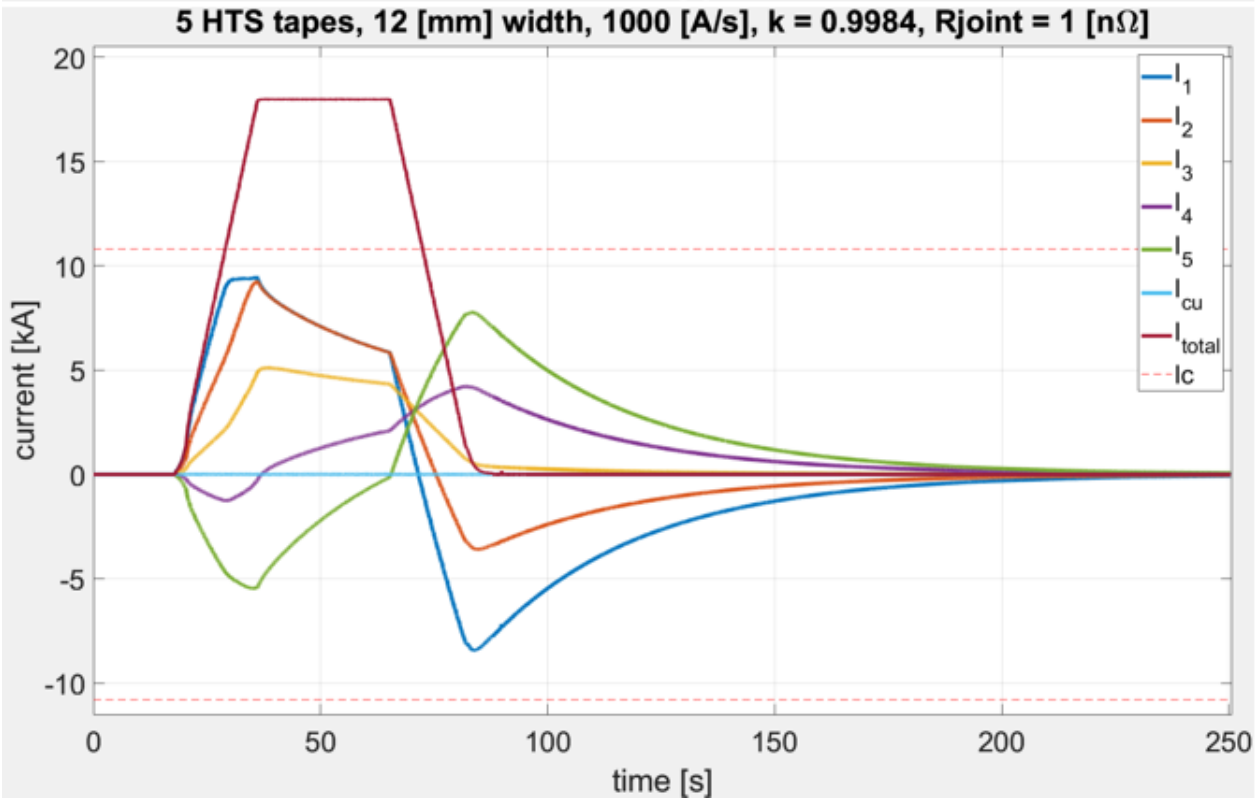

Figure 84: Coupling factor variation for 20-kA-class STARS conductor. Top: With a geometric coupling factor ($k = 0.99967$), the current decays within 40 s after ramp-down finishes. Bottom: With a reduced coupling factor ($k = 0.9984$), the overall current distribution matches better the 100 s decay observed experimentally.

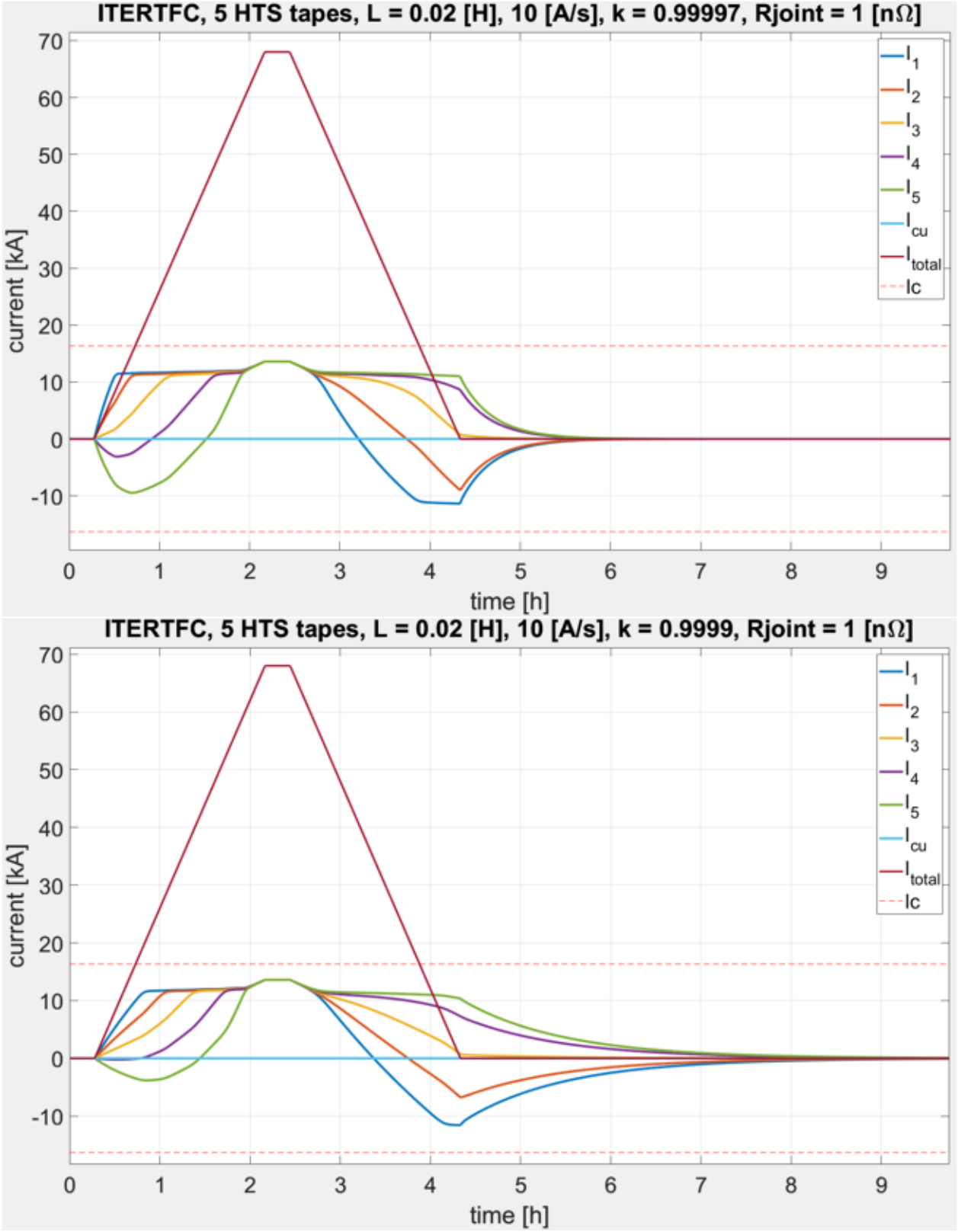

Figure 85: Coupling factor variation for ITER TFC model. Top: With a geometric coupling factor ($k = 0.99997$), the current decays within 1 h after ramp-down finishes. Bottom: With a reduced coupling factor ($k = 0.9999$), the current decays within 3 h, and the margin of the currents respect to the critical current is larger.

6.5.3 Changing critical current

The numerical calculations shown so far make the assumption that the total critical current remains constant for the whole process, with a 20% higher value than what the cable would have at the nominal operating current.

While the constant critical current assumption was token as a representative case, the critical current from a HTS tape depends on the temperature and surrounding magnetic field (both external and self-field). So for a trapezoidal input current, the critical current would similarly change as a function of time. The effects of changing the critical current assumption, either constant or as a function of magnetic field, can be observed on Figure 86.

For a trapezoidal current input, the critical current decreases as the absolute value of the input current increases, due to both the current limit intrinsic to the superconductor, as well as the self magnetic field generated. Still, the current is limited by the critical current, as the resistance of the superconducting layer increases as function of the power law.

Overall, the behavior remains similar for both cases. If the critical current changes as function of time, the critical current still limits the current in each branch during the ramp-up or ramp-down phases. On the other hand, it is worth to note that the critical current in the innermost strands could still be surpassed with a sufficiently fast ramp-rate.

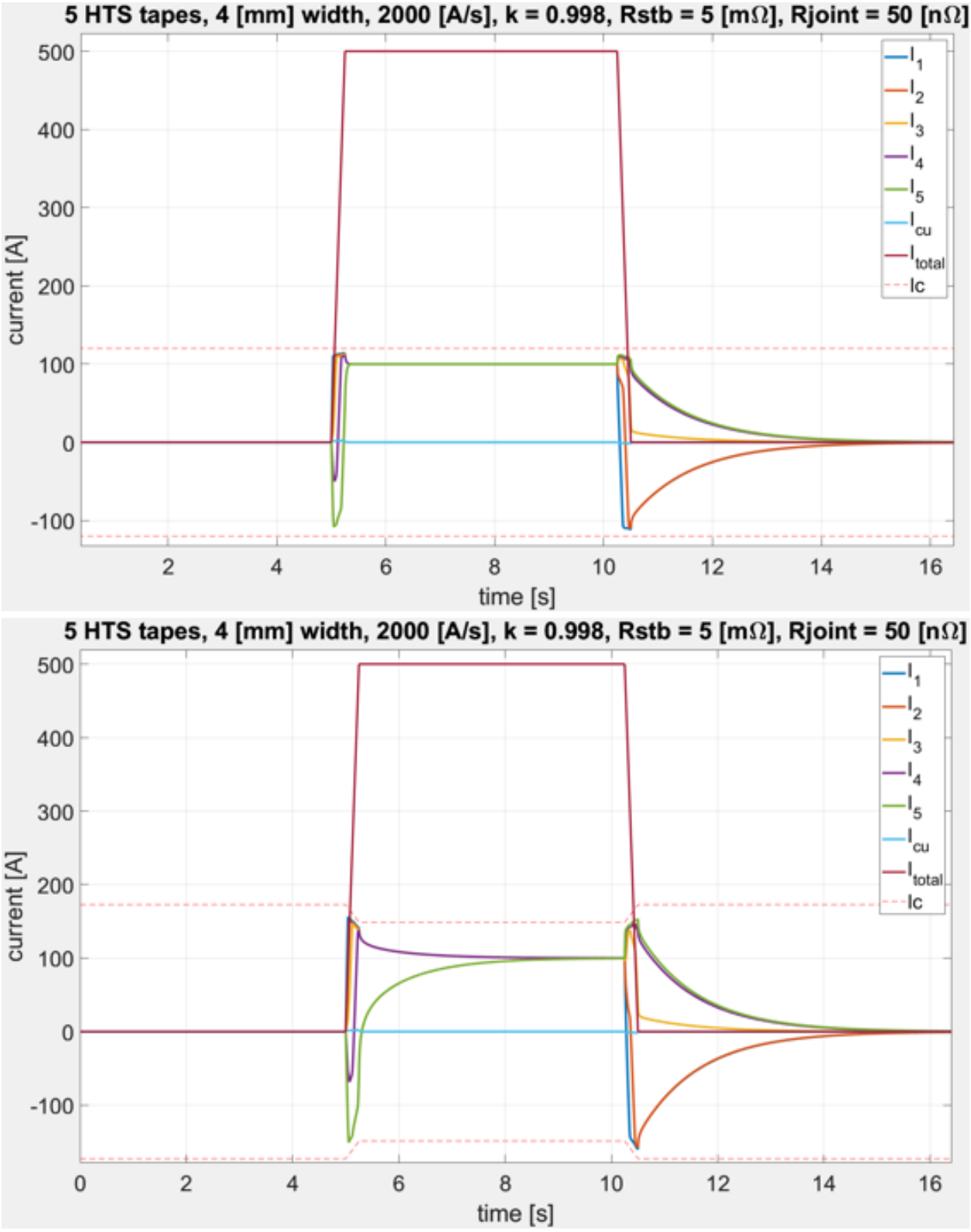

Figure 86: Comparison of critical current variation for L-RAISER. Top: A constant critical current leads to a faster stabilization of currents during the flat-top phase after the ramp-up. Bottom: A changing critical current may slow down the stabilization time for the ramp up, yet during the ramp-down the behavior is practically the same.

6.5.4 Thermal estimations for the 20-kA-class STARS conductor

Two zero-dimensional thermal estimations are presented here, assuming an adiabatic temperature rise with no cooling, to present the increased cryogenic stability by operating HTS at 20 K, thanks to gaining up to two orders of magnitude in the heat capacity of materials, compared to 4 K operation in LTS.

While there are different losses that would contribute to raise the temperature in a conductor (AC losses, hysteresis losses), the focus for this calculation looks only into ohmic losses (dependent on resistance and current, i.e. $P = RI^2$), produced by the flux-flow resistance when getting close to the critical current.

- **One HTS tape in quench-threshold condition during ramp-up phase**

  Recall the heat equation, defined for a material heated via joule effect:

$$Q = \rho V_s C_p \Delta T \tag{9}$$

$$P = \frac{Q}{\Delta t} = VI \tag{10}$$

  where ρ is the density and V_s is the volume of the sample, C_p the specific heat capacity, ΔT the temperature rise, Q the heat energy input. The power P generated as heat, is the heat energy input Q over the time period Δt where it is applied. For the heat generation terms, V is the voltage, I is the current, assuming they are both constant during the heat generation phase.

  Looking into the 18 kA and 1 kA/s case, we make an estimation of what could happen into the innermost HTS tape, by reaching a condition in the flux-flow region, which is the quench threshold region where the tape current is equal to the critical current. Then, considering that the heating is produced constantly during the 18 s that it takes from 0 A to 18 kA, while being on the critical electric field threshold, and the heat be propagated to the whole copper stabilizer of the 20-kA-class STARS conductor. Hence, the zero-dimensional thermal calculation is:

$$\Delta T = \frac{V_c I \Delta t}{\rho V_{cu} C_p} \tag{11}$$

$$V_c = E_c l \tag{12}$$

  where E_c is the critical electric field and l the average length of the HTS tapes in the 20-kA-class STARS conductor, for the critical voltage V_c. I considers taking an equal share of the total current for 15 HTS tapes, on the time t of 18 s where the heat is applied. ρ is the density of the (copper) stabilizer, V_{cu} is the volume of the copper in the conductor including the HTS tapes coating, and C_p is the specific heat as a function of temperature.

  The temperature is calculated for two scenarios, starting from 4 K and from 20 K, for the increased specific heat capacity available in HTS operating at 20 K, compared to what happens with materials at LTS temperature conditions. The result is shown in Figure 87:

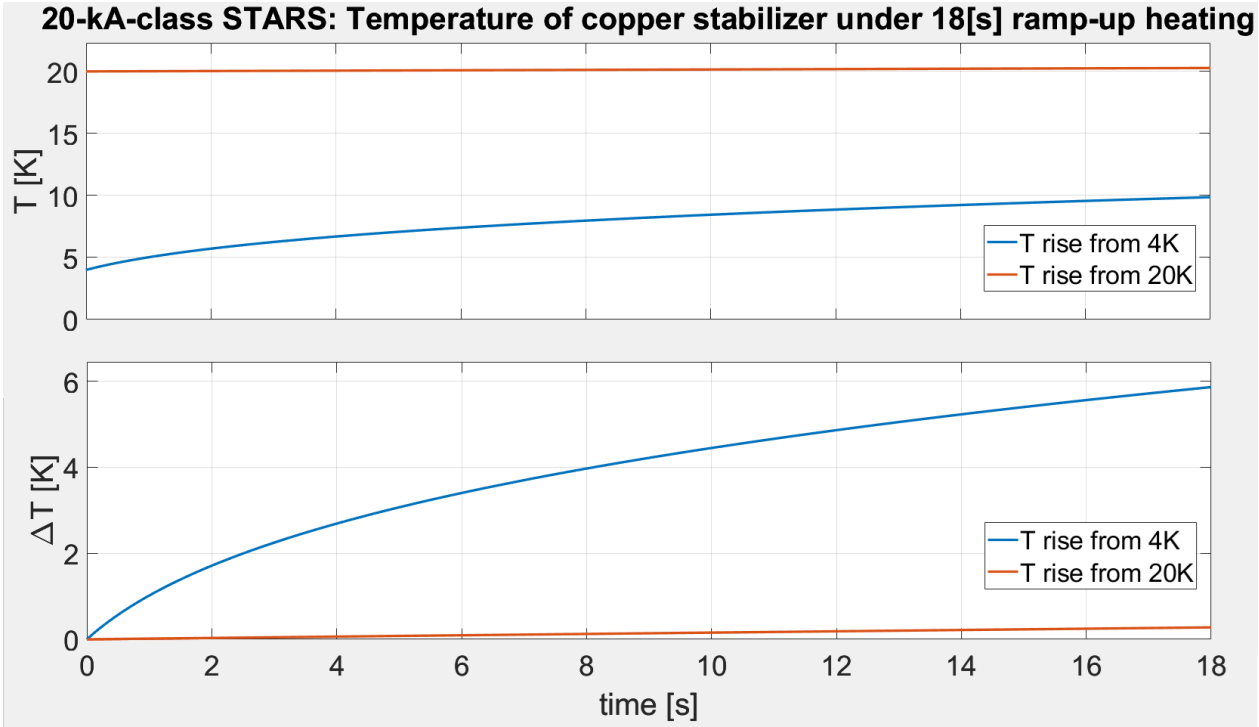

Figure 87: Temperature rise of copper stabilizer in 20-kA-class STARS, under two initial temperature cases, 4 K and 20 K. Assuming that heat is continuously produced during the 18 s ramp-up phase, starting from 20 K temperature rise is around 0.3 K, while starting from 4 K the temperature rise is 5.9 K.

As it can be seen, for the same heat input, the temperature rise is around 5.9 K when starting from an initial temperature of 4 K. In the case of an initial temperature of 20 K, the temperature rise is marginal, within 0.3 K.

- **Ohmic losses for computed current distribution**
  The previous calculation considers a constant heat generation during the whole duration of the ramp-up rate. In reality, as current distribution evolves differently in each HTS tape, some of them are closer to the critical current threshold while others have a wider margin, so the corresponding heat generation differs.

  By using the equation $P = RI^2$, for the instantaneous power generated at each timestep, the ohmic losses per HTS tape are calculated, and the total temperature rise computed. The resulting equation for the heat generation produced in each current branch (both superconductor and stabilizer), is:

$$\Delta T = \frac{RI^2 \Delta t}{\rho V_{cu} C_p} \tag{13}$$

  where R is the instantaneous resistance in each branch (superconducting or stabilizer), I is the instantaneous current, Δt is the time step of the calculation. ρ is the density of the (copper) stabilizer, V_{cu} is the volume of the copper in the conductor including the HTS tapes coating, and C_p is the specific heat in function of temperature.

By taking the computed current distribution in the 20-kA-class STARS conductor from Figure 80, the flux-flow ohmic losses and temperature rise is calculated, at an initial temperature of 20 K. The result is shown in Figure 88:

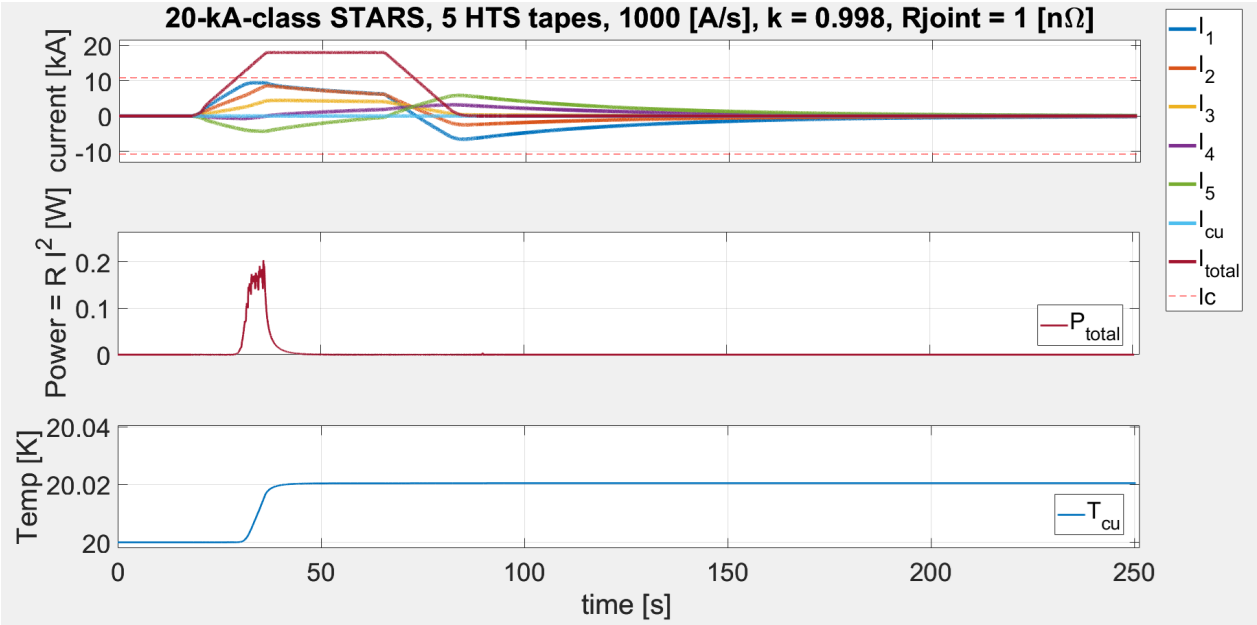

Figure 88: Temperature rise by ohmic losses in 20-kA-class STARS conductor, as produced by each HTS tape, and propagated to the copper stabilizer. Thanks to the higher heat capacity of copper at 20 K compared to 4 K, temperature rise is negligible, even with no cooling.

For the 20-kA-class STARS coiled sample, under a ramp rate of 1 kA/s, the numerical calculation shows still some margin of the current in each HTS tape, relative to the critical current. The first calculation considers only one HTS tape in the critical current threshold for 18 s, while the second calculation includes the instantaneous current in all HTS tapes during the total duration of the input current.

Given the wider margin of the current in some HTS tapes, compared to the critical current, the heat generation resulted lower than the first estimation. The innermost and outermost HTS tapes are the ones that approach closer to the critical current threshold, while the tapes in between generate less ohmic losses by having a wider critical current margin. The resulting temperature rise is still not significant, less than 0.1 K.

7 Discussion

7.1 Extrapolation to large HTS magnet: ITER TFC DP

What might happen in a large inductance magnet? Is simple-stacking enough for stable DC operation? As a first step to check the feasibility, we can extrapolate the current numerical calculation for a reactor-size HTS magnet. As a test case it was chosen the ITER Toroidal Field Coil (TFC), which is a large superconducting magnet meant to operate in DC current, where a numerical calculation for a simple-stacking geometry with HTS tapes may be applied.

Figure 89: ITER TFC. Left: Schematic of ITER TF coil [145], including the mechanical support structure (dimensions of 16.5 m height, 9 m width). Right: Simplified filament tracing for the D-shaped magnet (accurate dimensions can be found in [146, 147]).

A single filament was traced in Figure 89 to exemplify the process, as it was done with the previous 2 coiled samples. In reality, the detailed geometry of how a ITER-TFC magnet made with HTS would be, is yet to be defined. It could include a double pancake approach as of the current ITER-TFC design does, however the higher current density of an HTS cable compared with the current LTS cable design may imply less turns in a different geometry.

A calculation is done based on the design operation values of ITER-TFC magnet system [145–149], assuming 7 double-pancakes inside one ITER-TFC, similar to the current TFC magnet design based on LTS. Then, an estimate of the self-inductance of a single double-pancake segment is obtained, to make a current distribution calculation.

A double pancake (DP) coil consists on two spiral coils formed by the same filament. We can understand the geometry by using a tape as filament, which can be seen in Figure 90.

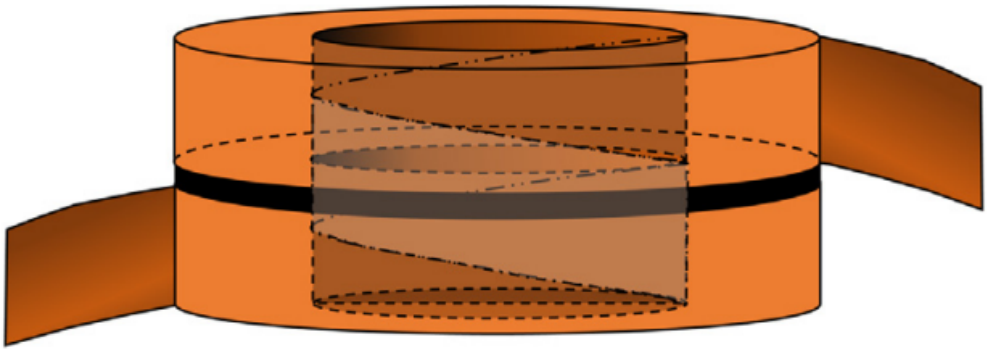

Figure 90: Schematic of a Double Pancake (DP) coil, visualized with a planar tape [150]. The coil starts being wound from the bottom, in a spiral shape inwards. When reaching the inner radius, the tape is shifted one tape width, and the second coil is wound in a spiral shape outwards. The same approach is used when making double pancake geometries in big magnets, with cables that have a square or circular cross section.

Initially the tape is wound in a spiral inwards until reaching the inner radius, from there it's shifted one tape width on top, and the winding continues to form the second coil from the inner towards the outer radius, and finalized until the same turns as the first coil are reached. If a current is fed through one end of the double pancake coil, the current follows the spiral in both coils in the same direction, so the resulting on-axis magnetic field points in the same direction, similar to a single circular coil, yet with more turns the magnetic field magnitude is higher.

In that same idea, the ITER-TFC magnet system is composed of 18 coils, where each coil internally has 5 DP coils plus 2 side DP coils, and these 7 DP coils are connected in series, outlining ultimately the filament that conforms a single TFC unit. We can see the inner assembly on Figure 91:

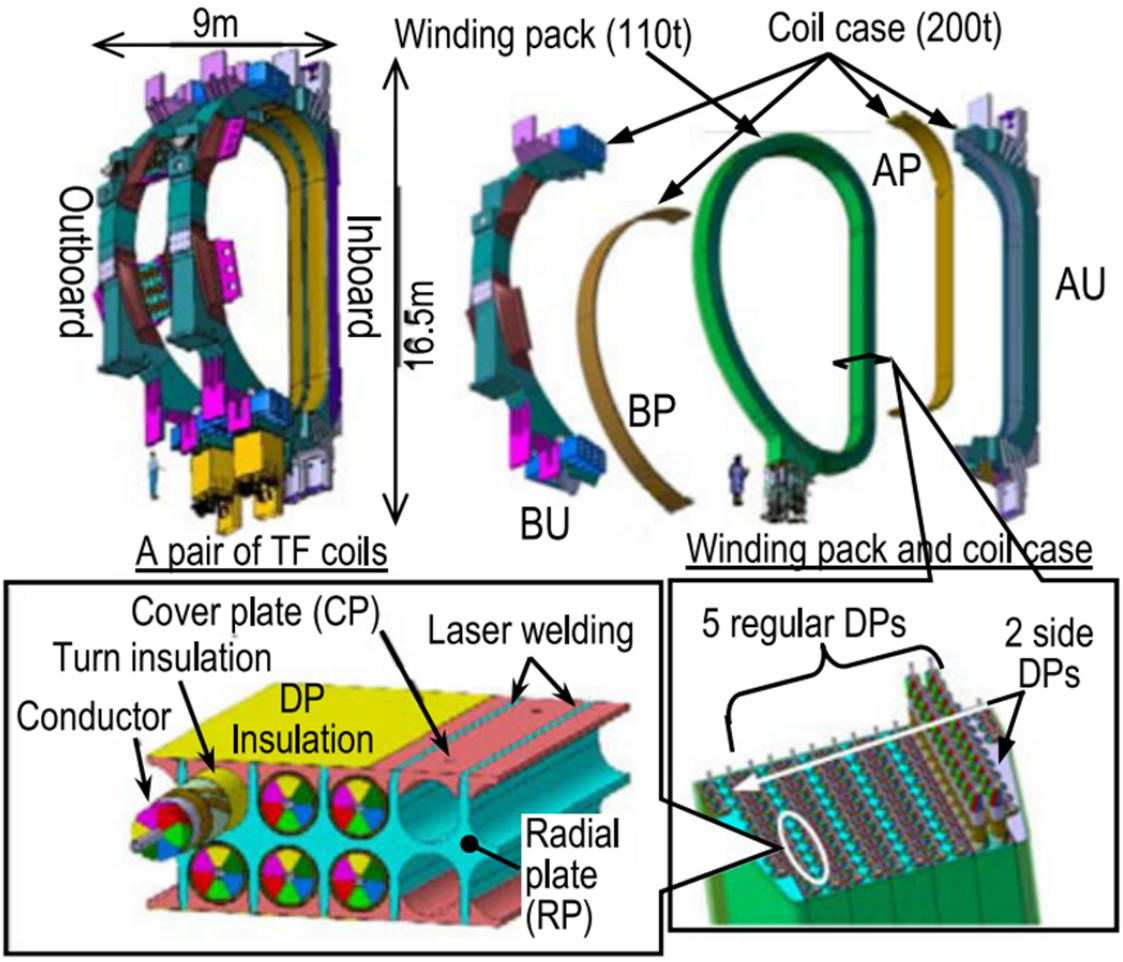

Figure 91: Schematic of ITER-TFC assembly configuration [147]. Each TFC is composed of 5 DP coils plus 2 side DP coils. The DP coils are connected in series, making the current flow in the same direction, adding to the magnetic field strength in the bore of the coil.

The ITER-TFC design uses LTS large-current CICC made of Nb_3Sn [151], so switching to HTS materials may significantly change the geometry, given the different current density and perhaps cross-sectional area, in the case using a STARS-like conductor with a squared cross section.

Based on some of the available technical specifications of the ITER-TFC magnet design, various design parameters are taken and treated to determine the values used in the present numerical calculation.

Table 6: ITER-TFC technical specifications. Data publicly available, that considers the values as of now, with a TFC coil made of LTS conductors.

ITER-TFC magnet system stored energy	41 [GJ]
Operating Current	68 [kA]
Double Pancake (DP) coils	5 DP coils + 2 side DP coil
Conductor Length for DP coil	760 [m]

We know that the stored magnetic energy in a coil is $\frac{1}{2}LI^2$, and that the stored energy scales with the square of turns $E \propto N^2$. Then dividing the total energy by one of the 18 TFC, and scaling with the turns factor, assuming that each DP is one turn (averaging for $N = 7$ turns) we determine the self-inductance value of one DP coil, with an operational current of $I = 68$ kA, as:

$$E = \frac{\frac{41[GJ]}{18}}{N^2} = 46 \text{ [MJ]}$$

$$L = \frac{2E}{I^2} = 20 \text{ [mH]}$$

The conductor length is used for the calculation of the superconducting resistance as of the Power Law (Equation 4). A 20 HTS tapes stack is considered, to distribute the separation between HTS tapes for a 5 HTS tapes model, so the length and inductance variation per HTS tape is proportionally adjusted. The critical current is considered as constant, 20% higher than the value of the operating current.

Table 7: ITER-TFC DP calculation parameters for HTS. Estimations are done based on the ITER-TFC available data, to have values of all the required parameters to perform a numerical calculation.

Self-inductance	20 [mH]
Average HTS tape length	760 [m]
Operating current	68 [kA]
Total critical current	81.6 [kA]

7.1.1 Fast ramp-rate

A concern for large HTS magnets is that, as the self-inductance of HTS tapes and the inductance difference between them both increase, it may become detrimental for stable operation. Similarly, as with the previous simulations, a trapezoidal input current is used as a test scenario to explore what happens on the ITER-TFC DP magnet.

Under a fast ramp rate, the innermost strands or HTS tapes in a coiled cable, having less resistance and inductance, can start conducting the current initially during the ramp-up phase. Then, the current in the outer strands start to catch up afterwards, given the mutual inductance and circulation currents balancing the current distribution. Eventually, all HTS tapes have an almost same (but not precisely equal given the different length of the filaments) DC current share.

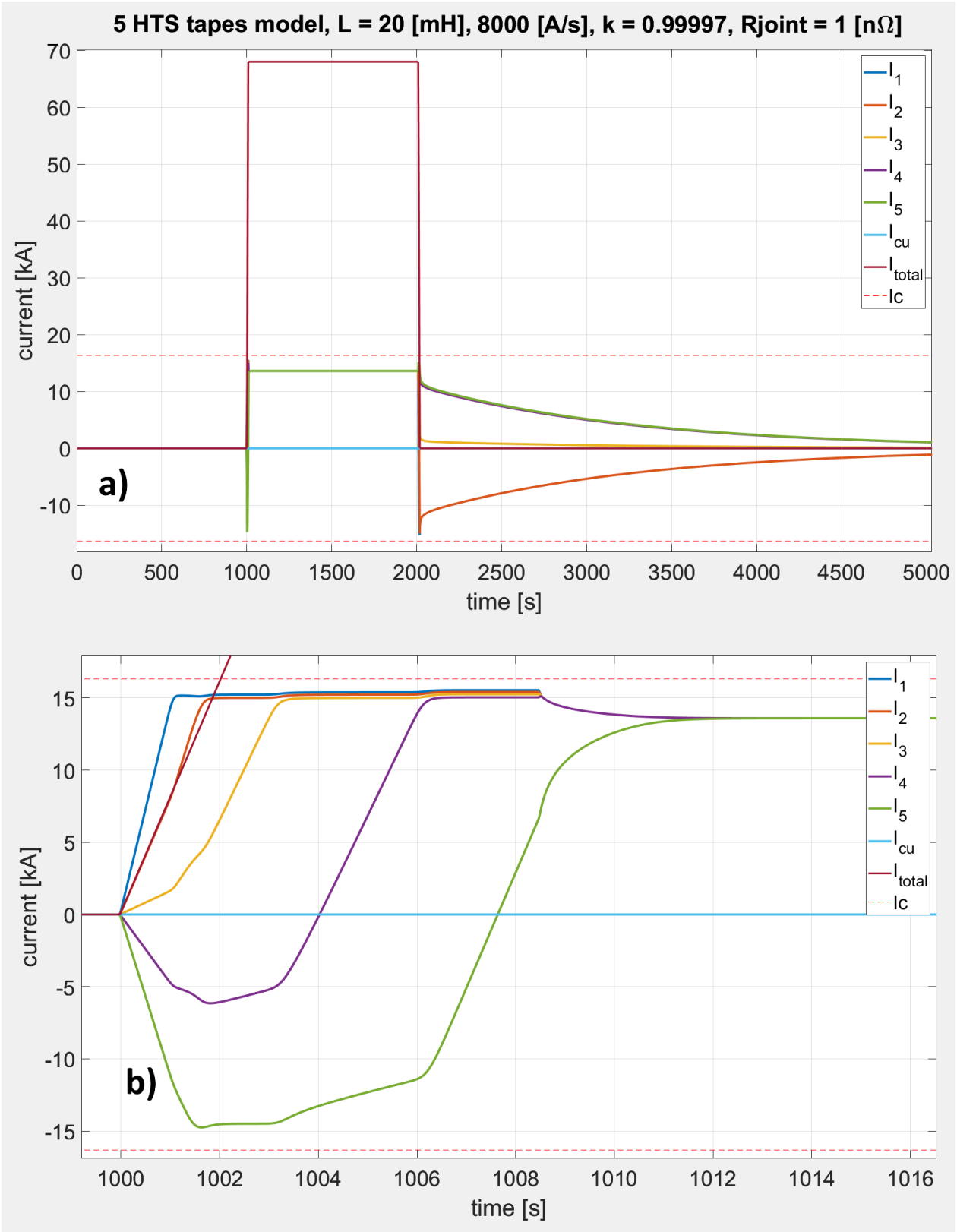

Figure 92: ITER-TFC DP simulation for 5 HTS tapes, trapezoidal current of 68 [kA] and 8000 [A/s]. In a) the overall current distribution is shown. In b) there is a zoom of the ramp-up phase, where the lower impedance branch reaches 95% of I_c.

7.1.2 Slow ramp-rate

Note that testing the behavior under trapezoidal input current, is to estimate if such large magnet can be charged and reach nominal current without quenching.

However, in reality, there is no need to charge to such fast ramp rate a DC operated HTS magnet. For large LTS magnets is customary to charge them within several hours, precisely to ensure that the nominal current is reached stably without risking a premature quench.

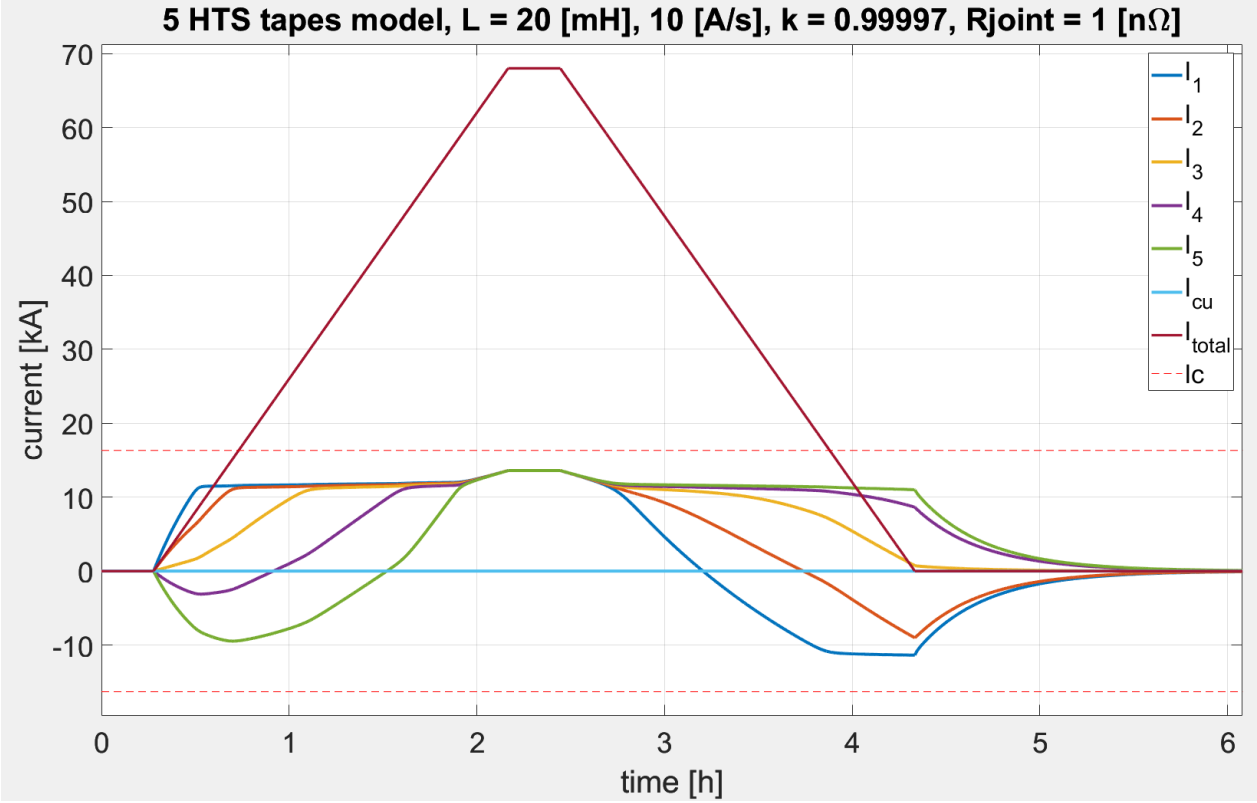

Figure 93: ITER TFC DP simulation for 5 HTS tapes, trapezoidal current of 68 [kA] and 10 [A/s]. The currents per branch have a large window margin from the critical current, and gradually stabilize on the flat-top section of the input current.

A slow charging of the same magnet is shown in Figure 93. There is a larger margin of the current in each branch compared to the critical current. As such current can redistribute within the strands with enough margin as to make less likely a quench of any HTS tape.

7.2 Contact Resistance and longitudinal subdivision

In the present calculation it is assumed that the circulation currents only return through current lead. This is a simplification, in reality, if contact resistance between HTS tapes has a low enough value compared to the joint resistance, circulation currents may return inside the cable, and not only in the current lead section.

Hence, the path where the circulation currents return depends on the ratio between longitudinal and contact resistance, as well as the value of the joint resistance. For long cables,

contact area between HTS tapes increases, and may account for a higher ratio of current circulating inside the cable, compared with shorter cables.

Further subdivision along the longitude of the cable, to account the contact resistance between HTS tapes, may give a better picture of current distribution, and whether the current still returns mostly in the current lead, or a significant fraction also returns inside the cable. The numerical calculation done for the short-straight HTS cable assume a constant contact resistance between HTS tapes along the length of the cable, yet variation in the contact resistance may enhance circulation currents in localized regions inside a cable.

It is worth pointing out that adding contact resistance into the numerical model implies additional sources of joule heating, as they are resistive paths where current may flow, and add up to the total ohmic losses produced. Nevertheless, it may be desirable that the contact resistance is also as low as possible in a HTS cable, which may allow current redistribution in case the superconducting state is reduced or lost somewhere, while keeping the ohmic losses low and use more effectively the stabilizer as a whole.

Building on a similar circuit configuration as shown in the RL model from Figure 75, Figure 94 shows an updated configuration that could be explored in the future, by adding subdivisions in the longitudinal direction of the cable. Joint resistance in the current lead, contact resistance by the subdivision, and inductance terms may allow to give a more detailed description of the current in a high-current coiled simple-stacking HTS cable.

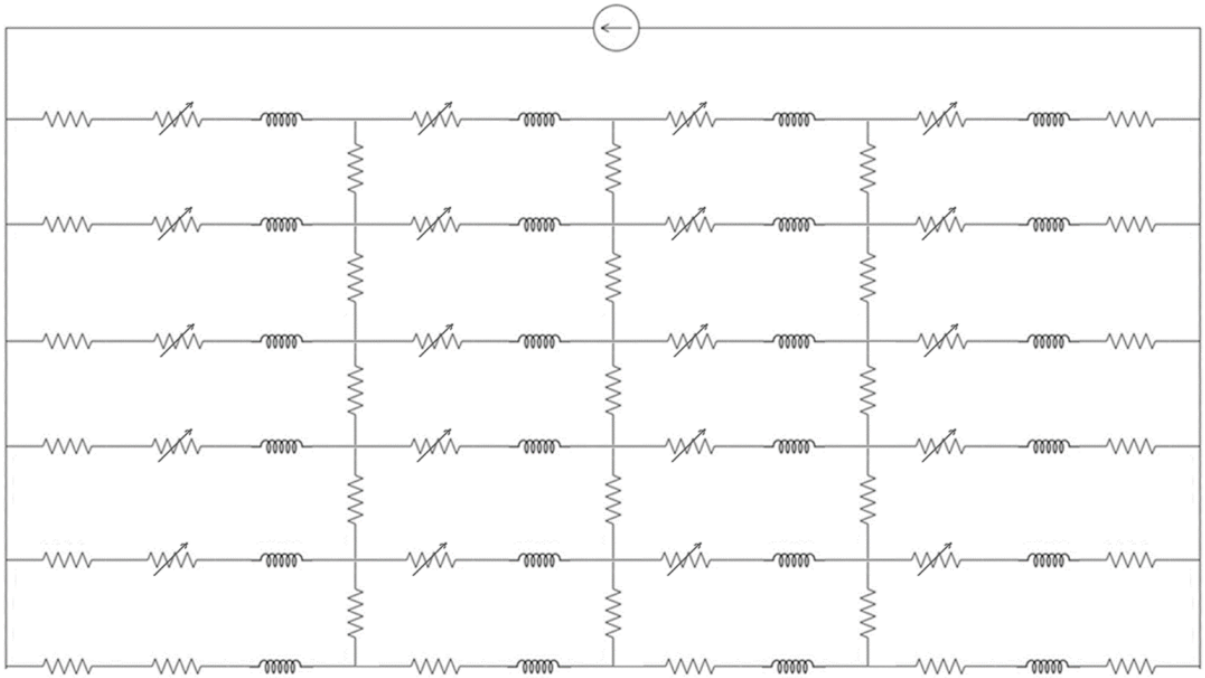

Figure 94: LR circuit model for current distribution in a coiled simple-stacking configuration, accounting joint resistance, internal contact resistance between HTS tapes, and inductance effects. Labels are omitted, as comparison from the single longitudinal inductance case.

7.3 Mutual Inductance and Coupling Factor

Coupling factor between filaments may slightly change in real cables wound in a coil shape, compared to a purely geometrical value. Ferromagnetic structures and different materials that surround the HTS tapes, imply slight changes of magnetic permeability throughout space. This is the case of CICC and large magnets in general.

Let us look the case of the 20-kA-class STARS conductor experiment. The stainless-steel jacket surrounds the HTS tapes along their total length, defining in the three dimensional space a region with different magnetic permeability than that of vacuum, which may slightly modify how the magnetic field lines between two coils are set into the three dimensional space around.

Also, a number of mechanical structures made of SS304 stainless steel, steel alloys and other materials, are present in the sample. These include the outer steel ring that serve as mechanical support, the long screws that support the weight of the sample, bolts in multiple locations that hold pieces in place, steel plates in the current lead rectangular piece, pipes for coolant flow, and semicircular steel plates partially covering the inner cross section of the coil. Additionally, a copper tube in a parallel path to the turns of the coil was used for coolant flow, in contact with copper blocks serving as heat sink for conduction cooling.

Then, when a current is fed into the sample, a magnetic field is produced that interacts with all these materials. In stainless steel structures there may be hysteresis losses by the changing magnetic field and how it interacts with the lattice of the material, while in copper structures there may be induced eddy currents that then decay without directly interacting with the HTS tapes inside the cable itself.

These effects may be not so significant at low-frequency current applications. Still, overall, these energy losses may be understood as a power loss, and it is useful to make an analogy as if the HTS tapes were the coils of a transformer. A small part of the power that could be transferred from one HTS tape to the other, gets instead lost into surrounding materials, which can be then translated as effectively reducing the coupling factor between them.

Figure 95 shows pictures of neodymium magnets attached to some of the stainless steel structures present in the 20-kA-class STARS. For the purpose of this discussion, these energy losses may have a slight effect into the coupling and current distribution in the HTS tapes, which experimentally can be observed as changes in the overall decay time. It needs further analysis to clarify for real conductors with a stainless steel jacket, whether a slight change in the coupling factor may significantly modify the current distribution, taking into account the role of the joint resistance in suppressing the circulation currents.

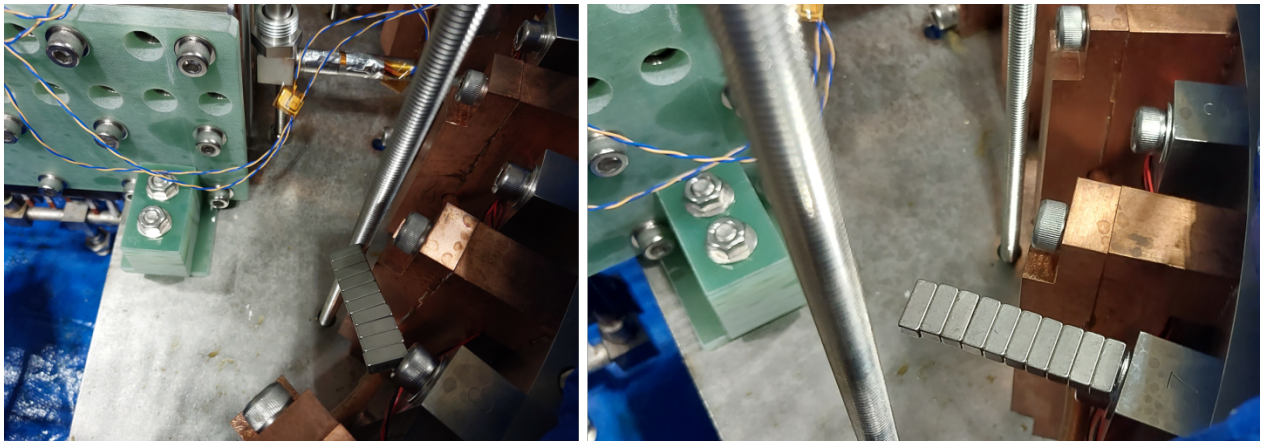

Figure 95: Confirmation of slight ferromagnetic parts in 20-kA-class STARS. The steel conduit and supporting mechanical structures are made with SS304 and other steel alloys, which may slightly affect the direction of magnetic field line, while producing eddy currents and hysteresis losses, that effectively reduce the coupling factor between HTS tapes in the cable.

Regarding the constant-temperature numerical calculations for the current distribution, specifically for the RL circuit model, the mutual inductance among HTS tapes is defined as function of the coupling factor, according to Equation 6.

On the "geometric" coupling factor case, the coupling factor depends on the area ratio between the radius defined by the HTS tapes along the solenoid defined, as the distance to its central axis, and as such it changes for each combination of mutual inductance among two given HTS tapes.

For the "reduced" coupling factor case, the achieved match of the residual magnetic field decay is by setting a single coupling factor value for all combinations of mutual inductance among HTS tapes. Note that the mutual inductance also depends on the values of the self-inductance of two given HTS tapes.

Despite this difference between the "geometric" coupling factor with multiple values, and for the "reduced" coupling factor case with a single value, the mutual inductance may not significantly deviate given the scale between the radius of the coil itself and the thickness of the HTS tapes.

For the 20-kA-class STARS and L-RAISER solenoids, the radius of the innermost REBCO tape is much larger than the separation between the superconducting layers of e.g 2 contiguous tapes (100 mm $>>$ 100 μm). The radius ratio then becomes more closer to unity at increasing coil radius, hence the variation of the coupling factor between different REBCO tapes combinations becomes lower as the radius of the coil increases.

Nonetheless, the present assumptions for the coupling factor are a simplification, given the amount of unknown factors at hand, which may not deviate much given the closeness of the HTS tapes, forming paths of parallel solenoids with the same number of turns.

Still, with a more detailed analysis and calculation of mutual inductance, based on the magnetic permeability changes throughout space given the different materials, a more accurate description of the current distribution may be available.

7.4 Critical current in numerical calculation

For the coiled samples, in the case of 20-kA-class STARS the total critical current was calculated to be around 54 kA (or 10.8 kA per HTS tape in the 5 HTS tapes model). For L-RAISER this was defined to be 600 A.

The calculations done by considering a changing critical current, were to observe the effect in the waveforms of the current in each HTS tape, to confirm if significant difference may happen for either critical current assumption.

While the waveforms may change noticeably with a time-changing critical current, a similar trend to the constant critical current assumption is observed. If the current in a HTS tape is close to the critical current threshold, the resistance in that branch increases and decay becomes locally faster, while having a wider critical current margin makes the decay last for longer.

Noticeably, the overall decay time of circulation currents after the current ramp-down remains roughly the same, and the currents follow in parallel the path of the critical current threshold, both if the critical current is constant or not.

7.5 Magnetic Field Modelling

By tracing the filaments that each HTS tape defines, (with their three dimensional coordinates, as shown for the analysis of each coil explored within this project), it suggests for a Biot-Savart calculation, to reproduce the magnetic field produced by the current waveforms obtained from the electric circuit numerical calculation.

While available, let us recall that for a large-current superconducting cable with a stainless steel jacket or otherwise large coil, multitude of materials are present around the filaments, which may slightly deviate the direction of magnetic field line depending on their magnetic permeability. As such, a numerical calculation with Finite Element Method (FEM) or similar approaches may give a more accurate reproduction of the three dimensional magnetic field distribution.

As a preliminary calculation, taking the case of the 20-kA-class STARS conductor, and using the waveforms for the current distribution obtained from Figure 80, a Biot-Savart three dimensional magnetic field calculation is done, shown in Figure 96. The aim is to confirm the traceability of the magnetic field decay, as what can be observed from the current decay from each HTS tape.

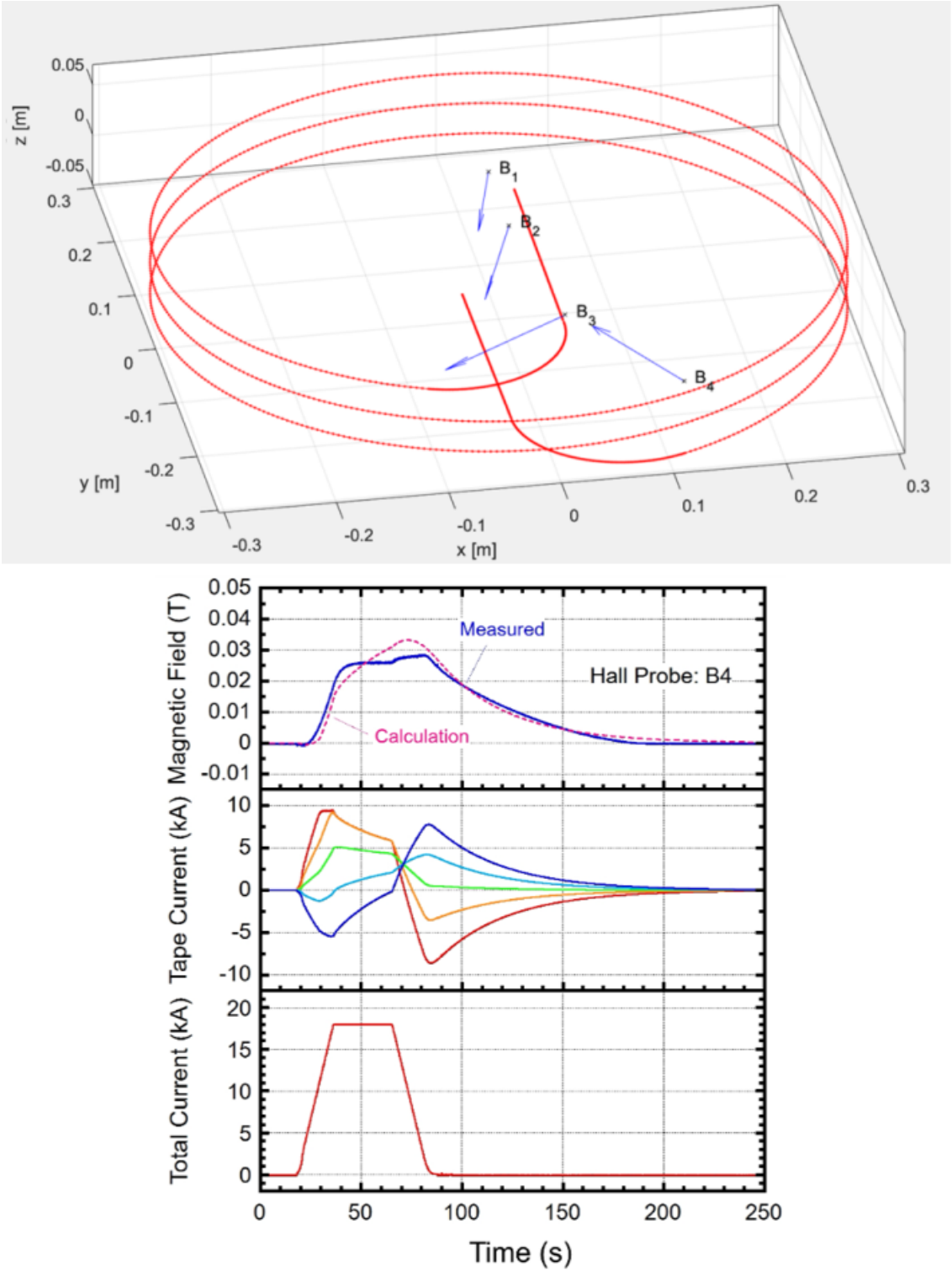

Figure 96: Biot-Savart preliminary 3D calculation for 20-kA-class STARS conductor, with a 5 HTS tapes model. Top: Tracing of filaments for the 6 m length of the HTS tapes, indicating direction of magnetic fields with current distribution from Figure 80. Bottom: Comparison for experimental (green line) and calculation (yellow line) in sensors B3 and B4, where accurate positioning and deviated magnetic field lines by other materials might affect matching.

During the development of the three dimensional Biot-Savart calculation, it was noticed that accurate positioning of calculation points is also necessary, which may make the magnetic field decay less visible with a different orientation in space of the magnetic sensor.

However, a possible limitation is that the computed currents assume that the recirculation only occurs in the current lead section. In reality, circulation currents in the experiment may have occurred in the inner region of the HTS tapes as well via the contact resistance, and even more, contact resistance may vary along the longitude of the cable.

Depending where the currents recirculate and return, and to which rate, the situation changes. If circulation currents mostly return at the current lead, the magnetic field calculation could make a closer match, but if there are significant fractions also returning via the contact resistance, this changes the overall current distribution in the three dimensional space. So in order to have a better reproduction of the magnetic field decay via a numerical calculation, an accurate description of the currents is needed, as mentioned in the Contact Resistance segment (subsection 7.2) of this Discussion chapter.

7.6 Scalability for large simple-stacking HTS conductor magnets

Coming back to the research question:

Can a simple-stacking large-current HTS cable, operate stably in a coil shape for DC current, when inductance variation among the tapes is present?

Let us have some concluding remarks.

The simple-stacking HTS experiments so far confirm stable operation with fast ramp rates, for trapezoidal input current or DC current. While stable operation was achieved, it remains unclear how close or far the HTS conductor experiments were to an unstable condition.

The 1.3 m HTS cable experiment showed that current transfer between the REBCO tapes is available. When any REBCO tapes starts developing a higher flux-flow resistance due to a large current in it, current transfer occurs to other REBCO tapes via the contact resistance.

Additional sensoring, specifically for the 20-kA-class STARS could provide extra information of the conditions inside the cable in high-current and high-field conditions, such as internal voltage taps and temperature sensors. Being a conductor with an internal electrical insulation and stainless steel jacket, access to inner sections is challenging and may have compromised mechanical robustness or electrical insulation, reason for which it was not pursued for the current experimental phases.

The L-RAISER experiment gave, along with the numerical calculations, gave further insights regarding the current distribution for the simple-stacking configuration. Results indicate that inductance variation increase may not be a prohibitive factor for scaling to larger magnets, as current in any HTS tape is limited by the critical current, and current transfer may occur via the contact resistance while the mutual inductance aids the power transfer among the HTS tapes when the conductor is in a coil shape.

The experimental results of the three HTS conductor experiments rely on the fact that cooling power may have been sufficient for all of them, to operate stably under the conditions tested. Especially for larger magnets operating at high current, if operating close to the critical current threshold, could a thermal runaway occur?

Thanks to the higher heat capacity available by operating at 20 K with HTS, although temperature rise may be lower than LTS for the same energy input, heat generation can also be localized. Then, the maximum temperature that materials reach also depends on how fast the generated heat can propagate throughout the material, and eventually be exhausted by the cooling system. Then local damage by overheating is a possibility.

For the ITER-TFC scenario, and any fusion magnet, the ohmic losses produced during operation are one of a few sources of heating, even if these losses are relatively low in a DC magnet compared to a magnet with AC operation.

Additional heat disturbances include nuclear heating produced by the neutrons produced in the plasma, possible plasma disruptions that may induce large currents in the magnet, and even changing currents in other magnets that may disturb the DC current. Towards the engineering side, point-wise defects for HTS tapes in the range of kilometers, could locally reduce the critical current and ohmic losses increase while the current redistribution around the defect takes place.

By having enough stabilizer in the HTS cable, the overall volume would be able to absorb all the heat disturbance sources, while being cooled and keeping the same operating temperature, to maintain the operation stable. An extensive thermal analysis is needed to further clarify if the present large-current simple-stacking cable designs can withstand all the expected heat disturbances, and remain stable under the operating conditions of a fusion reactor.

8 Summary

Magnets based on High-Temperature Superconductors (HTS) are a promising option for the next-generation fusion devices. HTS can achieve higher current density than Low-Temperature Superconductors (LTS), which results in a more compact magnet geometry, while increasing the magnetic field and improving the magnetic confinement performance of fusion plasmas.

Simple-stacking is the cable approach explored within this project, a mechanically strong configuration for HTS tapes which has an easy manufacturing process, and facilitates the fabrication of low resistance joints enabling modular coils. The higher cryogenic stability of HTS, due to the increased heat capacity when operating at a temperature of 20 K or higher, suggests that twisting and transposition may not be required for HTS magnets. Furthermore, experiments second that stable operation is available.

To clarify the feasibility of applying this configuration to large-current HTS magnets (due to the inductance difference formed between HTS tapes), it was explored the way current redistributes among HTS tapes, under input current conditions that would lead towards stable operation on DC current mode. As a magnet is gradually charged up to its operating DC current design, it is needed to be understood whether the current distribution among the strands can reach the operating current while remaining in the superconducting state.

Non-uniform current distribution (NUCD) and fast ramp rates are both causes of unstable operation in LTS magnets. It is then required to use twisting and transposition of superconducting strands, which facilitates a uniform current distribution among them. Slow ramp rates also facilitate the current to redistribute, so each superconducting strand carries a similar amount of current during the charging process of a magnet, defining the threshold for a Ramp Rate Limitation (RRL), above which the current handling capability of an LTS magnet deteriorates.

A circulation current can also develop among superconducting strands with a fast ramp rate, causing a large imbalance of current among them during a charging process. If the critical current of any strand is surpassed, a transition to the normal conduction state may occur, which may lead to a quench. So understanding the phenomenon in HTS contributes the clarification to which ramp rate threshold might be for stable operation of large-current HTS magnets based on simple-stacking.

At National Institute for Fusion Science (NIFS), large-current HTS cables have been explored, based on the simple-stacking concept from the beginning, especially for DC current operation and to be applied to the helical fusion reactor concept. Three experiments have been performed, one experiment for a straight cable, and two experiments for a coil shape. They confirm that simple-stacking HTS conductors have high stability for NUCD (despite the inductance difference formed with simple-stacking), and no RRL was found below a fast ramp-up rate of 2000 A/s. In parallel, constant-temperature numerical calculations were developed, to clarify the current distribution in both straight conductors (R circuit, accounting resistance) and coiled conductors (RL circuit, accounting resistance and inductance), which

consider the superconducting characteristics of HTS conductors.

The first experiment by T. Meulenbroeks et al. confirmed, for a short-straight cable of 1.3 m and 5 HTS tapes, stable operation under the worst-case scenario of NUCD, by feeding the current only through the topmost tape. A numerical calculation supported the experimental observation, that indicates a stepwise transfer of current between HTS tapes occurs while the critical current in each tape is being reached, and the process continues as the total input current increases.

The second experiment is the 20-kA-class STARS conductor, for a 6 m total length, solenoid coil shape with 3 turns and 600 mm in diameter, operating between 20 K and 40 K. The nominal current of 18 kA achieved with 1 kA/s ramp up and down tests, confirmed stable operation and no discernible degradation for up to 200 cycles in total and a maximum of 2 kA/s was attained with no premature quench due to a RRL. The observation of a residual magnetic field after the input current became zero confirmed the formation of circulation currents, and by magnetic measurements by sensors at different positions of the coiled sample, it was clarified the return path of the circulation currents being higher near the current lead region.

The third experiment is the L-RAISER solenoid designed and developed as part of this project. It has a length of 10 m, using 5 REBCO tapes of 4 mm width on a simple-stacking configuration. By decreasing the diameter of the solenoid and increasing the number of turns, a higher self-inductance per HTS tape stack was obtained, compared to the 20-kA-class STARS conductor. L-RAISER was tested both under the worst-case scenario of current feeding and uniform current feeding. While the worst-case scenario of current feeding showed that current redistribution was available, uniform current feeding allowed stable operation up to 2 kA/s and high load factor (ratio between operating current and total critical current).

The constant-temperature (RL circuit) numerical calculations were done for both the 20-kA-class STARS and L-RAISER coiled samples, adapted for a 5 HTS tapes model in both cases, where a similar decay time was obtained to the values observed experimentally. An additional numerical calculation was done, extrapolating for a bigger HTS magnet for DC operation, choosing as analysis case a double-pancake (DP) inside ITER Toroidal Field Coil (TFC), under the same 5 HTS tapes model. The inductance and conductor longitude parameters were estimated, based on the current design of ITER TFC DP with LTS materials, and switching the conditions to a simple-stacking case with HTS materials.

The result indicates that for these ITER TFC DP coil parameters, a ramp-rate of a few kA/s (<8 kA/s) may be available, while reaching at that threshold "only" 95% of the critical current threshold in the innermost HTS tape. Then, this 8 kA/s threshold value is deemed a first estimate of what a RRL may be for a large HTS DC magnet based on simple-stacking. In reality, a magnet of such dimensions would be charged at a slow ramp-rate (e.g. 10 A/s or less) and as such, operation would be expected more stable.

As detailed thermal analysis for simple-stacking conductors remains as future work, a zero-dimensional thermal estimation was done for the 20-kA-class conductor. It was determined that under the current distribution from the numerical calculation at 1 kA/s, a marginal

temperature rise may occur (<0.1 K for the stabilizer available volume), even with no cooling during the process.

By scanning different combinations of variables in a calculation, it may be possible to keep estimating quantitatively the operation response of bigger coils. Related to experiments, a coil with small inductance and fast ramp rate, as the two coiled experiments described before, may provide a similar circulation current fraction than a big inductance coil with a slow ramp rate, and give a comparable performance for stable operation.

Experimental results so far suggest that there is further room for constructing longer length high-current HTS conductors, with similar stable operation. Numerical calculations suggest that even if inductance variation if present among the HTS tapes, stable operation is available, and the high cryogenic stability of HTS operating (available by operating at e.g. 20 K) causes negligible temperature rise, that may be exhausted by the cooling system. Detailed thermal analysis remains as future work, to further explore how much the critical current and RRL may be reduced, depending on the geometry, heat propagation and heat exhaust conditions for a large fusion-size HTS magnet based on simple-stacking.

Acknowledgements

These lines are to thank all the people that supported me along the road in all sorts of ways, during the study period and my stay at NIFS. Hoping that I managed to recollect my memories to mention every person.

To my family, for always supporting my study goals, and always be there to talk independently from where we are. Gracias.

To Nagato Yanagi for the opportunity to work into the applied superconductivity group at NIFS. For the guidance and patience during my study period, as well as considering my ideas along the road which led to fruitful discussions and experiments. I'm glad to have being able to learn and contribute into these superconductivity developments.

To Yoshiro Narushima for the willingness to listen and discuss about all sort of ideas and topics, support along the PhD project, the always easygoing attitude, and conversations in Spanish when there was the chance.

For the useful input and discussions that led to additions, corrections and improvements for this work. To Naoki Hirano, So Noguchi and Satoshi Ito.

For the development and progress of this project, I thank the contributions of many people, that by collaboration and/or discussion supported the fulfillment of both experiments and numerical calculations.

To Hirotaka Chikaraishi for the helpful conversation towards equation modelling; to Tetsuhiro Obana, Shinsaku Imagawa and Kazuya Takahata for the additional comments to add into the discussion section. To Tomosumi Baba for the support for the 20-kA-class STARS conductor, and in the assembly of L-RAISER. To Tim Meulenbroeks and Maria Morbey; whose contribution work for the straight HTS cable led to the explorations within this project. To Enghryt Rattanawongnara for the inductance measurement ideas, and frequent engineering conversations that often gave me insights. To Shinji Hamaguchi and Yuta Onodera, for their kindness and support along the experimental work. To Miguel Lindero for the conversations about superconductivity developments.

To Roger Jaspers from TU/e, Frederic Trillaud and Julio Herrera from UNAM, and Kenichi Nagaoka from NIFS. Thank you for initially supporting my plan of pursuing the PhD studies.

To the Research Assistant program from NIFS and the Yukwai Scholarship; providing the funding during the PhD studies period.

To the members of the NBI group, with whom we collaborated back in time when I did an internship some years back, and kindness throughout these years: Masaki Osakabe, Katsuyoshi Tsumori, Masashi Kisaki, Yasuaki Haba and Haruhisa Nakano.

To the NIFS community with whom I shared conversations both for technical and casual matters. To the people from the English Lunch and Library Cafe, for the interesting con-

versations in all sorts of topics. To Byron Peterson, for promoting the cohesion of both Japanese and international community in NIFS, as the good times ranging from ski to dinner or karaoke, along my former and current stay. To Katsumi Ida for the kindness along the ski trip; Stephen Carr and the interesting society conversations; Kazuko Mizuno, Riho Kameyama and Ayami Kimata for kindness and introducing me to different Japanese snacks; Akiko Miyashita for the Spanish conversations; Hiroshi Kasahara for CAE software support.

To NIFS staff, that constantly supported me with administration matters, thank you for your kindness always, and taking the time to explain me processes and paperwork when it was due. To Takako Shibata, Ai Seta, Sanae Kawai, Tomoko Matsuzaki, Ryotaro Yamaji, Keiko Kuriki and Satoru Sakakibara for the support along these years and kindness always.

To Nakamura-sensei and Hiro-sensei, who went along into teaching me Japanese language during my time in NIFS and Tajimi. でもまだです . Still got lots to learn.

To friends and people from different nationalities I met along the road during these study years. It's been a pleasure to exchange ideas and share a friendship with all of you. I deeply appreciate it.

To Eri Takada for the unconditional support, good times and teaching me all sorts of things about Japan. To Hikaru Kumai who helped me settle living matters in Japan, and nice conversations and friendship along the way; as well as Daigo Kanamori when moving out. To Priti, Shivam Gupta, Li Enhao, Lin Keren and again Enghryt; for the good times and casual conversations that made every working day a bit more amusing. To Tetsuto Hara for the nice discussions in technical and societal matters, and support on dropping me closer to home. To Nagaaki Kambara and Yuuki Noguchi, who were supportive and took us to discover interesting places around Chubu region of Japan, both with snow and sea landscapes, as well as the ocassional random paperwork. To Tang Ning, Wang Na, JJ Simons and Liu Bing for all the nice trips, good times and conversations that we shared along, may we keep contact. To Tomoki Shimamoto, Yuto Toda, Yuuya Suzuki, Hiroki Yata, Toyo Yamashita and Tsukasa Sugiyama for the good times at dinners and board games; Tetsuhiro Nasu and the interesting music event; Joseph Li, Shu Nishimoto, Liao Longyong, Paenthong Worathat, Irino, Bhumika and Swati for the kindness.

To the international community who visited NIFS at different points in time, from which a fresh perspective and friendliness was always welcome and appreciated. To Alexander Liptak, Maikel Morren and Stanley for the trips and experiences shared; Victoria Haak and the tea break conversations; Gabriele Partessoti, Isabella Mario and Basile for the coffee breaks and nice conversations on that Kyoto trip; Jaime for the easygoing attitude and friendliness; Nerea Panadero for the kindness. May we meet again sometime somewhere.

And to every person that I may have missed, who lent me a friendly word or gesture at any given point.

では、みんなさん、ありがとうございました
Muchas gracias. Thank you very much.
Diego

Appendix A: Constant Temperature RL Model

As introduced in the main text, a resistance-inductance (RL) circuit model is defined, accounting the slightly different values present among stacked HTS tapes wound in a coil shape, for the simple-stacking configuration. The model is derived from Kirchhoff's Voltage and Current Laws (KVL, KCL).

This model assumes that the temperature remains constant during the process, while the current in each HTS tape is limited by the critical current of the HTS superconducting layer. Figure 97 shows the RL circuit for the case of 5 HTS tapes:

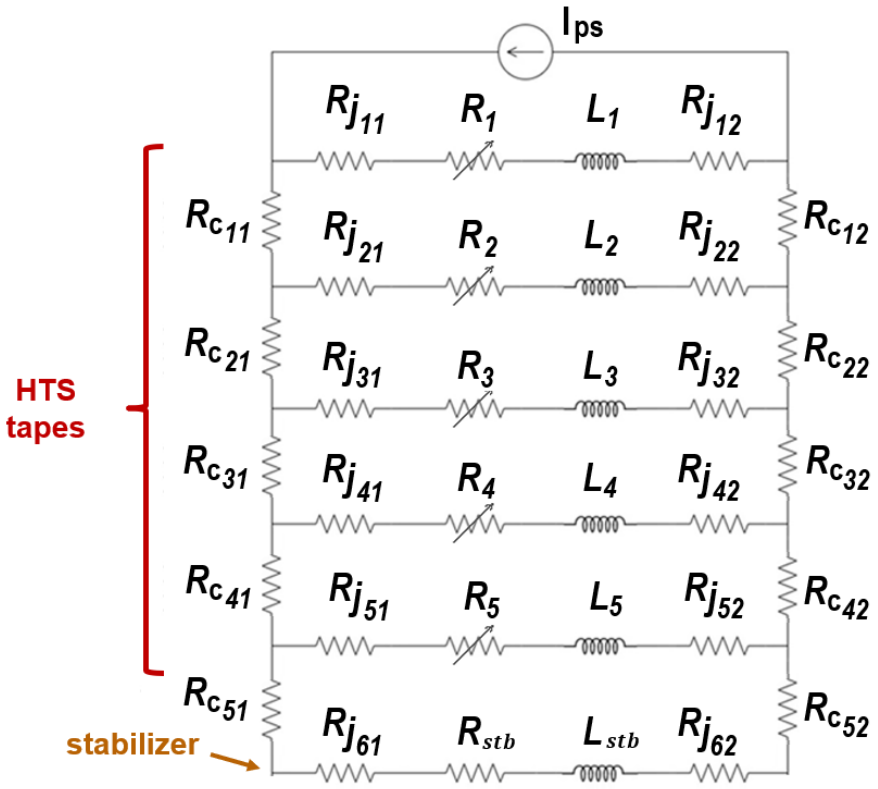

Figure 97: Complete RL circuit model for 5 HTS tapes, accounting length and inductance variation of the strands. The joint resistances (R_j) and contact resistances (R_c) imply a worst-case scenario of current feeding. By setting all R_c equal to zero, it corresponds to the uniform current feeding condition from Figure 75.

This circuit form considers also contact resistances (R_c). Given there is only "one" division longitudinally for each row in the circuit, it implies a worst-case scenario of current feeding, done only through the edge of one HTS tape. Accounting inner contact resistances requires a subdivision longitudinally, as mentioned in the Discussion section.

By setting all R_c equal to zero, the model corresponds to the uniform current feeding condition from Figure 75. The general form for a m number of HTS tapes, with stabilizer and contact resistance is then:

$$
\begin{cases}
I_1(R_1+\sum_{n=1}^{2}Rj_{1n})-I_2(R_2+\sum_{n=1}^{2}Rj_{2n}+\sum_{n=1}^{2}Rc_{1n})-(\sum_{n=3}^{m}I_n)(\sum_{n=1}^{2}Rc_{1n})+\sum_{n=1}^{m+1}(M_{1n}-M_{2n})\dot{I}_n=0 \\
\qquad\qquad\qquad\qquad\qquad\qquad\qquad\qquad\vdots \\
I_{m-2}(R_{m-2}+\sum_{n=1}^{2}Rj_{(m-2)n})-I_{m-1}(R_{m-1}+\sum_{n=1}^{2}Rj_{(m-1)n}+\sum_{n=1}^{2}Rc_{(m-2)n}) \\
\qquad\qquad -(\sum_{n=m+1}^{m+1}I_n)(\sum_{n=1}^{2}Rc_{(m-2)n})+\sum_{n=1}^{m+1}(M_{(m-2)n}-M_{(m-1)n})\dot{I}_n=0 \\
I_{m-1}(R_{m-1}+\sum_{n=1}^{2}Rj_{(m-1)n})-I_m(R_m+\sum_{n=1}^{2}Rj_{mn}+\sum_{n=1}^{2}Rc_{(m-1)n})+\sum_{n=1}^{m+1}(M_{(m-1)n}-M_{mn})\dot{I}_n=0 \\
I_{ps}-(\sum_{n=1}^{m+1}I_n)=0
\end{cases}
\tag{14}
$$

$$
M=k\sqrt{L_iL_j},\quad k=A_i/A_j,\quad A_i>A_j \tag{15}
$$

where:

I_{ps}	Input current
I_1-I_m	Current in each superconducting branch
I_{m+1}	Current in stabilizer branch
R_1-R_m	Resistance of superconducting layer of HTS tape (power law)
R_{m+1}	Stabilizer resistance
R_j	Joint resistance between HTS tapes
R_c	Contact resistance (in non-uniform current feeding case)
M_{ii}	Self-inductance of the branch
M_{ij} $(i \neq j)$	Mutual inductance between branches
k	Coupling factor (area ratio between strands)

The power law equation for the superconducting resistance calculation is:

$$
R_{sc}=\frac{E_c}{I_c}\Delta x(\frac{I_x}{I_c})^n \tag{16}
$$

where:

E_c	Critical electric field criterion ($1x10^{-6}[V/cm]$)
Δx	Length of the superconducting branch
I_x	Current in the superconducting branch
I_c	Critical current
n	n-value

References

[1] Giuliano Buceti. "Sustainable power density in electricity generation". In: *Management of Environmental Quality: An International Journal* 25.1 (2014), pp. 5–18. DOI: 10.1108/MEQ-05-2013-0047. eprint: https://doi.org/10.1108/MEQ-05-2013-0047. URL: https://doi.org/10.1108/MEQ-05-2013-0047.

[2] Ioannis N. Kessides. "Nuclear Power and Sustainable Energy Policy: Promises and Perils". In: *The World Bank Research Observer* 25.2 (2010), pp. 323–362. DOI: 10.1093/wbro/lkp010. eprint: /oup/backfile/content_public/journal/wbro/25/2/10.1093/wbro/lkp010/2/lkp010.pdf. URL: http://dx.doi.org/10.1093/wbro/lkp010.

[3] *United Nations Development Program: The 17 Sustainable Development Goals (SDG)*. 2024. URL: https://sdgs.un.org/goals.

[4] Zion Lights. "The (Missing) Role of Nuclear Energy in the Sustainable Development Goals". In: *Journal of the European Institut for Multidisciplinary Studies on Human Rights Science* 3 (Mar. 2022). URL: https://knowmadinstitut.org/2022/03/the-missing-role-of-nuclear-energy-in-the-sustainable-development-goals.

[5] Marina Dabetic Ex Filipovic, Dejana Popovic and Slavko Nešić. "The role of nuclear energy for sustainable development goals". In: June 2017. URL: https://www.researchgate.net/publication/314281780_The_role_of_nuclear_energy_for_sustainable_development_goals.

[6] Harikrishnan Tulsidas et al. "The Role of Nuclear Energy in Sustainable Development: Entry Pathways". In: (Feb. 2019). DOI: 10.13140/RG.2.2.30120.62723.

[7] International Atomic Energy Association. *Nuclear Power for Sustainable Development*. 2017. URL: https://www.iaea.org/sites/default/files/np-sustainable-development.pdf.

[8] International Atomic Energy Association. *Sustainable Development Goals (SDGs) at IAEA*. 2024. URL: https://www.iaea.org/about/overview/sustainable-development-goals.

[9] World Nuclear Association. *Nuclear's contribution to achieving the UN Sustainable Development Goals*. 2021. URL: https://www.world-nuclear.org/sustainable-development-goals-and-nuclear.aspx.

[10] United Nations: Climate Action. *The Paris Agreement*. 2024. URL: https://www.un.org/en/climatechange/paris-agreement.

[11] Akos Horvath and Elisabeth Rachlew. "Nuclear power in the 21st century: Challenges and possibilities". In: *Ambio* 45.1 (Jan. 2016), pp. 38–49. ISSN: 1654-7209. DOI: 10.1007/s13280-015-0732-y. URL: https://doi.org/10.1007/s13280-015-0732-y.

[12] Alistair F. Holdsworth et al. "Spent Nuclear Fuel;Waste or Resource? The Potential of Strategic Materials Recovery during Recycle for Sustainability and Advanced Waste Management". In: *Waste* 1.1 (2023), pp. 249–263. ISSN: 2813-0391. DOI: 10.3390/waste1010016. URL: https://www.mdpi.com/2813-0391/1/1/16.

[13] Bruno Merk et al. "An innovative way of thinking nuclear waste management - Neutron physics of a reactor directly operating on SNF". en. In: *PLoS One* 12.7 (July 2017). URL: https://www.ncbi.nlm.nih.gov/pmc/articles/PMC5531547/.

[14] Rajesh Kumar Jyothi et al. "An overview of thorium as a prospective natural resource for future energy". In: *Frontiers in Energy Research* 11 (2023). ISSN: 2296-598X. DOI: 10.3389/fenrg.2023.1132611. URL: https://www.frontiersin.org/articles/10.3389/fenrg.2023.1132611.

[15] M. Mitchell Waldrop. *Pursuing fusion power*. Nov. 2023. URL: https://knowablemagazine.org/content/article/physical-world/2023/the-challenge-of-fusion-power.

[16] Franco Julio Mangiarotti. *Design of Demountable Toroidal Field Coils with REBCO Superconductors for a Fusion Reactor*. Massachusetts Institute of Technology, 2016.

[17] Jeffrey P Freidberg. *Plasma Physics and Fusion Energy*. Cambridge University Press, 2008.

[18] Peter Dunn. *On the right path to fusion energy*. URL: https://www.psfc.mit.edu/news/2018/on-the-right-path-to-fusion-energy.

[19] Thomas Griffiths et al. "The commercialisation of fusion for the energy market: a review of socio-economic studies". In: *Progress in Energy* 4.4 (Aug. 2022), p. 042008. DOI: 10.1088/2516-1083/ac84bf. URL: https://dx.doi.org/10.1088/2516-1083/ac84bf.

[20] N.J. Lopes Cardozo, A.G.G. Lange and G.J. Kramer. "Fusion : expensive and taking forever?" English. In: *Journal of Fusion Energy* 35.1 (Mar. 2016), pp. 94–101. ISSN: 0164-0313. DOI: 10.1007/s10894-015-0012-7.

[21] N.J. Lopes Cardozo. "Economic aspects of the deployment of fusion energy: The valley of death and the innovation cycle". English. In: *Philosophical Transactions of the Royal Society of London, Series A: Mathematical, Physical and Engineering Sciences* 377.2141 (Mar. 2019). ISSN: 1364-503X. DOI: 10.1098/rsta.2017.0444.

[22] Malcolm C. Handley, Daniel Slesinski and Scott C. Hsu. "Potential Early Markets for Fusion Energy". In: *Journal of Fusion Energy* 40.2 (July 2021), p. 18. ISSN: 1572-9591. DOI: 10.1007/s10894-021-00306-4. URL: https://doi.org/10.1007/s10894-021-00306-4.

[23] Hirotaka Chikaraishi et al. "Conceptual Design of Fusion Power Complex with Hydrogen Storage Function in Superconducting Magnet System". In: *Plasma and Fusion Research* 18 (2023), pp. 1205001–1205001. DOI: 10.1585/pfr.18.1205001.

[24] Ahmed I. Osman et al. "Hydrogen production, storage, utilisation and environmental impacts: a review". In: *Environmental Chemistry Letters* 20.1 (Feb. 2022), pp. 153–188. ISSN: 1610-3661. DOI: 10.1007/s10311-021-01322-8. URL: https://doi.org/10.1007/s10311-021-01322-8.

[25] *The Future of Hydrogen*. 2019. URL: https://www.iea.org/reports/the-future-of-hydrogen.

[26] *Global Hydrogen Review 2023*. 2023. URL: https://www.iea.org/reports/global-hydrogen-review-2023.

[27] Alexander Trattner, Manfred Klell and Fabian Radner. "Sustainable hydrogen society – Vision, findings and development of a hydrogen economy using the example of Austria". In: *International Journal of Hydrogen Energy* 47.4 (2022), pp. 2059–2079. ISSN: 0360-3199. DOI: https://doi.org/10.1016/j.ijhydene.2021.10.166. URL: https://www.sciencedirect.com/science/article/pii/S0360319921042233.

[28] Daqin Guan et al. "Hydrogen society: from present to future". In: *Energy Environ. Sci.* 16 (11 2023), pp. 4926–4943. DOI: 10.1039/D3EE02695G. URL: http://dx.doi.org/10.1039/D3EE02695G.

[29] *Fusion Energy: Potentially Transformative Technology Still Faces Fundamental Challenges*. 2023. URL: https://www.gao.gov/products/gao-23-105813.

[30] Brandon Sorbom. *High-temperature superconductors for fusion: Recent achievements and near-term challenges*. URL: https://suli.pppl.gov/2020/course/20200619_SULI_HTS_Sorbom_Final.pdf.

[31] International Atomic Energy Agency. *World Survey of Fusion Devices 2022*. International Atomic Energy Agency, 2023. ISBN: 9789201434227. URL: https://www.iaea.org/publications/15253/world-survey-of-fusion-devices-2022.

[32] Samuele Meschini et al. "Review of commercial nuclear fusion projects". In: *Frontiers in Energy Research* 11 (2023). ISSN: 2296-598X. DOI: 10.3389/fenrg.2023.1157394. URL: https://www.frontiersin.org/articles/10.3389/fenrg.2023.1157394.

[33] D. M. Ventura-Ovalle D. Hernández-Arriaga and M. Nieto-Pérez. "Design of the Toroidal Field Coil System for the TPM-1U Tokamak". In: *Fusion Science and Technology* 75.2 (2019), pp. 148–159. DOI: 10.1080/15361055.2018.1554390. eprint: https://doi.org/10.1080/15361055.2018.1554390. URL: https://doi.org/10.1080/15361055.2018.1554390.

[34] T.S. Lee et al. "Optimal design of a toroidal field magnet system and cost of electricity implications for a tokamak using high temperature superconductors". In: *Fusion Engineering and Design* 98-99 (2015). Proceedings of the 28th Symposium On Fusion Technology (SOFT-28), pp. 1072–1075. ISSN: 0920-3796. DOI: https://doi.org/10.1016/j.fusengdes.2015.06.125. URL: http://www.sciencedirect.com/science/article/pii/S0920379615301526.

[35] Yeekin Tsui, Elizabeth Surrey and Damian Hampshire. "Soldered joints—an essential component of demountable high temperature superconducting fusion magnets". In: *Superconductor Science and Technology* 29.7 (2016), p. 075005. URL: http://stacks.iop.org/0953-2048/29/i=7/a=075005.

[36] Hidetoshi Hashizume and Satoshi Ito. "Design prospect of remountable high-temperature superconducting magnet". In: *Fusion Engineering and Design* 89.9 (2014). Proceedings of the 11th International Symposium on Fusion Nuclear Technology-11 (ISFNT-11) Barcelona, Spain, 15-20 September, 2013, pp. 2241–2245. ISSN: 0920-3796. DOI: https://doi.org/10.1016/j.fusengdes.2013.12.014. URL: https://www.sciencedirect.com/science/article/pii/S092037961300728X.

[37] Miguel Lindero Hernández. "Design and construction of a circular emountable toroidal field coil prototype for the mexican tokamak TPM-1U". PhD thesis. 2022. 102 pp. URL: http://tesis.ipn.mx/handle/123456789/32051.

[38] F. J. Mangiarotti and J. V. Minervini. "Advances on the Design of Demountable Toroidal Field Coils With REBCO Superconductors for an ARIES-I Class Fusion Reactor". In: *IEEE Transactions on Applied Superconductivity* 25.3 (June 2015), pp. 1–5. ISSN: 1051-8223. DOI: 10.1109/TASC.2014.2379641.

[39] B.N. Sorbom et al. "ARC: A compact, high-field, fusion nuclear science facility and demonstration power plant with demountable magnets". In: *Fusion Engineering and Design* 100 (2015), pp. 378–405. ISSN: 0920-3796. DOI: https://doi.org/10.1016/j.fusengdes.2015.07.008. URL: http://www.sciencedirect.com/science/article/pii/S0920379615302337.

[40] Gourab Bansal et al. "High-Temperature Superconducting Coil Option for the LHD-Type Fusion Energy Reactor FFHR". In: *Plasma and Fusion Research* 3 (2008), S1049–S1049. DOI: 10.1585/pfr.3.S1049.

[41] Nagato YANAGI et al. "Progress in the Conceptual Design of the Helical Fusion Reactor FFHR-d1". In: *Journal of Fusion Energy* 38.1 (Oct. 2018), pp. 147–161. ISSN: 0164-0313. URL: https://cir.nii.ac.jp/crid/1050571948014334336.

[42] Satoshi Ito et al. "Mechanical and Electrical Characteristics of a Bridge-Type Mechanical Lap Joint of HTS STARS Conductors". In: *IEEE Transactions on Applied Superconductivity* 26.2 (2016), pp. 1–10. DOI: 10.1109/TASC.2016.2517197.

[43] Satoshi Ito et al. "Advanced high-temperature superconducting magnet for fusion reactors: Segment fabrication and joint technique". In: *Fusion Engineering and Design* 136 (2018). Special Issue: Proceedings of the 13th International Symposium on Fusion Nuclear Technology (ISFNT-13), pp. 239–246. ISSN: 0920-3796. DOI: https://doi.org/10.1016/j.fusengdes.2018.01.072. URL: https://www.sciencedirect.com/science/article/pii/S092037961830098X.

[44] Satoshi Ito et al. "Bridge-type mechanical lap joint of HTS STARS conductors using an integrated joint piece". In: *Fusion Engineering and Design* 146 (2019). SI:SOFT-30, pp. 590–593. ISSN: 0920-3796. DOI: https://doi.org/10.1016/j.fusengdes.2019.01.030. URL: https://www.sciencedirect.com/science/article/pii/S0920379619300390.

[45] N. Yanagi et al. "Magnet design with 100-kA HTS STARS conductors for the helical fusion reactor". In: *Cryogenics* 80 (2016). Special Issue on HTS Cooling 2015, pp. 243–249. ISSN: 0011-2275. DOI: https://doi.org/10.1016/j.cryogenics.2016.06.011. URL: https://www.sciencedirect.com/science/article/pii/S0011227516301485.

[46] CERN Large Hadron Collider Team. *LHC Machine Outreach: Superconducting cable*. URL: https://lhc-machine-outreach.web.cern.ch/components/cable.htm.

[47] Dirk van Delft and Peter Kes. "The discovery of superconductivity". In: *Physics Today* 63.9 (Sept. 2010), pp. 38–43. ISSN: 0031-9228. DOI: 10.1063/1.3490499. eprint: https://pubs.aip.org/physicstoday/article-pdf/63/9/38/9879861/38_1_online.pdf. URL: https://doi.org/10.1063/1.3490499.

[48] Simon Alastair Keys. *Temperature and strain scaling laws for the critical current density in Nb3Sn and Nb3Al conductors in high magnetic fields*. Durham University, 2001. URL: http://etheses.dur.ac.uk/3951/.

[49] Bryan Luther. *Superconductivity: Basic Properties*. http://faculty.cord.edu/luther/physics225/lectures/superconductors.pdf. (Accessed on 10/08/2018).

[50] P.H. Kes. "Electrodynamics of Superconductors: Flux Properties". In: *Encyclopedia of Materials: Science and Technology*. Ed. by K.H. Jürgen Buschow et al. Oxford: Elsevier, 2001, pp. 2535–2537. ISBN: 978-0-08-043152-9. DOI: https://doi.org/10.1016/B0-08-043152-6/00459-9. URL: http://www.sciencedirect.com/science/article/pii/B0080431526004599.

[51] M.N. Wilson. *Superconducting Magnets*. Monographs on cryogenics. Clarendon Press, 1983. ISBN: 9780198548102. URL: https://books.google.nl/books?id=AObvAAAAMAAJ.

[52] M. K. Wu et al. "Superconductivity at 93 K in a new mixed-phase Y-Ba-Cu-O compound system at ambient pressure". In: *Phys. Rev. Lett.* 58 (9 Mar. 1987), pp. 908–910. DOI: 10.1103/PhysRevLett.58.908. URL: https://link.aps.org/doi/10.1103/PhysRevLett.58.908.

[53] D.G. Schlom and J. Mannhart. "High-temperature Superconductors: Thin Films and Multilayers". In: *Encyclopedia of Materials: Science and Technology*. Ed. by K.H. Jürgen Buschow et al. Oxford: Elsevier, 2001, pp. 3806–3819. ISBN: 978-0-08-043152-9. DOI: https://doi.org/10.1016/B0-08-043152-6/00678-1. URL: http://www.sciencedirect.com/science/article/pii/B0080431526006781.

[54] J. C. Hernandez-Llambes and D. Hazelton. "Advantages of second-generation high temperature superconductors for pulsed power applications". In: *2009 IEEE Pulsed Power Conference*. June 2009, pp. 221–226. DOI: 10.1109/PPC.2009.5386312.

[55] Calvin C.T. Chow, Mark D. Ainslie and K.T. Chau. "High temperature superconducting rotating electrical machines: An overview". In: *Energy Reports* 9 (2023), pp. 1124–1156. ISSN: 2352-4847. DOI: https://doi.org/10.1016/j.egyr.2022.11.173. URL: https://www.sciencedirect.com/science/article/pii/S2352484722025628.

[56] Wafa Ali Soomro et al. "Advancements and Impediments in Applications of High-Temperature Superconducting Material". In: *2020 IEEE International Conference on Applied Superconductivity and Electromagnetic Devices (ASEMD)* (2020), pp. 1–4. URL: https://api.semanticscholar.org/CorpusID:229310218.

[57] Jianxun Jin et al. "Applied Superconductivity and Electromagnetic Devices - Principles and Current Exploration Highlights". In: *IEEE Transactions on Applied Superconductivity* 31.8 (2021), pp. 1–29. DOI: 10.1109/TASC.2021.3108740.

[58] Aimé Labbé et al. "Recent Advances and Challenges in the Development of Radiofrequency HTS Coil for MRI". In: *Frontiers in Physics* 9 (2021). ISSN: 2296-424X. DOI: 10.3389/fphy.2021.705438. URL: https://www.frontiersin.org/articles/10.3389/fphy.2021.705438.

[59] Bright Appiah Adu-Gyamfi and Clara Good. "Electric aviation: A review of concepts and enabling technologies". In: *Transportation Engineering* 9 (2022), p. 100134. ISSN: 2666-691X. DOI: https://doi.org/10.1016/j.treng.2022.100134. URL: https://www.sciencedirect.com/science/article/pii/S2666691X2200032X.

[60] Francesco Grilli et al. "Superconducting motors for aircraft propulsion: the Advanced Superconducting Motor Experimental Demonstrator project". In: *Journal of Physics: Conference Series* 1590.1 (July 2020), p. 012051. DOI: 10.1088/1742-6596/1590/1/012051. URL: https://dx.doi.org/10.1088/1742-6596/1590/1/012051.

[61] Xiaowei Song et al. "Commissioning of the World's First Full-Scale MW-Class Superconducting Generator on a Direct Drive Wind Turbine". In: *IEEE Transactions on Energy Conversion* 35.3 (2020), pp. 1697–1704. DOI: 10.1109/TEC.2020.2982897.

[62] Manuel La Rosa Betancourt et al. "High-Temperature Superconductors as a Key Enabling Technology for Space Missions". In: Nov. 2021. DOI: 10.2514/6.2021-4110.

[63] L. Lu et al. "Potential Applications of MTS and HTS to MRI Imaging Systems for Particle Beam Therapy". In: *International Journal of Radiation Oncology*Biology*Physics* 111.3, Supplement (2021). 2021 Proceedings of the ASTRO 63rd Annual Meeting, S46–S47. ISSN: 0360-3016. DOI: https://doi.org/10.1016/j.ijrobp.2021.07.126. URL: https://www.sciencedirect.com/science/article/pii/S0360301621009962.

[64] Jun Nagamatsu et al. "Superconductivity at 39 K in magnesium diboride". In: *Nature* 410 (Mar. 2001), 63 EP -. URL: http://dx.doi.org/10.1038/35065039.

[65] K Vinod, R G Abhilash Kumar and U Syamaprasad. "Prospects for MgB 2 superconductors for magnet application". In: *Superconductor Science and Technology* 20.1 (2007), R1. URL: http://stacks.iop.org/0953-2048/20/i=1/a=R01.

[66] A.I. Golovashkin et al. "Low temperature direct measurements of Hc2 in HTSC using megagauss magnetic fields". In: *Physica C: Superconductivity* 185-189 (1991), pp. 1859–1860. ISSN: 0921-4534. DOI: https://doi.org/10.1016/0921-4534(91)91055-9. URL: http://www.sciencedirect.com/science/article/pii/0921453491910559.

[67] Laan van der D. C et al. "Temperature and magnetic field dependence of the critical current of BiSrCaCuO tape conductors". In: (Jan. 2001), pp. 3345–3348.

[68] Tsuyoshi Sekitani, Yasuhiro H Matsuda and Noboru Miura. "Measurement of the upper critical field of optimally-doped YBa 2 Cu 3 O 7-d in megagauss magnetic fields". In: *New Journal of Physics* 9.3 (2007), p. 47. URL: http://stacks.iop.org/1367-2630/9/i=3/a=047.

[69] H. W. Weijers et al. "High Field Magnets With HTS Conductors". In: *IEEE Transactions on Applied Superconductivity* 20.3 (June 2010), pp. 576–582. ISSN: 1051-8223. DOI: 10.1109/TASC.2010.2043080.

[70] Christian Barth. "High Temperature Superconductor Cable Concepts for Fusion Magnets". 31.03.04; LK 01. PhD thesis. 2013. 232 pp. ISBN: 978-3-7315-0065-0. DOI: 10.5445/KSP/1000035747.

[71] Ziad Melhem. *Global Superconductivity Alliance for the Future Initiative*. 2023. URL: https://mt28.aoscongres.com/docs/ScGA_presentation.pdf.

[72] Ziad Melhem. *Superconductivity Global Alliance (ScGA): Enabling Next Generation of Magnets for Greener, Healthier, Prosperous and Sustainable Future*. 2023. URL: https://mt28.aoscongres.com/superconductivity-global-alliance%21en.

[73] J. Pereiro et al. "Insights from the study of high-temperature interface superconductivity". In: *Philosophical Transactions of the Royal Society of London A: Mathematical, Physical and Engineering Sciences* 370.1977 (2012), pp. 4890–4903. ISSN: 1364-503X. DOI: 10.1098/rsta.2012.0219. eprint: http://rsta.royalsocietypublishing.org/content/370/1977/4890.full.pdf. URL: http://rsta.royalsocietypublishing.org/content/370/1977/4890.

[74] Erica Salazar. *HTS magnets and SPARC: Paving a pathway towards faster, smaller, and economical high-field fusion energy*. URL: https://suli.pppl.gov/2022/course/PPPL_HTSmagnets_ppt.pdf.

[75] J. W. Ekin. "Offset criterion for determining superconductor critical current". In: *Applied Physics Letters* 55.9 (1989), pp. 905–907. DOI: 10.1063/1.102259. eprint: https://doi.org/10.1063/1.102259. URL: https://doi.org/10.1063/1.102259.

[76] *IEC 61788-1:2006 | IEC Webstore*. https://webstore.iec.ch/publication/5909. (Accessed on 10/08/2018).

[77] Saul Rindt. *Development of the First ReBCO-CORC Based Racetrack Model Coil*. Eindhoven University of Technology, 2018.

[78] Helmut Krauth. "Fabrication and Application of NbTi AND Nb3Sn Superconductors". In: *Vacuumschmelze GmbH Co. KG Report* (Jan. 2001), p. 13.

[79] Hiroshi Maeda et al. "A New High-Tc Oxide Superconductor without a Rare Earth Element". In: *Japanese Journal of Applied Physics* 27.2A (Feb. 1988), p. L209. DOI: 10.1143/JJAP.27.L209. URL: https://dx.doi.org/10.1143/JJAP.27.L209.

[80] A. Molodyk et al. "Development and large volume production of extremely high current density YBa2Cu3O7 superconducting wires for fusion". In: *Scientific Reports* 11.1 (Jan. 2021), p. 2084. ISSN: 2045-2322. DOI: 10.1038/s41598-021-81559-z. URL: https://doi.org/10.1038/s41598-021-81559-z.

[81] *Wire Specification | SuperPower*. http://www.superpower-inc.com/content/wire-specification. (Accessed on 10/03/2018).

[82] You-He Zhou, Dongkeun Park and Yukikazu Iwasa. "Review of progress and challenges of key mechanical issues in high-field superconducting magnets". In: *National Science Review* 10.3 (Jan. 2023), nwad001. ISSN: 2095-5138. DOI: 10.1093/nsr/nwad001. eprint: https://academic.oup.com/nsr/article-pdf/10/3/nwad001/49716762/nwad001.pdf. URL: https://doi.org/10.1093/nsr/nwad001.

[83] W. H. Fietz et al. "High-Current HTS Cables: Status and Actual Development". In: *IEEE Transactions on Applied Superconductivity* 26.4 (June 2016), pp. 1–5. ISSN: 1051-8223. DOI: 10.1109/TASC.2016.2517319.

[84] Y. Terazaki et al. "Measurement and Analysis of Critical Current of 100-kA Class Simply-Stacked HTS Conductors". In: *IEEE Transactions on Applied Superconductivity* 25.3 (June 2015), pp. 1–5. ISSN: 1051-8223. DOI: 10.1109/TASC.2014.2377793.

[85] N. Yanagi et al. "Stable operation characteristics and perspectives of the large-current HTS STARS conductor". In: *Journal of Physics: Conference Series* 2545.1 (July 2023), p. 012008. DOI: 10.1088/1742-6596/2545/1/012008. URL: https://dx.doi.org/10.1088/1742-6596/2545/1/012008.

[86] Shinnosuke Matsunaga et al. "HTS-WISE Conductor and Magnet Impregnated With Low-Melting Point Metal". In: *IEEE Transactions on Applied Superconductivity* 30.4 (2020), pp. 1–5. DOI: 10.1109/TASC.2020.2969613.

[87] Y. Narushima et al. "Test of 10 kA-Class HTS WISE Conductor in High Magnetic Field Facility". In: *Plasma and Fusion Research* 17 (2022), p. 2405006. DOI: 10.1585/pfr.17.2405006.

[88] Zachary S. Hartwig et al. "The SPARC Toroidal Field Model Coil Program". In: *IEEE Transactions on Applied Superconductivity* 34.2 (2024), pp. 1–16. DOI: 10.1109/TASC.2023.3332613.

[89] D. G. Whyte et al. "Experimental Assessment and Model Validation of the SPARC Toroidal Field Model Coil". In: *IEEE Transactions on Applied Superconductivity* 34.2 (2024), pp. 1–18. DOI: 10.1109/TASC.2023.3332823.

[90] Makoto Takayasu et al. "HTS twisted stacked-tape cable conductor". In: *Superconductor Science and Technology* 25.1 (2012), p. 014011. URL: http://stacks.iop.org/0953-2048/25/i=1/a=014011.

[91] D Uglietti, Rainer Wesche and Pierluigi Bruzzone. "Design and Strand Tests of a Fusion Cable Composed of Coated Conductor Tapes". In: 24 (June 2014), pp. 1–4.

[92] T. Mito et al. "Development of FAIR conductor and HTS coil for fusion experimental device". In: *Journal of Physics Communications* 4 (Feb. 2020). DOI: 10.1088/2399-6528/ab7954.

[93] Zachary S Hartwig et al. "VIPER: an industrially scalable high-current high-temperature superconductor cable". In: *Superconductor Science and Technology* 33.11 (Oct. 2020), 11LT01. DOI: 10.1088/1361-6668/abb8c0. URL: https://doi.org/10.1088/1361-6668/abb8c0.

[94] Wilfried Goldacker et al. "Roebel cables from REBCO coated conductors: a one-century-old concept for the superconductivity of the future". In: *Superconductor Science and Technology* 27.9 (2014), p. 093001. URL: http://stacks.iop.org/0953-2048/27/i=9/a=093001.

[95] A. Kario. *HTS Roebel cables for the EuCARD2 "Future Magnets*. 2016. URL: https://indico.cern.ch/event/489475/contributions/1166833/attachments/1263291/1868932/23.04.2016_Malta_Kario.pdf.

[96] V. Corato et al. "Strategy for Developing the EU-DEMO Magnet System in the Concept Design Phase". In: *IEEE Transactions on Applied Superconductivity* 32.6 (2022), pp. 1–7. DOI: 10.1109/TASC.2022.3153248.

[97] N Bykovskiy et al. "Experimental study of stability, quench propagation and detection methods on 15 kA sub-scale HTS fusion conductors in SULTAN". In: *Superconductor Science and Technology* 36.3 (Feb. 2023), p. 034002. DOI: 10.1088/1361-6668/acb17b. URL: https://dx.doi.org/10.1088/1361-6668/acb17b.

[98] G. Celentano et al. "Design of an Industrially Feasible Twisted-Stack HTS Cable-in-Conduit Conductor for Fusion Application". In: *IEEE Transactions on Applied Superconductivity* 24.3 (June 2014), pp. 1–5. ISSN: 1051-8223. DOI: 10.1109/TASC.2013.2287910.

[99] A. Augieri et al. "Electrical Characterization of ENEA High Temperature Superconducting Cable". In: *IEEE Transactions on Applied Superconductivity* 25.3 (2015), pp. 1–4. DOI: 10.1109/TASC.2014.2364391.

[100] Giuseppe Celentano et al. "Bending Behavior of HTS Stacked Tapes in a Cable-in-Conduit Conductor With Twisted Al-Slotted Core". In: *IEEE Transactions on Applied Superconductivity* 29.5 (2019), pp. 1–5. DOI: 10.1109/TASC.2019.2899248.

[101] Andrea Augieri. *Recent activities on REBCO and IBS materials at ENEA*. 2023. URL: https://indico.cern.ch/event/1302031/contributions/5620809/attachments/2743314/4772725/ENEA%20Actities%20on%20REBCO%20and%20IBS%20-%20AAugieri.pdf.

[102] Yi Shi et al. "Quasi-Round HTS Conductor Using REBCO Tapes for Fusion Magnet Application". In: *IEEE Transactions on Applied Superconductivity* 30.1 (2020), pp. 1–4. DOI: 10.1109/TASC.2019.2931998.

[103] M. J. Wolf et al. "HTS CroCo: A Stacked HTS Conductor Optimized for High Currents and Long-Length Production". In: *IEEE Transactions on Applied Superconductivity* 26.2 (Mar. 2016), pp. 19–24. ISSN: 1051-8223. DOI: 10.1109/TASC.2016.2521323.

[104] Michael J. Wolf et al. "Critical Current Densities of 482 A/mm2 in HTS CrossConductors at 4.2 K and 12 T". In: *IEEE Transactions on Applied Superconductivity* 28.4 (2018), pp. 1–4. DOI: 10.1109/TASC.2018.2815767.

[105] M J Wolf et al. "HTS CroCo - a Strand for High Direct Current Applications". In: *Journal of Physics: Conference Series* 1590.1 (July 2020), p. 012020. DOI: 10.1088/1742-6596/1590/1/012020. URL: https://dx.doi.org/10.1088/1742-6596/1590/1/012020.

[106] Michael J. Wolf et al. "High temperature superconductors for fusion applications and new developments for the HTS CroCo conductor design". In: *Fusion Engineering and Design* 172 (2021), p. 112739. ISSN: 0920-3796. DOI: https://doi.org/10.1016/j.fusengdes.2021.112739. URL: https://www.sciencedirect.com/science/article/pii/S0920379621005159.

[107] Changtao Kan et al. "Development of a 10 m quasi-isotropic strand assembled from 2G wires". In: *Physica C: Superconductivity and its Applications* 546 (2018), pp. 28–33. ISSN: 0921-4534. DOI: https://doi.org/10.1016/j.physc.2017.12.004. URL: https://www.sciencedirect.com/science/article/pii/S0921453417301430.

[108] Hao Chen et al. "Experimental Study on Quasi-Isotropic Critical Current of an HTS Conductor With High Engineering Current Density". In: *IEEE Transactions on Applied Superconductivity* 29.5 (2019), pp. 1–4. DOI: 10.1109/TASC.2019.2901603.

[109] Yang Li et al. "Investigation on Critical Current Properties of Quasi-Isotropic Strand Made From Coated Conductors". In: *IEEE Transactions on Applied Superconductivity* 25.3 (2015), pp. 1–5. DOI: 10.1109/TASC.2014.2365695.

[110] Jiuke Wang et al. "Study on critical current of a flexible quasi-isotropic HTS conductor with high engineering current density". In: *Fusion Engineering and Design* 160 (2020), p. 111820. ISSN: 0920-3796. DOI: https://doi.org/10.1016/j.fusengdes.2020.111820. URL: https://www.sciencedirect.com/science/article/pii/S0920379620303689.

[111] Jeremy D. Weiss et al. "Introduction of CORC ® wires: highly flexible, round high-temperature superconducting wires for magnet and power transmission applications". In: *Superconductor Science and Technology* 30.1 (Nov. 2016). DOI: 10.1088/0953-2048/30/1/014002.

[112] Danko van der Laan et al. *High-field magnets wound from CORC® cables and wires*. CHATS on Applied Superconductivity 2017. Sendai, Japan. Dec. 2017.

[113] T A J Meulenbroeks et al. "Observation of a non-uniform current distribution in stacked high temperature superconducting tapes". In: *Journal of Physics: Conference Series* 1293.1 (Sept. 2019), p. 012065. DOI: 10.1088/1742-6596/1293/1/012065. URL: https://dx.doi.org/10.1088/1742-6596/1293/1/012065.

[114] L. Krempasky and C. Schmidt. "Ramp-rate limitation in large superconducting magnets due to 'supercurrents'". In: *Cryogenics* 36.6 (1996), pp. 471–483. ISSN: 0011-2275. DOI: https://doi.org/10.1016/0011-2275(96)00006-9. URL: https://www.sciencedirect.com/science/article/pii/0011227596000069.

[115] D. Uglietti. "A review of commercial high temperature superconducting materials for large magnets: from wires and tapes to cables and conductors". In: *Superconductor Science and Technology* 32.5 (Apr. 2019), p. 053001. DOI: 10.1088/1361-6668/ab06a2. URL: https://doi.org/10.1088/1361-6668/ab06a2.

[116] D. Uglietti et al. "Non-twisted stacks of coated conductors for magnets: Analysis of inductance and AC losses". In: *Cryogenics* 110, 103-118 (Sept. 2020), pp. 103–118. DOI: 10.1016/j.cryogenics.2020.103118. URL: https://www.sciencedirect.com/science/article/pii/S001122752030120X.

[117] Nagato YANAGI et al. "Feasibility of HTS Magnet Option for Fusion Reactors". In: *Plasma and Fusion Research* 9 (2014), pp. 1405013–1405013. DOI: 10.1585/pfr.9.1405013.

[118] Y Narushima et al. "Characteristics and causes of voltage observed at the current feeder of high-temperature superconducting WISE conductor". In: *Journal of Physics: Conference Series* 2545.1 (July 2023), p. 012009. DOI: 10.1088/1742-6596/2545/1/012009. URL: https://dx.doi.org/10.1088/1742-6596/2545/1/012009.

[119] N. Amemiya. "Overview of current distribution and re-distribution in superconducting cables and their influence on stability". In: *Cryogenics* 38.5 (1998), pp. 545–550. ISSN: 0011-2275. DOI: https://doi.org/10.1016/S0011-2275(98)00007-1. URL: https://www.sciencedirect.com/science/article/pii/S0011227598000071.

[120] Walter H. Fietz et al. "High-Current HTS Cables: Status and Actual Development". In: *IEEE Transactions on Applied Superconductivity* 26.4 (2016), pp. 1–5. DOI: 10.1109/TASC.2016.2517319. URL: https://ieeexplore.ieee.org/document/7406727.

[121] P. Bruzzone, Walter H. Fietz, Joseph V. Minervini et al. "High temperature superconductors for fusion magnets". In: *Nuclear Fusion* 58.10 (Aug. 2018), p. 103001. DOI: 10.1088/1741-4326/aad835. URL: https://doi.org/10.1088/1741-4326/aad835.

[122] D C van der Laan, J D Weiss and D M McRae. "Status of CORCsup®/sup cables and wires for use in high-field magnets and power systems a decade after their introduction". In: *Superconductor Science and Technology* 32.3 (Feb. 2019), p. 033001. DOI: 10.1088/1361-6668/aafc82. URL: https://doi.org/10.1088/1361-6668/aafc82.

[123] S.C. Richter et al. "Bending Radius Limits of Different Coated REBCO Conductor Tapes - An Experimental Investigation with Regard to HTS Undulators". In: *Proc. IPAC'21* (Campinas, SP, Brazil). International Particle Accelerator Conference 12. https://doi.org/10.18429/JACoW-IPAC2021-THPAB042. JACoW Publishing, Geneva, Switzerland, Aug. 2021, THPAB042, pp. 3837–3840. ISBN: 978-3-95450-214-1. DOI: 10.18429/JACoW-IPAC2021-THPAB042. URL: https://jacow.org/ipac2021/papers/thpab042.pdf.

[124] Makoto Takayasu et al. “HTS twisted stacked-tape cable conductor”. In: *Superconductor Science and Technology* 25.1 (Dec. 2011), p. 014011. DOI: 10.1088/0953-2048/25/1/014011. URL: https://dx.doi.org/10.1088/0953-2048/25/1/014011.

[125] Neil Mitchell et al. “Superconductors for fusion: a roadmap”. In: *Superconductor Science and Technology* 34.10 (Sept. 2021), p. 103001. DOI: 10.1088/1361-6668/ac0992. URL: https://dx.doi.org/10.1088/1361-6668/ac0992.

[126] S. Oh et al. “Preliminary Design Study on Non-Twisted HTS Conductor for Fusion Applications”. In: *IEEE Transactions on Applied Superconductivity* 33.5 (2023), pp. 1–5. DOI: 10.1109/TASC.2023.3262490.

[127] Sergey A. Lelekhov. “Analysis of a Possibility to Use Parallel Non-Twisted Stacks of HTS Tapes as Cable in High Current Conductor of Tokamak Toroidal Field Coils”. In: *IEEE Transactions on Applied Superconductivity* 31.5 (2021), pp. 1–5. DOI: 10.1109/TASC.2021.3069322.

[128] N. Koizumi et al. “Experimental results on instability caused by non-uniform current distribution in the 30 kA NbTi Demo Poloidal Coil (DPC-U) conductor”. In: *Cryogenics* 34.2 (1994), pp. 155–162. ISSN: 0011-2275. DOI: https://doi.org/10.1016/0011-2275(94)90038-8. URL: https://www.sciencedirect.com/science/article/pii/0011227594900388.

[129] Toshiyuki Mito et al. “Extra AC losses for a CICC coil due to the non-uniform current distribution in the cable”. In: *Cryogenics* 38.5 (1998), pp. 551–558. ISSN: 0011-2275. DOI: https://doi.org/10.1016/S0011-2275(98)00029-0. URL: https://www.sciencedirect.com/science/article/pii/S0011227598000290.

[130] K. Takahata et al. “Coupling losses in cable-in-conduit conductors for LHD poloidal coils”. In: *Fusion Engineering and Design* 65.1 (2003), pp. 39–45. ISSN: 0920-3796. DOI: https://doi.org/10.1016/S0920-3796(02)00279-X. URL: https://www.sciencedirect.com/science/article/pii/S092037960200279X.

[131] Gourab Bansal et al. “Stability measurements with non-uniform current distribution in NbTi cable-in-conduit conductor for SST-1”. In: *Fusion Engineering and Design* 81.20 (2006). Proceedings of the Fifteenth International toki Conference on "Fusion and Advanced Technology", pp. 2491–2495. ISSN: 0920-3796. DOI: https://doi.org/10.1016/j.fusengdes.2006.07.082. URL: https://www.sciencedirect.com/science/article/pii/S0920379606002572.

[132] R Zanino et al. “EU contribution to the test and analysis of the ITER poloidal field conductor insert and the central solenoid model coil”. In: *Superconductor Science and Technology* 22.8 (July 2009), p. 085006. DOI: 10.1088/0953-2048/22/8/085006. URL: https://dx.doi.org/10.1088/0953-2048/22/8/085006.

[133] Tetsuhiro Obana et al. “Investigation of long time constants of magnetic fields generated by the JT-60SA CS1 module”. In: *Fusion Engineering and Design* 137 (2018), pp. 274–282. ISSN: 0920-3796. DOI: https://doi.org/10.1016/j.fusengdes.2018.10.005. URL: https://www.sciencedirect.com/science/article/pii/S0920379618306574.

[134] S Imagawa et al. "Measurement of Decay Time Constant of Shielding Current in ITER-TF Joint Samples". In: *Journal of Physics: Conference Series* 1857.1 (Apr. 2021), p. 012013. DOI: 10.1088/1742-6596/1857/1/012013. URL: https://dx.doi.org/10.1088/1742-6596/1857/1/012013.

[135] Shinsaku Imagawa et al. "Simulation of Decay of Shielding Currents in ITER-TF Joint Samples". In: *Plasma and Fusion Research* 17 (2022), p. 2405021. DOI: 10.1585/pfr.17.2405021.

[136] N. Yanagi et al. "Design and development of high-temperature superconducting magnet system with joint-winding for the helical fusion reactor". In: *Nuclear Fusion* 55.5 (Apr. 2015), p. 053021. DOI: 10.1088/0029-5515/55/5/053021. URL: https://dx.doi.org/10.1088/0029-5515/55/5/053021.

[137] Diego Garfias et al. "Simulation of non-uniform current distribution in stacked HTS tapes". In: *Plasma and Fusion Research* 17 (2022), p. 2405066. DOI: 10.1585/pfr.17.2405066.

[138] Stuart Wimbush and Nicholas Strickland. "A Public Database of High-Temperature Superconductor Critical Current Data". In: *IEEE Transactions on Applied Superconductivity* PP (Nov. 2016), pp. 1–1. DOI: 10.1109/TASC.2016.2628700.

[139] N. M. Strickland, C. Hoffmann and S. C. Wimbush. "A 1 kA-class cryogen-free critical current characterization system for superconducting coated conductors". In: *Review of Scientific Instruments* 85.11 (Nov. 2014), p. 113907. ISSN: 0034-6748. DOI: 10.1063/1.4902139. eprint: https://pubs.aip.org/aip/rsi/article-pdf/doi/10.1063/1.4902139/13415662/113907_1_online.pdf. URL: https://doi.org/10.1063/1.4902139.

[140] Queval Loic. *BSmag Toolbox*. Apr. 2015. DOI: 10.13140/RG.2.2.15939.96806.

[141] *SuperMagnet, Cryosoft Solids Suite*. https://supermagnet.sourceforge.io/solids.html. 2021.

[142] L. Bottura, C. Rosso and M. Breschi. "A general model for thermal, hydraulic and electric analysis of superconducting cables". In: *Cryogenics* 40.8 (2000). 4th Workshop on Computation of Thermal Hydraulic Transients in Superconductors, pp. 617–626. ISSN: 0011-2275. DOI: https://doi.org/10.1016/S0011-2275(01)00019-4. URL: https://www.sciencedirect.com/science/article/pii/S0011227501000194.

[143] L. Bottura. "Thermal, Hydraulic, and Electromagnetic Modeling of Superconducting Magnet Systems". In: *IEEE Transactions on Applied Superconductivity* 26.3 (2016), pp. 1–7. DOI: 10.1109/TASC.2016.2544253.

[144] L. A. Hall. *Survey of electrical resistivity measurements on 16 pure metals in the temperature range 0 to 273 deg K*. National Bureau of Standards Boulder, CO, United States. 1968. URL: https://ntrs.nasa.gov/citations/19680012399.

[145] Wayne Reiersen. *ITER US Toroidal Field Coil Conductor*. 2024. URL: https://usiter.org/hardware/toroidal-field-conductor/.

[146] A. Foussat et al. "Overview of the ITER Toroidal Field Magnet System Integration". In: *IEEE Transactions on Applied Superconductivity* 26.4 (2016), pp. 1–5. DOI: 10.1109/TASC.2016.2536640.

[147] N. Koizumi et al. "Series Production of ITER TF Coil in Japan- Double-Pancake and Winding Pack Insulation". In: *IEEE Transactions on Applied Superconductivity* 28.3 (2018), pp. 1–4. DOI: 10.1109/TASC.2017.2776125.

[148] N. Koizumi. "Progress of ITER Superconducting Magnet Procurement". In: *Physics Procedia* 45 (2013). Proceedings of the 25th International Symposium on Superconductivity (ISS2012), pp. 225–228. ISSN: 1875-3892. DOI: https://doi.org/10.1016/j.phpro.2013.05.008. URL: https://www.sciencedirect.com/science/article/pii/S187538921300357X.

[149] F. Lucca et al. "ITER TF coil double pancake assembly: Laser welding numerical simulation". In: *Fusion Engineering and Design* 86.6 (2011). Proceedings of the 26th Symposium of Fusion Technology (SOFT-26), pp. 1472–1475. ISSN: 0920-3796. DOI: https://doi.org/10.1016/j.fusengdes.2011.03.105. URL: https://www.sciencedirect.com/science/article/pii/S0920379611003802.

[150] Andreas W. Zimmermann and Suleiman M. Sharkh. "Design of a 1 MJ/100 kW high temperature superconducting magnet for energy storage". In: *Energy Reports* 6 (2020). 4th Annual CDT Conference in Energy Storage Its Applications, pp. 180–188. ISSN: 2352-4847. DOI: https://doi.org/10.1016/j.egyr.2020.03.023. URL: https://www.sciencedirect.com/science/article/pii/S2352484720302341.

[151] M. Nakamoto et al. "Completion of the first ITER toroidal field coil in Japan". In: *Nuclear Fusion* 61.11 (Oct. 2021), p. 116044. DOI: 10.1088/1741-4326/ac26ed. URL: https://dx.doi.org/10.1088/1741-4326/ac26ed.